

Simple Processes in Complex Places

by

Casey M. Schneider-Mizell

A dissertation submitted in partial fulfillment
of the requirements for the degree of
Doctor of Philosophy
(Physics)
in The University of Michigan
2010

Doctoral Committee:

Professor Leonard M. Sander, Chair
Associate Professor Michal R. Źochowski
Professor Ratindranath Akhoury
Professor Mark E. Newman
Professor Scott E. Page

© Casey M. Schneider-Mizell 2010
All Rights Reserved

To Phil and Marie, for bringing me up right.

ACKNOWLEDGEMENTS

This thesis has only been possible due to a host of people who have helped me grow for as long as I've been around. First and foremost, my parents, Marie and Phil, have been as generous as can be in encouraging me and enabling me to pursue whatever it was I was interested in at any given time. I would not be who I am were it not for croquet and wabi, especially Nick and Anna, who grounded me in that peculiarly ridiculous sense of intellectual play that one can enjoy in college. And graduate school, for all its bumps, has allowed me to meet and befriend so many fantastic people; Jess, Sarah, Evan, Ross, Kate, Matt, Matt, Katy, Brooks, Andrew, without you I'd have burnt out long, long ago. I've been lucky to fall in with an excellent advisor, Len Sander, whose ability to cut to the heart of problems is humbling and inspiring. His unique approach to interdisciplinary physics set me off in directions I never had known existed before coming to Michigan. The work presented here would have been impossible without a multitude of scientists with whom I collaborated or learned from over many useful conversations: namely Michal Zochowski, Mark Newman, Evgeniy Khain, Mike Berens, Scott Page, Sarah Feldt, David Adams, Liz Strahman, Yen-Ting Lin, and Andy Stein. The Center for the Study of Complex Systems has offered innumerable opportunities for expanding my notions of how to use (and not use) quantitative approaches in understanding the world. And finally, I am deeply grateful for Jessica, who gave me purpose (and Colbert, an exceedingly delightful cat) in this last, important year.

Chapter II contains work published in two places. The first paper was Scott Page, who came to Len Sander and started our interest in the voter model. It was published in [128]. The second paper was with Len Sander and published in [150]. Chapter III is based on work published with Evgeniy Khain, Oskar Nowicki, Sean Lawler, Nino Chiocca, and Len Sander in [96]. I am grateful to Evgeniy for his work and perseverance on this paper, and am glad to have a small part of my data analysis on glioma spheroid invasion presented within it. Chapter IV is a project created with Michal Zochowski and Len Sander and developed with many interesting and active discussions with Jack Parent and Eshel Ben-Jacob. This work is ongoing.

Financial assistance for the work here came from grants from the NSF, NIH, the University of Michigan Center for Computational Medicine. I am grateful to the University of Michigan Rackham Graduate School, Institute for Complex Adaptive Matter, and the Institute for Mathematics and its Applications at the University of Minnesota for travel support to a variety of meetings, conferences, and schools that have been instrumental to my diverse education. The extensive computational resources of the Center for Advanced Computing in the University of Michigan School of Engineering were used for most simulations presented, otherwise I would have been here for even longer.

TABLE OF CONTENTS

DEDICATION	ii
ACKNOWLEDGEMENTS	iii
LIST OF FIGURES	vii
CHAPTER	
I. Introduction	1
1.1 Network Structure and Description	5
1.2 The Voter Model	10
1.3 Glioblastoma Multiforme	16
1.4 Adult Hippocampal Neurogenesis	20
1.4.1 Neurons and neuronal dynamics	20
1.4.2 The hippocampus and the dentate gyrus	24
1.4.3 Neurogenesis	26
II. Generalizations of the Voter Model on Networks	30
2.1 Conformity and dissonance in generalized voter models	30
2.1.1 Background: the mean field voter model	34
2.1.2 Scaling	36
2.1.3 Analysis using network theory	38
2.1.4 Discussion	42
2.2 A generalized voter model on complex networks	44
2.2.1 A generalized voter model	46
2.2.2 Bipartite Network	49
2.2.3 Random scale-free networks	51
2.2.4 Summary	62
III. Glioblastoma Pattern Formation	63
3.1 Introduction	64
3.2 Glioma clustering	66
3.3 Discussion	75

IV. Network Reorganization in Adult Neurogenesis	79
4.1 Neurogenesis model	82
4.1.1 Initial network formation	82
4.1.2 Neuronal dynamics	84
4.1.3 Neurogenesis and network reorganization	85
4.2 Results	86
4.2.1 Activity and augmentation patterns of the network in response to external stimulus	88
4.2.2 Innervation patterns of incorporated neurons	91
4.2.3 Firing dynamics	91
4.2.4 Robustness of network activity	93
4.3 Discussion	94
V. Summary and Conclusions	99
APPENDIX	103
BIBLIOGRAPHY	120

LIST OF FIGURES

Figure

1.1	Example of voter model processes. a) The voter model on a 1d lattice. Having selected the starred site to update in this time step, a neighbor is chosen with probability $p = 1/2$. In this instance, the right one is picked. b) The voter model on a network with degree heterogeneity under node update rules. Site A has a degree of 3, but site B has degree of 5. Because of this, the probability of site A giving its state to site B in one Monte Carlo step is much less than B to A . As a result, B has more influence on the dynamics of the network than A	12
1.2	Glioblastoma invasion into a collagen matrix, imaged with confocal microscopy. The spheroid in the center shedding cells which migrate into the matrix, spreading out with time. The spheroid is approximately 300 microns in diameter. Data from experiments performed by Tim Demuth and Mike Berens.	17
1.3	A cartoon diagram with the major parts of typical neuron. The cell body, or soma, has two types of neural processes. Dendrites form inputs to the cell and are typically arranged in dense arbors. Axons can extend far from the cell before branching. Axons from one cell and dendrites from another cell connect at a synapse.	21
1.4	Illustration of an action potential. Once the potential crosses the threshold, an action potential fires and then resets after a refractory period.	22

1.5	A simplified schematic of the healthy dentate gyrus. Granule cells (G) live in the granule cell layer, sending axons through the hilus to the CA3 and dendrites down into the molecular layer, where they receive efferents from the entorhinal cortex. Importantly, they do not synapse onto one another. Granule cell activity is moderated by inhibitory interneurons such as basket cells (B) which receive granule cell activity and synapse onto granule cells a moderate distance away. Mossy cells (M) also receive granule cell activity and form excitatory synapses onto the dendrites of distant granule cells. Though not shown, mossy cells and basket cells also connect to one another. Neurogenesis occurs at the boundary between the hilus and the granule cell layer.	25
2.1	A cartoon of the dynamics. Having picked the opinion of person j on topic i , the black node, we look to replace it by opinions having similar topic or similar person, shown as dark bordered nodes. With probability p we take from a randomly selected other persons opinion on topic i and with probability q we take from a randomly selected other topic within person j	33
2.2	The exit time, T , as a function of NM for $p = 0.5$. The different points are average over 2000 realizations for different values of N, M . Error bars are within the marker size. The loglog best fit line, shown as a dashed line, has a slope of 2.003.	37
2.3	The exit time, T , for $N = 10, M = 15$ as a function of p , averaged over 2000 realizations. Error bars are within the marker size.	38
2.4	The scaled exit time, qT as a function of NM^2 for three values of $q \ll 1$, averaged over 2000 realizations. A dashed line with slope unity is shown for reference. Error bars are smaller than the marker size. Since the exit times themselves vary by a factor of 1000 for the various values of q , the scaling behavior seems satisfactory. Different points correspond to different values of N, M . For example, the pairs (8,8) and (32,4) both give $NM^2 = 512$	40
2.5	The estimate of 2.20 compared to the results of simulations from Figure 2.3, shifted by a constant factor of order unity for comparison. The reciprocals of the other two eigenvalues are also shown. The gap between the values is of order 10^2 – 10^3 , so that the smallest eigenvalue dominates	43

2.6	Circles are the simulated fit of $d \log T / d \log N$ for a complete bipartite network with groups of size $M = 40$ and N ranging from 100 to 5000. The dotted line is the scaling of Equation 2.39 for the same range of N	51
2.7	Simulated values of $d \log T / d \log N$ under node selection based on several hundred runs for N from 750–15000. Squares correspond to $\nu = 2.8$, circles to $\nu = 2.4$. The dashed line is the scaling based on the diffusive estimate, calculated by fitting the numerically calculated sum in Equation 2.44 for similar values of N . Note that frustration begins to dominate for $\nu = 2.4$ at $\alpha > 1.6$, causing the deviation from the diffusive estimate.	54
2.8	Simulated values of $d \log T / d \log N$ under edge selection from several hundred runs of values of N from 750–15000. Square are for $\nu = 2.8$, circles for $\nu = 2.4$. The dashed line comes from fitting the numerically calculated sum in Equation 2.44 for similar values of N . The horizontal line is the effective slope of $T \sim \log N$ for the system sizes used.	55
2.9	A example of node update dynamics on a small network containing a global highest degree node (G) and a separate local highest degree node (L) for $\alpha = 1$ and $\alpha = 10$. The darkness of a node corresponds to the average fraction of time spent in a state opposite the final state of the network over 1000 realizations with identical initial conditions. A darker node has spent more time in a contrary state than a light node. For $\alpha = 1$, states are well mixed and $T = 9.4$. For $\alpha = 10$, the decay to the metastable value ρ^* does not occur. The local leader and its neighborhood spend most of the time in a contrary state and $T = 4814$	57
2.10	Normalized histogram of the absolute value of the time average deviation from ensemble equilibrium value ρ^* per node for $N = 3000$, $\nu = 2.4$, and $\alpha = 1$ (\times), 1.5 (\circ), 2 (\square), and 5 (\triangle) under node update dynamics, drawn over 50 (for $\alpha = 5$) or 10 (for all other α values) runs. For diffusive values of α , the deviations are gaussian and peaked around zero. For $\alpha = 5$, nodes do not center about ρ^* . The inset shows a normalized histogram of mean deviation values per network for $\alpha = 1$ (\times) and 5 (\square). The diffusive case is peaked around zero, whereas the frustrated case is broad and nonzero, showing large differences across networks.	58

2.11	Typical dynamics of the fraction of active edges (edges connecting nodes with different states) for diffusion and frustration. Both have $N = 10000$, $\nu = 2.8$, and edge selection. The top line, in black, is for $\alpha = 1$ and the bottom line, in gray, is for $\alpha = 8$. The $\alpha = 1$ case is diffusive and fluctuates to convergence after reaching the ensemble average value. The $\alpha = 8$ case decays exponentially to a value greater than the ensemble average value, because a locally highest degree node or cluster is slow to flip. Just before $t = 1200$, these nodes flip and the system reaches the absorbing state. Inset shows early time dynamics on a similar network for $\alpha = 10$ in gray and $\alpha = 4$ in black. Both decay exponentially initially, but the high α case becomes frustrated and the other continues to convergence. . .	60
2.12	The scaling of mean time for the most isolated local leader to adopt the state of a neighbor, based on 1000 networks and $N=1000\text{--}32000$. Circles are for $\nu = 2.4$, squares for $\nu = 2.8$, connecting lines indicate node update, markers only indicates edge update. Note that this ignores the probability that a neighbor has an opposite state, therefore certainly underestimating the time to flip, but still gives qualitative agreement to the behavior observed in simulations. . . .	61
3.1	Paths from a hanging drop spheroid assay of the X12 glioblastoma cell line.	65
3.2	Snapshots of the system for the two cell lines five days after the beginning of the experiment. ΔEGFR (b) cells form clusters, while WT cells (a) are homogeneously distributed over the system.	67
3.3	ΔEGFR cells a few hours after beginning of the experiment. Shown is a part of the system, $1400\mu\text{m}$ on $1400\mu\text{m}$. A circle shows a small cluster of cells, which randomly migrated and stuck together due to cell-cell adhesion.	68
3.4	A part of the phase diagram, for small densities and large adhesion parameters. The probability of migration decreases as the number of nearest neighbors increases to account for cell-cell adhesion. A border of the phase separation region (the solid line) is given by Eq. (3.1). We start from small density and turn on proliferation. The average density of cells increases, and one can either enter the two-phase region [path (A)-(B)] or remain in the stable region [path (C)-(D)], depending on the adhesion parameter (two dotted lines). . .	69

3.5	Clustering of $\Delta EGFR$ cells, as computed from the discrete model. Snapshots of the system are taken at time $T = 1800$, which corresponds to the fifth day of experiments (see Fig. 3.2b). An upper panel corresponds to the case $\alpha_{high} = \alpha_{low}$, a lower panel incorporates an assumption that invasive cells switch their phenotype to proliferative (and increase their proliferation rate), when they form clusters, here $\alpha_{high} \gg \alpha_{low}$. Parameters: $q = 0.9, \alpha_{low} = \alpha_{high} = 0.00127$ for the upper panel and $q = 0.84, \alpha_{low} = 0.0004, \alpha_{high} = 0.0056$ for the lower panel, the diffusion time is $\tau = 4$ minutes.	72
3.6	Cluster size distribution for $\Delta EGFR$ from experiment (circles, dotted line) and simulations (symbols). Pluses correspond to the case $\alpha_{high} = \alpha_{low}$, see also the upper panel in Fig. 3.5; squares correspond for the case we take into account the dynamic phenotypic switch between “invasive” phenotype and “proliferative” phenotype (see text) when cells form clusters, see also the lower panel in Fig. 3.5. Parameters are the same as in Fig. 3.5. An inset shows the phase diagram of parameters (q, α_{high}) as computed from simulations of the discrete model for $\alpha_{low} = 0.0017$ (see text). Above the dotted curve, the system shows density inhomogeneities, while below it the system remains homogeneous. Therefore, the possible parameters values for the wild type correspond to the lower part of the diagram.	74
3.7	Shed rate J from tumor spheroid (measured in $10^6 \text{ cells cm}^{-2} \text{ day}^{-1}$) as a function of the adhesion parameter q as computed in numerical simulations of a three-dimensional version of the discrete stochastic model. The dotted line corresponds to the experimentally observed shed rate for $U87\Delta EGFR$ cells, which gives $q \simeq 0.85$	76
4.1	Incorporation patterns of adult-born neurons in the rat hippocampus in normal conditions (Top) and four weeks post-status epilepticus (Bottom). The granule cell layer is denoted “gcl” and the hilus is denoted “h.” Note both abnormal locations of survival and disrupted innervation patterns. See A.1 for methods. Images provided courtesy of Jack Parent.	80
4.2	a) Cartoon schematic of the established network formation. Local excitatory-to-excitatory connections are rewired to a random excitatory cell with probability p . b) Examples of this process on reduced networks for each of the three regimes we consider in this work: Local ($p = 0$), small-world ($p = 0.1$), and global ($p = 1$). Each image is a subset of an excitatory network of 500 cells with an average out-degree of 3. Edges are colored darker according to how close their parent cell is to the center.	83

4.3	Examples of typical survival patterns of new cells for each of the normal inhibition three regimes: local ($p = 0$, small-world ($p = 0.1$), and global ($p = 0.7$). The top row depicts new cells (blue) amidst established cells (gray) and the stimulation point (magenta star). Incorporation is much more concentrated in the small-world case than either local or global. The second row highlights the out-connections (black lines) from one new cell. Local topologies, while localized, have less radial orientation of out-connections than small-world topologies. Global networks are highly random. The third row shows connections from the same cell to cells, new or established, with which its mean phase coherence was greater than 0.5 (red lines). Local and small-world networks are spatially constrained, but the small-world does not expand as far as local networks. Global networks, by contrast, show widespread synchronization. The fourth row depicts the mean firing delay from burst onset (early to late represented by blue to red). Global networks lack spatial firing order.	87
4.4	Descriptions of the distribution of activity. a) Average spatial distribution of final firing rate (top, log scale) and b) change of firing rate (bottom, linear scale) for several values of rewiring probability and inhibition. Only normal inhibition and local and small-world networks have spatially constrained final activity and activity change, with small-world having more focused increase of firing rate around the stimulated region. c) Activity profile as a function of distance from the stimulus at ten points during the simulation, averaged over the “worst-case” half of simulations with the highest rate of survival. Dark blue is the earliest, dark red the latest. Note the expanding profile in the local case. d) Mean network frequency as a function of the number of cells survived (different markers) and incorporated into the network for normal inhibition. d) Burst synchrony B, ranging from 0 for Poisson random firing to 1 for exactly simultaneous, as a function of number of cells survived. Notably, global networks are not functionally robust to the addition of activity-seeking cells. Where present, error bars denote standard error.	90

4.5	a) Mean distance of surviving cells from stimulus point. b) Spatial correlation of initial network activity and survival probability. Note that the optimum occurs for $p = 0.1$, with neither local nor global networks performing as well. c) Correlation of initial activity with change in activity. Again, small-world networks are the only ones to show consistent enhancement of initially active regions. d) Mean radial (relative to stimulus location) orientation of new cell out-connections. Small-world networks show the most radial order. e) Examples of the intraburst structure of instantaneous firing rate for local and global networks. In the local case, new cells fire as part of the burst, whereas in the global case new cells form a population that fires before the established network cells burst. f) The mean delay in intraburst firing onset of old cells compared to new cells. Local and small-world networks at normal inhibition do not see a large separation of new and old populations. Error bars in all cases denote standard error.	92
4.6	Mean network frequency (a) and burst synchrony B (b) as a function of the number of cells survived and incorporated into the network for normal inhibition. Notably, global networks are not functionally robust to the addition of activity-seeking cells.	94
A.1	Average mean path length (diamonds) and clustering coefficient (dots) as a function of rewiring probability p , normalized by the value for $p = 0$. All data points are averages over 20 simulated networks. The path length drops sharply as p increases, but the clustering coefficient has much slower decrease. The small-world regime is defined by having large clustering but small path length, which is found for rewiring probabilities near $p = 0.1$	105
A.2	Integration patterns of new neurons in normal inhibition networks, after perturbing the random jitter magnitude.	113
A.3	Integration patterns of new neurons in low inhibition networks, after perturbing the random jitter magnitude.	113
A.4	Integration patterns of new neurons in normal inhibition networks, after perturbing the size of the local radius for new cells. Increasing the radius causes almost no difference, although decreasing it too much results in cells that have a hard time finding strong innervation and thus surviving.	115

A.5	Integration patterns of new neurons in low inhibition networks, after perturbing the size of the local radius for new cells. Unlike the normal inhibition case, for low inhibition the radius matters, but only changes the absolute magnitudes of number of surviving new cells and mean distance and does not alter the shape of the dependence on p .	116
A.6	A comparison of integration patterns in a high connectivity network (4.5% instead of 3.5%) with 200 inhibitory cells. Note that around $p = 0.2$, the networks switch from behaving like they are in a low inhibition regime to one with normal inhibition.	117
A.7	a) Examples of the mean number of reconnection events as a function of space for several values of rewiring and inhibition. Note that in cases where the network acts like a good filter, which is to say at low p , the network splits into regions where it is easy to wire into and regions where it is hard to wire into, with the separation being greater for normal inhibition. b) Mean direction of output connections as a function of location for two different values of rewiring. Both have normal inhibition. For low rewiring, the connections are aligned radially, whereas for higher rewiring the orientation becomes more random. c) Average number of rewiring events. Networks with low inhibition require less searching to effectively integrate into the network.	119

CHAPTER I

Introduction

Many problems in physics are impossible to solve microscopically, but well described probabilistically. For example, in Brownian motion, a small particle such as pollen or a dust mote exhibits small jumps in random directions when floating on water. At the microscopic level, what is occurring is that a slightly different number of water molecules with slightly different momenta hit each side of the particle at any moment. While the resulting net force is very small, if the particle is also very small, this causes a significant acceleration. Newton's laws are perfectly well obeyed at every instant, but trying to predict the exact behavior of the fluid — and thus the forces — is a problem of untenable complexity. However, the statistical distribution of fluctuations is not nearly so complex. No one direction is preferred to others, all of the random kicks are uncorrelated in time, and the momentum kicks follow a Gaussian distribution [89]. While the trajectory of any one Brownian particle is thus unpredictable, the statistical characteristics of its path are not hard to calculate.

Problems in biology or the social sciences that have a similar flavor as Brownian motion abound. The genes for a given organism in a population depend on its exact lineage and chance encounters between zygotes. The spread of email viruses through a computer network depends on the exact address books of every computer. Diseases

move through populations, but respond to individual immune systems and random interactions between the sick and the susceptible. Yet in each case even though a complete description of the details is all but unknowable, the randomness can wash out and the gene distribution, number of infected computers, and size of an epidemic can all obey understandable statistics. The key message from this is that, when discussing stochastic processes, the behavior of populations can potentially be much more predictable than the individuals within it.

One of the surprising features of even a simple stochastic process is that its behavior can be extremely sensitive to the space in which they occur. Consider a drunkard who will take a step in any available direction with equal probability. We may ask what the probability is that he will return to where he starts after some number of steps. It turns out that if the drunkard is constrained to one dimension, thus only moving forward or back, such returns are frequent and inevitable [66]. In two dimensions, returns will occur with probability one, albeit in longer times. However, in three dimensions, perhaps a drunkard flying a spaceship, no returns to the origin can ever be expected.

Such a result is not at all unusual, nor limited to the random walk. Other processes exhibit qualitatively different behavior as a function of the space which they are in. Chaotic dynamics, with its sensitivity to initial conditions and complicated paths, is unattainable in two dimensional deterministic continuous dynamical systems [6]. This result, a direct consequence of the Poincare-Bendixson theorem, rests on the notion that trajectories are lines, and so periodic trajectories form closed loops. In a plane, closed loops separate space into an “inside” and an “outside,” which means that trajectories that start on one side of a periodic trajectory can never leave. There is not enough room in 2d for sufficiently intricate paths to ob-

serve anything beyond trajectories that converge to points or periodic cycles. In three dimensions and higher, though, lines are no longer form an impassable barrier and so dynamics are not similarly constrained. Another example comes from the general theory of phase transitions, which describes how many-body systems undergo abrupt, qualitative shifts in their state when some thermodynamic quantity passes a critical point, such as water turning from solid to liquid when warmed above freezing. If the number of dimensions of a system is below the lower critical dimension for a particular interaction, no phase transition can occur. At and above the lower critical dimension, transitions can occur, but behave differently near their critical point depending on the dimension. Above an upper critical dimension, behavior near a critical point no longer varies with further increases. For instance, the Ising model, which describes magnetic ordering of spin systems, exhibits no ordered phase in one dimension and no differences in phase transitions for four and higher dimensions [89]. Dynamical processes take some of their properties from their rules, but also some from the constraints — or lack thereof — imposed by the space in which they act.

The regular lattice is not the only type of space that one can be interested in, however. Consider influenza, which spreads through particular interactions between people. A description of the space on which disease dynamics occurs thus would not look like a regular lattice, but rather a network where each individual is ‘adjacent’ to other people with whom a relevant interaction occurs. However, now our intuition tells us something important: Surely the undergraduate living in a dorm among hundreds of people is more likely to get sick than a graduate student holed up in her basement laboratory. This intuition does generally turn out to hold true, at least in theoretical models (e.g. [74, 137], among many, many others). Even though the biology of disease spreading is more or less identical for the two individuals, the

space of interactions causes the social butterfly and the hermit to experience different dynamics.

This is not a trivial observation. Complex networks have turned out to be an effective representation of many situations across a variety of disciplines. In the language of network theory, people in the disease example are represented by ‘nodes’ and the direct connections between them are called ‘edges.’ In some situations, the network is a concrete interpretation of the system. Subway or train stations can be nodes, with edges between stations that are one stop apart. Neurons form physical connections to other neurons to which they send signals. In other cases, however, the network structure can describe more abstract relationships. Academic papers can form the nodes on a network that are connected to the papers that cite them. Food webs connect organisms to the organisms that they consume. Genes in a cell can be represented by nodes connected to other genes whose expression they influence. In some of these examples, for instance citation networks, structure itself is the primary object to describe. However, in others such as gene expression, neurons, or disease spread, the network represents an interaction topology for some dynamical process. Nodes connect to nodes whose dynamics they influence. Considering the diversity of behavior that can occur just by changing Euclidian dimensionality, one should not be surprised that complex, non-regular topologies can yield extremely rich behavior.

This dissertation will discuss in detail three particular topics: a toy model of opinion spread on networks, cancer cell motility, and the reorganization of neuronal networks. While these are unrelated topics in application, they all present relatively simple processes which exhibit interesting dynamics due to their environment. The remainder of the introduction is organized to first introduce the formalism and frequently studied properties of complex networks important for Chapters II and IV.

Following that, I will give background into each of the three chapters so the reader can better understand the context in which the questions arise.

1.1 Network Structure and Description

Network theory attempts describe and understand complex patterns of connectivity. As noted above, however, the systems being described range widely — from planes to humans to genomes — and with numbers of objects ranging from tens of people in a small social circle to millions of websites linking to one another or billions of neurons in a human brain. The seamless description such a diversity of topic and scale requires a very general formalism and nomenclature. In the interest of setting the stage for the work in this dissertation without going too far afield, only aspects important for the later chapters will be introduced here. The established literature has vastly more scope than I mention (See [5, 118, 120, 54] for far more thorough treatments).

We restrict the fundamental objects to be ‘units that can be connected,’ called nodes or vertices, and ‘connections themselves,’ called edges or links. A description of the network structure can then be realized by specifying the nodes and the edges between them. In the case that one wishes to describe merely the presence or absence of a connection, but not its strength, the network is called ‘unweighted.’ We can assign all nodes an index $\{i\}$ and define a matrix \mathbf{A} such that $A_{ij} = 1$ if node j is connected to node i and 0 otherwise. The resulting matrix \mathbf{A} is called the adjacency matrix, as it specifies which nodes are directly connected to what other nodes. If the strength of a connection is relevant, for instance a network of rail stations might want to include inter-station distance, the value of A_{ij} can take on an arbitrary value and the resulting network is called ‘weighted.’

It is also convenient to distinguish between networks where all connections are reciprocated, such as one formed by people who talk on the phone with one another, and those which connections are not necessarily symmetric, for instance who eats whom in a food web. The former type, known as undirected networks, have the useful property that

$$A_{ij} = A_{ji} \quad (1.1)$$

and thus

$$\mathbf{A} = \mathbf{A}^T. \quad (1.2)$$

Directed networks, which lack such symmetry, have no similar property.

Since networks can be large and complicated, one wishes to find measurements that can succinctly describe properties of networks as a whole. Given the adjacency matrix formalism, some quantities are both immediately suggested and quickly calculable. One of the most important is the number of connections a node has, known as its degree. For the sake of simplicity, the following will refer only to undirected networks, though the generalizations to directed networks are straight-forward. The degree of the i th node, k_i is easily given by

$$k_i = \sum_1^N A_{ij}. \quad (1.3)$$

This provides us with a discrete distribution $p(k)$ for the fraction of nodes of a given degree. Basic statistics can then be applied to determine quantities like the mean degree $\langle k \rangle = \sum_k kp(k)$ and higher moments.

Describing a network by its degree distribution may seem simplistic, since it ignores significant amounts of information about what lies on the other side of an edge. However, the shape of the distribution turns out to capture some important aspects of structural heterogeneity. I will contrast two common types of random

networks: Erdos-Renyi graphs and scale-free networks.

Erdos-Renyi random graphs were one of the first complex network models to be studied [59]. Consider a population of N nodes, with each possible pairwise connection being assigned an edge with probability α . This produces a network with degrees that are binomially distributed with mean degree $\langle k \rangle = \alpha(N - 1)$:

$$p(k) = \binom{N}{k} \alpha^k (1 - \alpha)^{N-k}. \quad (1.4)$$

For the typical case of large N and small α , $p(k)$ approximates a Poisson distribution with mean $\mu = \alpha N$. Exponentially few nodes thus have a degree that differs more than the standard deviation $\sigma = \sqrt{\alpha N}$ from μ . As a consequence, a typical node has a degree very near the mean.

Observations of real networks have found that they are nothing like an Erdos-Renyi network. An enormous number and variety of networks have a degree distribution which obeys a power law [119, 41]:

$$p(k) \propto k^{-\alpha} \quad (1.5)$$

where α is a constant. Power law distributions differ significantly from Gaussian distributions. Perhaps the most striking feature is that they lack a characteristic scale that usefully describes the population. Consider the ratio between the number of nodes with degree k and with degree $2k$:

$$\frac{p(k)}{p(2k)} = \frac{k^{-\alpha}}{(2k)^{-\alpha}} = 2^\alpha. \quad (1.6)$$

The ratio is independent of k . If all degrees were to be doubled, the distribution would remain fundamentally identical up to changes in the smallest possible values. In fact, it can be shown that distributions with this scale-free property are uniquely power laws. Additionally, because the probabilities decay merely geometrically (instead of

the much quicker exponential), some nodes with a very high degree are present, even if most other nodes have a much smaller degree. Because of this, there is no notion of a typical degree like there was with a binomial distribution.

In fact, the variance of the distribution can diverge with system size. Consider a network with N nodes and a degree distribution $p(k) = Ck^{-\alpha}$ where $C = \sum_{k=1}^N p(k)$. As N gets large, C converges to the reciprocal of the Riemann zeta function $\zeta_\alpha = \sum_1^\infty k^{-\alpha}$, and thus remains finite for $\alpha > 1$. For N large, the variance of the degree distribution can be approximated by the integral:

$$\langle k^2 \rangle = \int_1^N k^2 p(k) dk = C \int_1^N k^{2-\alpha} dk \propto \frac{C}{\alpha - 3} N^{3-\alpha} \quad (1.7)$$

If $\alpha < 3$, the $\langle k^2 \rangle$, and thus the size of the fluctuations, grows arbitrarily large as the size of the network grows. Similar analysis shows that the mean of the degree distribution diverges with system size if $\alpha < 2$. Interestingly, many measured networks have power law exponents between 2 and 3, where the mean is finite, but the deviations from that are on the order of the system size itself [41]. As we will see in the next section, when degree has influence on the behavior of a dynamical process on the network, the size of these fluctuations can have large consequences.

Important network properties are not restricted to cases with high degree heterogeneity. Another important class of networks is known as small-world, for their implications about the distance between any two individuals. It was initially observed as the social phenomenon that any two random individuals can almost always find some connection between them another as friends-of-friends-of-friends (with a typically cited average of six such hops [174]), though since then has been generalized outside of the social context.

The defining work to formalize the notion of small-worldness comes from Watts

and Strogatz [175]. They suggest that small-world networks have two properties: path lengths between nodes are ‘short,’ but nodes are nonetheless share most of their connections with their neighbors. There are several philosophically similar ways to define a characteristic path length for the network, but all relate to some average of the length of the shortest paths between all pairs of nodes. If the characteristic path length scales in proportion to the logarithm of the system size, it is considered ‘short’ in this context. This is compared to nodes in Euclidian space, for which the distance goes geometrically with system size.

The other property is inspired by a natural social behavior: friends tend to share friends with one another. Phrased in network terms, for a given node, how much overlap is there between its neighborhood and the neighborhood of its neighbors? One approach is to compare the number of connected triples of nodes (any set of three nodes in which there are at least two connections) to the number of fully-connected triples (sets of three nodes that all connect directly to one another). A clustering coefficient C can thus be defined as

$$C = \frac{3 \times \#\text{fully-connected triples}}{\#\text{connected triples}}, \quad (1.8)$$

which has the nice property that it ranges between 0 for a complete lack of overlap and 1 for complete overlap. One can also define a local clustering coefficient C_i for a node i , using only triples that include that node.

Though the extremely high degree nodes present in scale-free networks can provide the shortcuts to make a network small-world, it is not necessary to have high degree heterogeneity to accomplish this. An important example is provided by Watts and Strogatz’s highly influential random network model [175]. Consider a ring of N nodes, each of which is connected to the nodes within r steps of them, such that

$r \ll N$. Every node has the same degree, $k = 2r$. Each edge is then interrogated and with probability p rewired to a random node on the ring. For $p = 0.001\text{--}0.1$, there is a crossover from a purely local network with long paths to a small-world regime with short paths. The clustering remains high because nearby nodes have significant overlap in their connections, but the mean path length drops significantly as the rewired links provide shortcuts to distant parts of the network. If p increases much beyond 0.1, the local structure disappears as the topology becomes mixed throughout space.

Small-world properties are often found in social settings, as was their origin, but have been more recently been pointed toward in the brain [32]. Structural studies of connection patterns in the cortex [75] and the hippocampus [58] show them to be dominated by short-range connections, but with long-range connections also present. Functional studies of neural activity also show signs of small-worldness in how different brain regions fire together [180].

With some basic considerations about network structure now in mind, we now move onward onto processes on networks. By this, I mean systems where nodes have some sort of dynamical state and can interact with adjacent nodes following the structure of the network. The exact form of the interaction and the states, of course, depends on the process which we wish to study. I start with one of the simplest that exists.

1.2 The Voter Model

Despite its politically evocative name, the voter model is a nonequilibrium stochastic process studied primarily for its simplicity and amenability to closed form solutions. Simply stated, it is a discrete model wherein every site has a state $\sigma = \pm 1$.

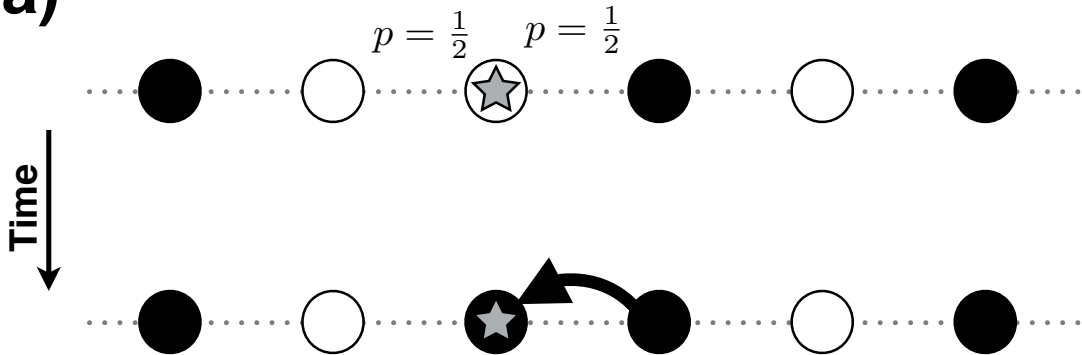
Every time step, a site is chosen at random to have its current state replaced by the state of a randomly chosen neighbor (see Figure 1.1a). An important properties leap out from that description: A node never adopts a state not possessed by a neighbor, so there is no temperature-like noise. If the system is ever entirely in a $+1$ state, there is no way to generate a -1 state (and vice versa). These consensus states are thus absorbing, meaning that the system cannot leave them.

The process was introduced in the mathematical probability community by Clifford and Subury in 1973 [43] and analyzed at length there through its connections to coalescing random walks [108]. It appears to have been developed independently in the physics literature, at least for the one and two dimensional case, by Krapivsky in a model of surface catalysis [100, 64]. Since then, it has more often been taken as a generic example for nonequilibrium processes [154, 21, 123], or as a toy model of the spread of neutral states such as opinions and rumors [36] or diseases [137].

The voter model does have direct parallels in ecology and population genetics. The neutral theory of biodiversity [82] studies a process in which non-moving individuals of some number of species populate a large 2d square lattice. The species identity at a given site is equivalent to the ± 1 state in the voter model,. On the death of an individual, the space it occupied is filled by an individual of a species on an adjacent site, just like in the voter model. This process, even though it contains no information about the distinct properties of different species, turns out to reproduce well the observed curve that relates the number of distinct observed species to the size of the region that one looks within (the so-called species-area curve).

In population genetics, one can consider what happens when a gene can take one of two alleles that have no bearing on the fitness (reproductive ability) of an organism and no individuals mate at random. For example, suppose (biologically

a)



b)

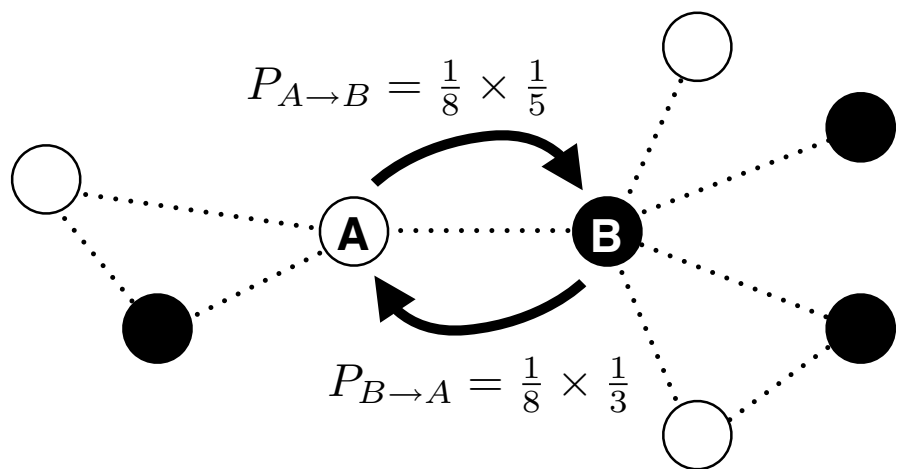


Figure 1.1: Example of voter model processes. a) The voter model on a 1d lattice. Having selected the starred site to update in this time step, a neighbor is chosen with probability $p = 1/2$. In this instance, the right one is picked. b) The voter model on a network with degree heterogeneity under node update rules. Site A has a degree of 3, but site B has degree of 5. Because of this, the probability of site A giving its state to site B in one Monte Carlo step is much less than B to A. As a result, B has more influence on the dynamics of the network than A.

incorrectly, in this case) that eye color is given by a single gene that can code for either blue eyes or brown eyes. If people with blue eye color and brown eye color have the same number of children on average, the two alleles for eye color have neutral fitness. In the basic Wright-Fisher model of neutral genetic drift, mutation is taken to be extremely rare and population is held constant from generation to generation. A time step corresponds to replacing the previous population with a new generation. Since alleles do not affect fitness, the new population comes from a random binomial sampling of the previous generation [25]. In a finite population, fluctuations cause one allele to be more dominant than the other and eventually being the only allele present, an event known as fixation. This process differs from a voter model on a complete graph — a network in which all nodes connect to all other nodes — only in that all updates are taken simultaneously instead of in a random sequence. In the continuous time, large N limit, this has no effect on the solutions to the model. Since genetic data is generally only present in organisms currently alive, a great deal of work has gone into quantitatively understanding similar types of genetic drift to reconstruct ancestral lineages, resulting in coalescent theory. Similar techniques have also been considered in linguistics, with language components such as pronunciation replacing genes [18, 17].

Returning to the importance of topology, one of the primary results of both the probability theoretic and statistical physics approaches is that the voter model on an infinite lattice will asymptotically approach consensus in one and two dimensions, but not three or higher [108]. The most direct intuition for the cause of this comes from the random walk duality. The boundary between dissimilar states follows a random walk, and when boundaries merge the random walkers can be thought of as annihilating. Because of this, consensus occurs when random walks all collide, a

phenomenon related to the return probability mentioned earlier. In one and two dimensions, walks will necessarily collide and thus consensus will occur as a coarsening process, but not in three or higher.

The consideration of voter model behavior on network topologies was slow to set in. Initial work considered the voter model on a complete graph, one in which every node is connected to every other node [154, 37]. This is equivalent to the mean field limit in physics and can, in a sense, be thought of as a lattice in $d = \infty$. In this case, the system performs a one dimensional random walk in the fraction of nodes with a given state, with a diffusion coefficient that depends on the system state. When the system is close to fixation, the probability of switching the state of a node decreases and so diffusion slows. Using standard first passage process techniques [143], it can quickly be seen that the mean time to consensus scales as

$$T \propto N^2 \quad (1.9)$$

in time units of Monte Carlo update steps. More connectivity actually slows down organization on the network, contrary to intuition. The first portion of Chapter II generalizes the mean field system into layers of fully connected networks with a controllable coupling between one another, and uses this as a toy study of opinion dynamics and the emergence of separable time scales. The work was done with Scott Page from the Department of Political Science at the University of Michigan and Len Sander and published in [128].

More recently, considerable interest has focused on studying the voter model onto complex networks. In the case of Watts-Strogatz networks of size N , the shortcuts cause the system to develop a long-lasting state where the system remains disordered for a duration that scales with system size before eventually fluctuating to consen-

sus [172, 38, 27]. In the limit of infinite system size, the system would remain in the disordered state forever. In finite systems, given that p is large enough for shortcuts to be plentiful ($p \approx \frac{1}{2rN}$) the fixation time scales with N^2 , recapitulating the mean field result in that respect. Other aspects, such as correlation lengths, depend sensitively on p and were solved exactly in [172].

Much richer dynamics are observed when the voter model is placed onto networks with heterogeneous degree [141, 151, 18, 170, 11, 161, 162, 157, 38, 156]. The first task that must be done in such a situation is to decide what exactly it means to place the voter model on such networks. Three possibilities arose early on: a random node adopts the state of a random neighbor (what we will call node update, following [161]), a random node gives its state to a random neighbor (an invasion or reverse voter model [35]), or a random edge is chosen and which node gets the state of the other is determined at random (link update, again following [161]). All of these rules are identical on networks where all nodes have the same degree, a class that includes lattices, but when there is heterogeneity the situation differs considerably. Nodes with more edges are more likely to be a randomly chosen neighbor than nodes with fewer edges. Depending on the formulation of the model, they have more or less influence accordingly (for an example, see Figure 1.1b). The consensus time for the node update voter model on heterogeneous networks was solved in the scaling regime [157] and later with a more precise approximation [141]. Baxter, Blythe, and McKane have also put forth a very different approach to estimate the time to fixation of a general stochastic process using coalescent theory techniques, for which any form of voter model on an arbitrary network is a special case [18, 24].

The second portion of the work in Chapter II is devoted to generalizing the voter model into a form that can admit all three definitions of the process and solving for

the consensus time in networks. This section is based on work done with Len Sander and was published in [150].

1.3 Glioblastoma Multiforme

Glioblastoma multiforme is an unusually lethal form of brain cancer that strikes around 80,000 people per year in the U.S. and Europe alone. Despite years of work on therapies, the rate of survival 5 years after diagnosis remains a dismal 3% and median survival is only 12–14 months [65]. As with many cancers, the typical treatment begins with surgical removal (resection) of the tumor. Unfortunately, the typical glioma phenotype has a solid tumor core that is constantly shedding cells into the brain [106]. Invasion of cancer cells into the brain creates problems both with diagnosis and with treatment. Radiological imaging and MRI cannot resolve cancer cells at low densities, thus diagnosis of the extent of invasion is impossible to estimate. As a result, resection misses a considerable fraction of the pathological cells present in the brain [163]. Secondary tumors can form within this diffuse halo, eventually leading to death. Invading glioma exacerbate this problem by preferentially migrating along white matter tracts, which includes the corpus callosum that links the brain hemispheres.

Chemical and radiological treatments have yet to prove particularly effective and it has been suggested that targeting motility or shedding could allow for more successful outcomes [51]. The mechanisms involved in motility and shedding are somewhat different. A moving cell has a well-defined polarity, establishing a distinct front and back. The cell moves by first extending a process forward, either a long thin filopod or psuedopod in a 3d environment or a wide, flat lammelopod on a 2d surface. The process forms bonds with the extracellular matrix (ECM) at its far forward end. The

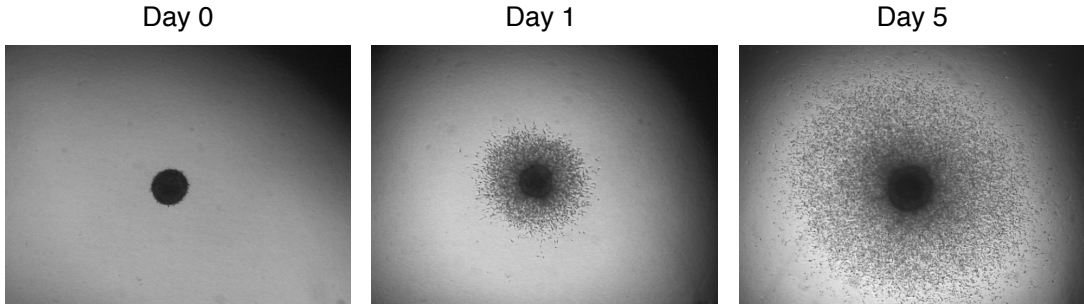


Figure 1.2: Glioblastoma invasion into a collagen matrix, imaged with confocal microscopy. The spheroid in the center shedding cells which migrate into the matrix, spreading out with time. The spheroid is approximately 300 microns in diameter. Data from experiments performed by Tim Demuth and Mike Berens.

cell can then exert a contractile force on itself by sliding actin filaments that run the length of the cell along one another. By detaching from the substrate at its rear, the cell pulls itself forward. A family of transmembrane proteins called integrins regulates the amount of adhesion between the cell and the matrix [83, 80]. Experiments have found that cell speeds exhibit a biphasic dependence on the amount of cell-matrix adhesion [181]. This is consistent with the intuitive notion that a cell can't go anywhere if it can't grab onto its substrate, but neither can it get anywhere if it can't let go. Good reviews of many of the physical details of motility can be found in [171, 114, 63, 9].

Shedding is the process of a cell leaving a solid mass of tumor cells. Typically, this involves a similar extension and pulling process as motility, but the detachment step now involves disconnecting not from the ECM, but from other cells. Cell-cell adhesion is governed by a class of several proteins called cadherins. Increased cadherin expression is associated with significantly fewer cells detaching and disruption of cadherin adhesion complexes correlates with increased invasiveness [12, 71, 16, 77]. Shedding can be thought of as a competition between cell-matrix adhesion, governing

the ability of a cell to pull, and cell-cell adhesion, governing the ability of a cell to leave the solid tumor.

Animal models can provide some insights into tumor growth and invasion, but because observation at the cellular resolution requires the death of the animal, limited data can be taken the trajectory of any one tumor. If we want a detailed understanding of the relationship between adhesions, motility, and network deformation, we need to be able to link up a variety of quantifiable measurements *in vivo* and *in vitro*.

Adhesion strengths are measured in many ways, some much more direct than others. The amount of cadherins a cell expresses can be qualitatively measured with Western blot assays, which allow one to observe the spatial extent of a protein smeared across a substrate by electrical potential, or quantitatively by flow cytometry, which measures the intensity of a fluorescence signal of labeled proteins. Cell lines that are adhesive enough to maintain a coherent spheroid have an effective surface tension that can be quantified via observation of the final spheroid shape after a known compression [176, 77]. Surface tension measurements correlate strongly with cadherin expression [77]. Detachment forces can also be measured directly, by bringing two cells into contact with one another and then pulling them apart. This can be observed at the cell level using two pipettes [112, 40] or at the individual molecular level by attaching one cell firmly to a substrate and the other cell to the cantilever of an atomic force microscopy setup [104, 105]. The rupture thresholds of integrin bonds, and thus cell-matrix adhesion, can be similarly measured using atomic force microscopy. Cell-level matrix adhesion strengths can also be qualitatively described using by measuring the probability of a cell detaching from a surface under a fluid wash or an applied centripetal force.

It is also valuable to measure the motility properties of cells, for instance the mean speed and the persistence length and time. A variety of assays have been developed for this in 2d and 3d. The work done in Chapter III will be related two types of assays in particular, the descriptions of which I will focus on here: one in which cells are placed at low densities on a surface and allowed to move [26, 76], the other where solid spheroids of cells are placed within a 3d collagen matrix [56].

Two dimensional motility studies have the advantage that they are easy to perform and observe. A petri dish coated with ECM proteins provides a substrate that cells will move on, and their behavior at low cell densities is well treated as a random walk [47]. Since cells tend to not typically crawl atop one another before forming confluent monolayers, cell-cell contact is also easy to see. However, cells that move in 3d environments tend to crawl along fibers, not surfaces, and many of the results do not generalize from one situation to the other [45, 138, 129, 55].

Thankfully, three dimensional assays can be done using gels made of collagen-I or a proprietary protein mixture called matrigel [98]. Confocal microscopy can then be used to image slices from a narrow range of depths. From a full z-stack of confocal images, a 3d reconstruction of cell position is easy to acquire. To get at simultaneous questions of shedding and motility, it is possible to culture clusters of around 1000 glioma cells as a spheroid and place it within the bulk of the gel. In this situation, it becomes possible to consider shedding and motility as separate events that are independently measurable [159]. Collagen is much softer than brain tissue, however. The same pulling forces that allow cells to leave a spheroid also induce long range alignment of the matrix in a radial direction [73, 167]. The feedback of collagen realignment onto individual cell motion is likely part of observation that cells have a predominantly radial path when leaving spheroids [160].

The work presented in Chapter III considers the effect of adhesion in motile cells. We use direct measurements of shedding in hanging drop assays to calibrate a phenomenological model of cell-cell adhesion that leads to a good description of observations of pattern formation in motility assays. In doing so, we suggest a useful approach to connecting cell-cell adhesion to the first steps of the invasion process. This work was done in collaboration with Evgeniy Khain and Len Sander, as well as Oskar Nowicki, Sean Lawler, and Antonio Chiocca of the Department of Neurological Surgery at The Ohio State University Medical Center and published in [96].

1.4 Adult Hippocampal Neurogenesis

The brain is comprised of around 100 billion neurons, cells which can send electrical signals to one another, and roughly the same number of glia, cells which form a physical substrate for neurons and provide complex environmental regulation. Though connections between neurons have long been known to change over time, until recently it was thought that no neurons were born in the adult mammalian brain. Several years ago it was discovered that there are at least two places in the brain where new cells are generated throughout adult life: the subventricular zone, from which new cells migrate to the olfactory bulb, and the hippocampus, a structure connected with memory formation and spatial learning [122, 124, 2]. Additionally, the process of integrating new cells is very sensitive to firing activity in the network. This presents an interesting case of a dynamical process, influencing the evolution of the network structure on which it operates.

1.4.1 Neurons and neuronal dynamics

Neurons come in a vast array of phenotypes, but they share several basic characteristics of general importance. See Figure 1.3 for a cartoon of a single neuron.

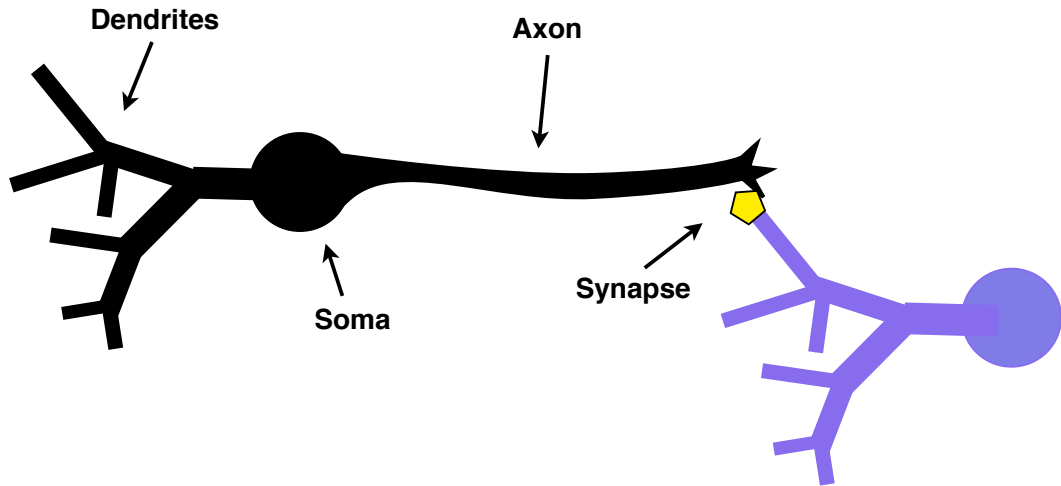


Figure 1.3: A cartoon diagram with the major parts of typical neuron. The cell body, or soma, has two types of neural processes. Dendrites form inputs to the cell and are typically arranged in dense arbors. Axons can extend far from the cell before branching. Axons from one cell and dendrites from another cell connect at a synapse.

They have a cell body, or soma, roughly 10 microns in diameter that remains fixed in place and contains the cell nucleus and organelles. The cell has two types of neural processes that extend from it: axons and dendrites. The axon is the output channel for neural signals, and may reach lengths as long as millimeters in some neuron types. The far end, or terminal, of the axon may have long branches to reach several other neurons. Dendrites form the input channel to a neuron. Though the total length of a single cell's dendrites may be long, they are typically patterned into dense arbors with many branchings. Because of this, dendrites do not extend great distances from the cell body. When two cells connect to one another, the axon of the upstream (or efferent) cell and the dendrite of the downstream (or afferent) cell meet at a synapse. Neurotransmitters are stored on the axonal side of the synapse, and can be released by the pre-synaptic cell and quickly bind to specific receptors on the dendritic side of the synapse as part of signal transduction.

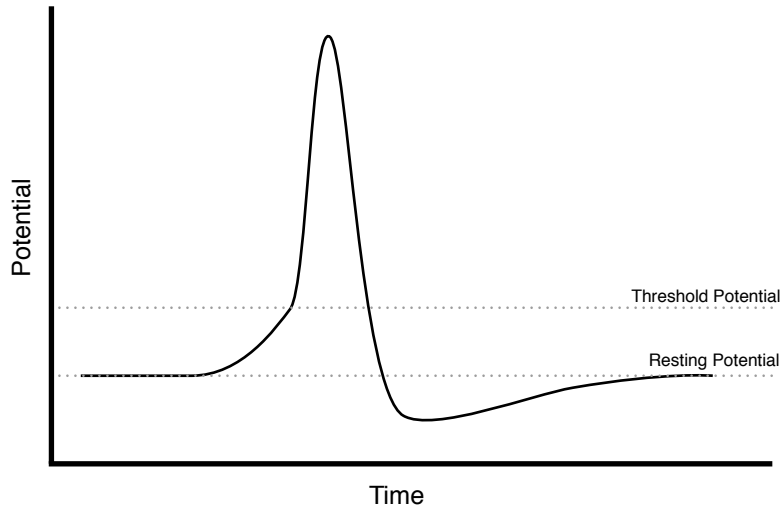


Figure 1.4: Illustration of an action potential. Once the potential crosses the threshold, an action potential fires and then resets after a refractory period.

Neuronal dynamics are based around the transmembrane electrical potential. In its resting state, a neuron maintains a resting potential difference of -70 mV by controlling the internal concentration of Na^+ , K^+ , and Ca^{2+} using active ion pumps. When a neuron's potential exceeds a threshold, typically around -55 mV , the ion gate behavior changes and the cell can rapidly depolarize and re-polarize, a behavior known as an action potential (see Figure 1.4). Spikes and firing events are common alternative names for action potential events. The depolarization period is very fast, on the order of 1 ms , and followed by a brief overshoot of several milliseconds where the polarization goes past the resting value. This refractory period creates a delay during which a cell cannot easily fire an action potential, which establishes an effective maximum firing rate that is slower than the spike dynamics.

The effect of an action potential on its downstream connections can be either excitatory or inhibitory, depending on the neurotransmitter involved. Cells which produce glutamate at their synapses typically induce an excitatory post-synaptic current that causes small depolarization in efferent cells. Multiple excitatory currents

that occur in quick succession are responsible for moving the membrane potential beyond the threshold for a spike. The effect of excitatory currents can be suppressed by cells which use GABA as a neurotransmitter. Most cells respond to GABA with an inhibitory post-synaptic current that causes hyper-polarization, pulling the membrane potential away from the firing threshold. Inhibitory neurons are often called interneurons. The amplitude of post-synaptic currents is determined not only by the phenotypes of the two neurons involved, but can be dynamically altered at individual synapses [1]. Adjusting synaptic weights on the time scale of hours and days to maximize causal correlations in pre-synaptic and post-synaptic firing events, a process known as spike time dependent plasticity, is important in learning. More rapid regulation by chemical factors in the local environment is also possible [155].

Because neuronal states are based on simple concentrations and potentials, it is possible to create a mathematical description of the effective voltage dynamics of an individual neuron [68]. The Hodgkin-Huxley model is a set of four coupled dynamical equations which phenomenologically describe both the ionic current dynamics and the dynamics of ion pumps. Simplifications of Hodgkin-Huxley dynamics, such as the Moriss-Lecar model and FitzHugh-Nagumo model describe only two variables: the potential and the rate at which the potential can recover to resting values. When details of the voltage dynamics are less important than the firing rate and large populations of neurons are being considered, integrate-and-fire, a one-dimensional model involving only voltage dynamics, is useful for its simplicity. The refractory period, however, has to be implemented by hand, and does not arise from dynamical equations.

1.4.2 The hippocampus and the dentate gyrus

When discussing populations of neurons, it is useful to distinguish between the anatomical network structure — which neurons synapse onto which other neurons — and the function of the brain, namely the spatiotemporal patterns of firing events. It is clear that there is a relationship between them, but the details of structure-function mappings are extraordinarily complex and certainly not one to one. Thankfully, the brain is organized into many modules that are structurally and functionally distinct and serve unique cognitive roles.

The hippocampus is a structure deeply involved in memory formation and awareness of spatial positioning. It can itself be broken down into a loop of submodules which each have a role in processing information [10]. Signals enter through the entorhinal cortex, which among other roles makes precise encoding of spatial positioning. From there, they are passed to the dentate gyrus (DG), which is directed associated with the storage of memories. The DG projects into the CA3 region, which in turn passes signals to the CA1 region. From there, signals are both sent out from the hippocampus through the subiculum and fed back into the entorhinal cortex. Each distinct component has a connectivity structure can generally be broken down into inputs from another region, recurrent neural circuitry that stays within the region, and outputs to the next segment.

As with many parts of the brain, the DG has an elaborate spatial structure based on layers [8]. It is segregated into three flat layers with a narrow transverse direction and a long longitudinal direction. The neuronal population is made up of two types of excitatory cells and a host of different types of inhibitory cells. I will focus on granule cells and mossy cells, the two excitatory types, and the most common interneuronal species, the basket cell. In the rat brain, there are around 10^6 granule

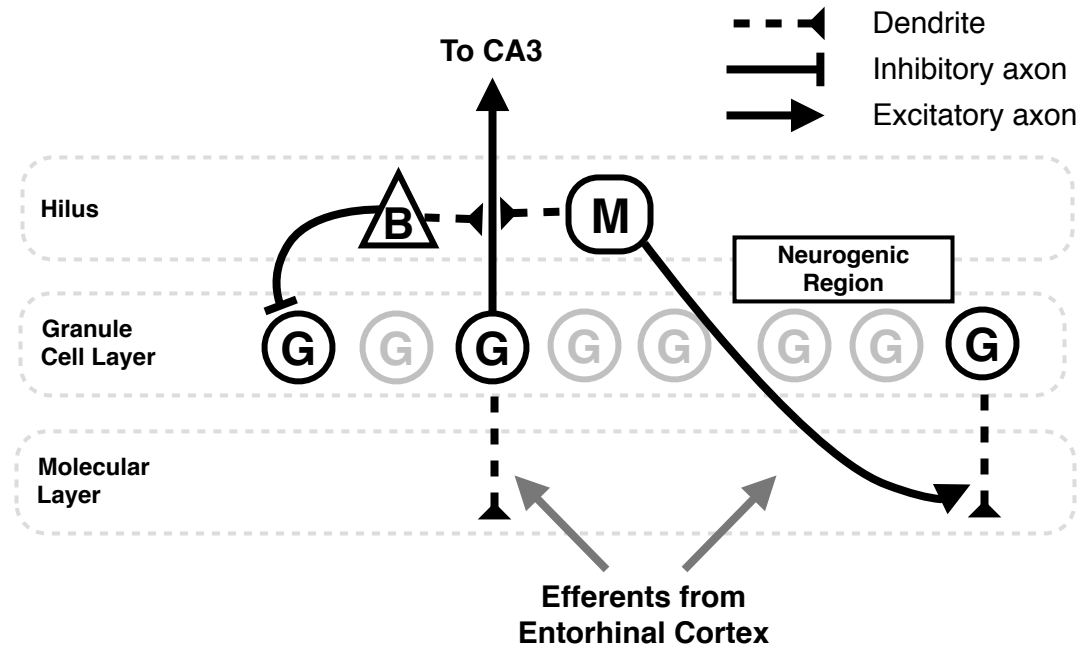


Figure 1.5: A simplified schematic of the healthy dentate gyrus. Granule cells (G) live in the granule cell layer, sending axons through the hilus to the CA3 and dendrites down into the molecular layer, where they receive efferents from the entorhinal cortex. Importantly, they do not synapse onto one another. Granule cell activity is moderated by inhibitory interneurons such as basket cells (B) which receive granule cell activity and synapse onto granule cells a moderate distance away. Mossy cells (M) also receive granule cell activity and form excitatory synapses onto the dendrites of distant granule cells. Though not shown, mossy cells and basket cells also connect to one another. Neurogenesis occurs at the boundary between the hilus and the granule cell layer.

cells, 3×10^4 mossy cells, and 10^4 basket cells.

The primary cell layer of the DG is the granule cell layer, which is home to granule cells (Figure 1.5). Granule cells have a distinct polarity, all of them sending their axons in one direction perpendicular to the layer and dendrites the opposite direction. Granule cell axons go to the hilus (or polymorphic layer), which is home to basket cells and mossy cells, as well as extending out to the CA3. Granule cell dendrites project into the molecular layer, which is comprised mostly of a dense tangle of neural processes, including axons from the entorhinal cortex. Neither granule cell

axons nor dendrites extend distally along the longitudinal direction of the DG. In keeping their axons and dendrites spatially separate, granule cells do not synapse onto one another.

Mossy cells form long range excitatory connections between granule cells. Mossy cell dendrites are enervated by nearby granule cells, but send axonal projections that extend distances on the order of the length of the DG. They share the hilus with basket cells, which are the region's major inhibitory neuronal species. Basket cells have similarly local connectivity patterns as granule cells, but receive inputs from granule cells, mossy cells, other interneurons, and even efferents from the entorhinal cortex.

1.4.3 Neurogenesis

Granule cells appear to be the only neuronal cell type in adult mammals that is produced in the adult brain. Neuronal stem cells use their neuronal processes to remain rooted in the subgranule zone at the interface between the hilus and the granule cell layer. They give rise to undifferentiated immature cells called neuroblasts, which migrate short distances to the granule cell layer. There, they respond to a chemical cue, reelin, generated by hilar interneurons that induces them to stop migrating and begin to mature into granule cells [72]. The survival rate for new cells is around 20-50% [48, 109]. Despite the constant introduction of new cells, the overall population of the DG remains constant even as the granule cell layer may turn over several times in the life of a rat [107].

The maturation process takes approximately seven weeks, and has a number of distinct intermediate phases [183, 127]. After two weeks, new cells have sent their dendrites into the molecular layer and receive synaptic inputs from GABAergic in-

terneurons. However, unlike mature cells, newborn granule cells respond to GABA with *excitatory* post-synaptic currents. Within two more weeks, glutamatergic afferents are also formed and neurotransmitters begin to have their normal effect. At this stage, for the first time, cells can produce normal action potentials and begin to form efferent synapses. There is considerable evidence that neurons at this stage are extremely plastic, and can both alter synaptic weights and form and destroy synapses at rates much higher than mature cells[14, 111]. After six to eight weeks, a cell matures and ceases to be distinguishable from the cells in the network that predate its birth.

It generally thought that new neurons benefit learning [3, 15, 124]. Experimental studies have shown that new cells do preferentially join active neural circuits [91]. Disruption of neurogenesis has also been correlated with decreased performance on spatial memory formation tasks, but the details have been difficult to determine [92]. A variety of computational studies have given some insights on the possible role of new neurons [177, 19, 48, 4]. These studies suggest that neural turnover is important to avoid overloading the neuronal networks memories and reduce the ability of it to continue encoding new patterns and that a short-duration plastic period benefits temporal separation of memories.

Neurogenesis is able to participate readily in learning tasks because it is sensitive to environmental activity throughout its birth and maturation. Excitatory activity in the environment increases the production rate of new cells [48]. Both GABAergic and glutamatergic activity promote the maturation process [67]. The high plasticity of immature cells means that the synaptic connectivity is the result of considerable activity-dependent reorganization and reweighting [153, 29]. Even survival rates have been observed to increase with increased firing rate of the new cell [109].

The general picture of the network dynamics of the dentate gyrus is thus one of multiple levels of feedback. Anatomical network structure influences functional structure, as it does everywhere in the brain. Through synaptic plasticity, functional structure can influence physical structure back, but this is slow for mature cells. Neurogenesis, however, adds a new form of fast feedback. Neuronal activity influences numerous aspects of cell integration, which in turn affects the anatomic structure. The DG's spatial order also affects neurogenesis in constraining the possible ways that a new cell can enter the network.

The nature of the feedback suggests that changes in the properties of one aspect will propagate into the others. Epilepsy, a pathology in which neuronal activity exhibits widespread synchrony, presents a natural experiment of such a situation. Injuries to the hippocampus can greatly alter the local network environment, affecting both connectivity and population structure [30]. Axons and dendrites from granule cells increase in both spatial extent and number of synapses [134, 132]. Unlike the situation in the healthy brain, granule cells in epileptic conditions can form synapses onto one another [57, 31]. In addition, there is significant trauma to the hilus, resulting in the death of inhibitory cells and some long-range mossy cells [113]. Computational models drawn from precise neuroanatomical measurements have found that these structural changes can be sufficient to allow epileptic activity [116, 58].

Neurogenesis in epileptic conditions is also abnormal [103, 133, 152, 183]. Birth and maturation rates are increased, especially immediately following injury [126, 135]. Without the reelin signals from hilar cells, new cells migrate into regions they would previously not have been able to, causing the granule cell layer to become wider and more diffuse [72, 78, 131]. Such ectopic granule cells do not follow the orderliness of the normal axonal and dendritic directions and contribute to a highly

altered connection structure longer processes and more synapses [86, 140]. It is still uncertain if neurogenesis in epileptic conditions has the potential to exert a healing effect or if it contributes to the pathology [133, 182]. Some experimental evidence suggests that reducing neurogenesis after epileptic injury has beneficial effects in rats, but the situation remains unclear [88].

In Chapter IV, we present what is, to the best of our knowledge, the first computational study to consider healthy and pathological neurogenesis under the same dynamic framework. We use a computational model to study the effect of network structure on the outcomes. Assuming that the rules for integration for new cells are pre-programmed to respond to activity, an assumption consistent with the biology, we show that there are qualitative differences in the types of dynamic networks that can come out of a neurogenesis process. This work has been done in collaboration with Len Sander, Michal Zochowski of the Department of Physics at the University of Michigan, Jack Parent of the Department of Neurology at the University of Michigan Medical Center, and Eshel Ben-Jacob of the School of Physics and Astronomy at Tel-Aviv University and is currently in preprint form [149].

CHAPTER II

Generalizations of the Voter Model on Networks

This chapter contains two generalizations of the voter model in complex environments. In both cases, network topology and the voter model process create a hierarchy of time scales, resulting in a rich set of regimes for the time to consensus of the system. In the first section, I present at a case inspired by social systems, where an individual can have conflicting drives for consistency that are unevenly weighted. This work was done with Scott E. Page and Len Sander and the section is derived from [128]. In the second section, I suggest a new process that can reproduce a variety of different voter-like models in complex networks. This research was done with Len Sander and the text for this section is derived from [150].

2.1 Conformity and dissonance in generalized voter models

The voter model describes one of the simplest statistical processes [108]. In this scheme there are N agents ('voters') that live on a graph, and can take on several values ('opinions'). In the simplest case there are two opinions which we denote by $+1, -1$. The dynamics is that a voter is chosen at random, and then a neighbor on the graph is chosen at random and 'influences' the first – that is, the chosen voter adopts the opinion of his neighbor. The dynamics continues until all of the voters are

in *conformity*, i.e all opinions are the same; then there can be no further change. We are interested in the mean time to arrive at this state for a finite number of voters. We will refer to this as the exit time, T .

The voter model provides a conceptual description of and provides insights into a variety of social, biological, and physical phenomena. In the social realm, the individual level tendency to conform has implications for macro levels of criminal activity [70], drug use, cultural behavior [13], altruistic behavior, technological adoption, and participation in political and social movements [179]. Economists typically treat conformity as a coordination game, a system wherein two players can choose one of two possible actions and receive a positive payoff only if they take the same one [44]. This approach has a mixed strategy equilibrium, wherein both players choose each action with probability 1/2. However, this equilibrium is not stable, and so is not often considered empirically.

This same underlying phenomenon – the matching of one entity’s state to that of another – arises in biology in the form of genetic drift [144]. In these models, the “opinions” take the form of two or more possible allele values. The applications to physics are, if anything, more direct. The model captures the coarsening of an alloy in the small-surface tension limit [53] and is very closely related to certain catalysis models for $A + B \rightarrow 0$ [184, 42].

A limitation of the voter model when applied to social and biological settings is that it fails to include a force for *consistency* among opinions on various issues. In social settings, that force has psychological underpinnings. While individuals do alter their behavior so as to conform with the majority as captured in the voter model, they also try to avoid cognitive dissonance [62]. In the biological setting, the consistency force can arise from differences between interactions within the local

ecosystem and between more distant ecosystems.

We generalize the standard voter model so as to include both a force for conformity and a force for consistency (avoidance of dissonance) [20]. We accomplish this by endowing each site with a vector of values of length M . For each coordinate of this vector, the site engages in a voter model with a fixed probability p . With probability $q = 1 - p$ the site considers the dissonance in its vector of values, and engages in a voter model with itself, i.e. it changes the value at different coordinates to match the values at other positions. In figurative language, a voter may have opinions about political party, the war in Iraq, gun control, etc. He can be influenced (with probability p) by his neighbors on any of this issues. With probability q he tries to change his own opinions to be consistent within himself. See Figure 2.1 for a picture of this geometry. We assume, for the purposes of the model, that there is a fixed relationship between opinions on these different issues, e.g., given cares about and apathetic about as the two possible states, a person apathetic about trade tariffs will be apathetic about farm subsidies, if he thinks about it.

The resulting model neatly captures a range of social phenomena from cultural formation – where individuals want to coordinate but also remain consistent – to the formation of political party platforms – party members want to agree with one another but also take consistent positions across issues. It may also be thought of as version of the well-known Wright Island model of population genetics [178]. In this model islands have a certain frequency of an allele which can be changed by migration from other islands. The migration probability is analogous to our p . In the limit of small p the two models are the same.

The results of applying these dynamics is surprising. Note that the only equilibria are for all voters to have the same opinion for each issue, i.e. complete conformity

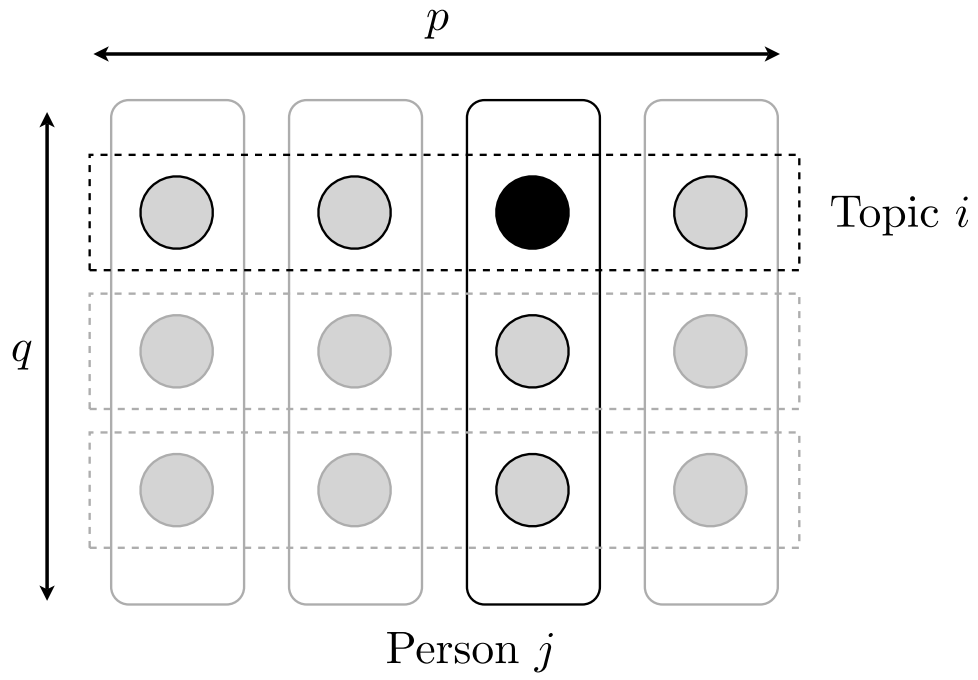


Figure 2.1: A cartoon of the dynamics. Having picked the opinion of person j on topic i , the black node, we look to replace it by opinions having similar topic or similar person, shown as dark bordered nodes. With probability p we take from a randomly selected other persons opinion on topic i and with probability q we take from a randomly selected other topic within person j .

and consistency. What is interesting is the time required for that convergence to occur, namely the exit time $T(N, M, p)$. The generalized model takes much longer to converge than the standard model. We will show that when p is very near to 0 or 1 T increases without bound. One implication of this is that if the conformity effect is much larger than the consistency effect, which could well be the case in some settings, then we might not expect convergence in a reasonable time. The model may partly explain persistent cultural heterogeneity, fractiousness of political parties, and genetic diversity of populations that we see in the world.

2.1.1 Background: the mean field voter model

The simplest graph for the voter model is the complete graph or mean field, i.e. all N voters are neighbors of each other. In this case a well-known connection to coalescing random walks makes solving for many properties straightforward [143]. To get a qualitative picture of the results, note that the system can be characterized by the number of plus opinions, denoted by n_1 . We now have the problem of a random walker at site n_1 on a line of length N . The probability of a move to the left or right is the probability of randomly selecting two sites with differing opinions. For large N this is $(n_1/N)(1 - n_1/N)$. The mean exit time starting from $j = n_1$, T_j , obeys a well-known equation [168]:

$$-1 = \frac{j}{N} \left(1 - \frac{j}{N}\right) (T_{j+1} - 2T_j + T_{j-1}) \quad (2.1)$$

The right hand side is the discrete second derivative of T . Letting $x = j/N$ be the density of plus opinions, for large N we have:

$$-N^2 = x(1-x) \frac{d^2}{dx^2} T(x) \quad (2.2)$$

on the unit interval, subject to $T(0) = T(1) = 0$. Therefore:

$$T(x) = -N^2(x \log(x) + (1-x) \log(1-x)) \quad (2.3)$$

This is the first passage time to the boundaries for a one dimensional random walk with spatially varying jump rate [97]. It should be noted that some authors define a unit of time to be a number of time steps equal to the system size, corresponding to the time it would take for all sites to update, which reduces T by a factor of N .

Real opinions do not, in general, take on just two values. Consider the case of three values, $0, \pm 1$. The system can be described by specifying any two of the opinions since $n_1 + n_0 + n_{-1} = N$. The dynamics is a random walk in a two dimensional space until one of the n 's is the whole population. We can think of this as a random walk on a triangular lattice inside a triangle with absorbing boundary conditions at the edges. (The edges correspond to one of the opinions being extinct.) There is a spatially dependent jump rate similar to that above. The essential behavior was not affected by the spatial dependence, so it will be ignored here. An extinct opinion cannot reappear, so once the system hits an edge, it performs a walk on that edge until it meets a vertex and the process stops. In general, for L attributes the system performs a random walk starting in an $L - 1$ dimensional simplex with absorbing boundary conditions until it hits a face. The walk continues in an $L - 2$ dimensional simplex and so on, until it hits one of the vertices which correspond to an equilibrium state.

Assuming, on average, the initial state of the system is that with equal numbers of each opinion, the corresponding random walker starts in the middle of the simplex. The center of an $L - 1$ dimensional simplex with side length N is of order N steps from a face. For a random walk in any dimension, it takes n^2 time to travel a distance

n . Thus the time to exit each simplex of dimensions $L - 1, L - 2, \dots$ is of order N^2 , as is the total time. An exact solution shows that the case of $L = 2$ and $L \rightarrow \infty$ differ only by a factor of $\log(2)$ [110]. For this reason, in what follows we will restrict ourselves to the two opinion case.

2.1.2 Scaling

We now return to the generalized voter model. Let there be N voters, each with an opinion on M issues; the opinions take values ± 1 . We can think of the graph as having M layers with N points which are all coupled to each other (i.e. mean-field coupling). Each column corresponds to a voter. Let p be the probability of an opinion change between voters in a layer, and $q = 1 - p$ be the probability of an internal change. These dynamics can conflict and slow the time to agreement.

For $M = 1$ or $N = 1$ we have the simple voter model with N or M voters, respectively. From the previous section, $T(N = 1, M) \propto M^2$. Similarly $T(N, 1) \propto N^2$. However, for $p = \frac{1}{2}$, $T(N, M, p = \frac{1}{2})$ must be symmetric in N and M . A reasonable guess is:

$$T(N, M, p = \frac{1}{2}) \propto N^2 M^2. \quad (2.4)$$

Simulations confirm this guess, as shown in Figure 2.2. In fact, this scaling holds pretty well for p up to 0.8. We should note for comparison that if we are not concerned with consistency, but find the time for M uncoupled layers to be in conformity, we would get $T \propto N^2 M$.

If $p \approx 1$, the fast dynamics is between voters. Each issue is almost always in conformity, and acts like a single issue in the simple model, namely $T \propto \tau M^2$, where τ is the time to flip a whole layer of voters. To find τ first note that we must wait $1/q$ time steps to have an exchange between layers. However, in most cases, the

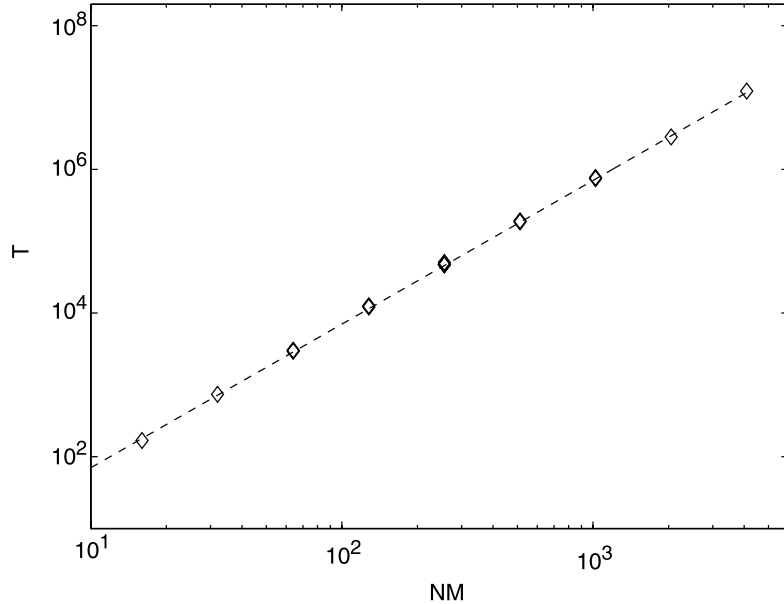


Figure 2.2: The exit time, T , as a function of NM for $p = 0.5$. The different points are average over 2000 realizations for different values of N, M . Error bars are within the marker size. The loglog best fit line, shown as a dashed line, has a slope of 2.003.

intralayer dynamics will simply eliminate the foreign opinion. The probability of a single introduced +1 changing a whole layer of -1 can be gotten by considering a random walk whose position is the number of +1's in the layer. We need to know the probability of a walker located adjacent to an adsorbing trap reaching a spot N spaces to its right before hitting the trap immediately to its left. This probability is $1/N$ [143], so that there need to be, on average, N introductions of a minority opinion before the layer flips. Thus τ , the time scale to flip the layer is N/q and $T \propto NM^2/q$. We expect the approximation to be valid if the time to generate a dissenting opinion, $1/q$, is bigger than the time to reach conformity, N^2 . That is $q < 1/N^2$.

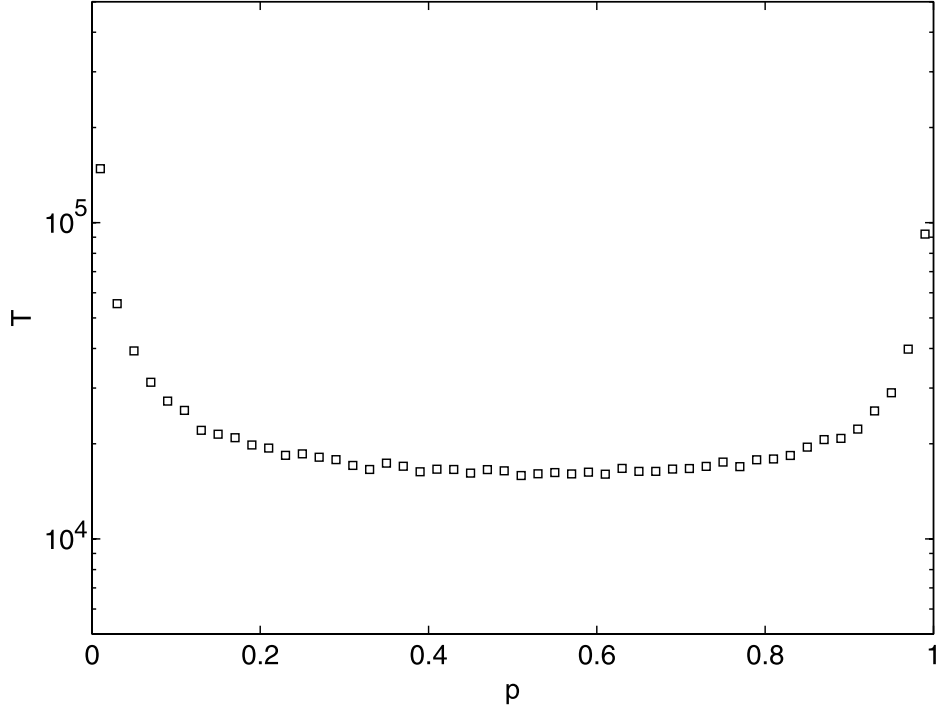


Figure 2.3: The exit time, T , for $N = 10$, $M = 15$ as a function of p , averaged over 2000 realizations. Error bars are within the marker size.

Exchanging $M \leftrightarrow N$ and $p \leftrightarrow q$ gives the result for $p \rightarrow 0_+$. This leads to:

$$T(N, M, p) \propto \begin{cases} NM^2/q & p \rightarrow 1_- \\ MN^2/p & p \rightarrow 0_+ \end{cases} \quad (2.5)$$

The overall behavior with p is shown in Figure 2.3. Note the increase for p near 0 or 1. Figure 2.5 shows a scaling plot which confirms Eq. 2.4.

2.1.3 Analysis using network theory

We now think of the graph on which the voters lie as a network with weighted bonds. Denote by \mathbf{s} the vector of all opinions and $\langle \mathbf{s} \rangle$ its ensemble average. The components of \mathbf{s} are denoted σ_i . Their averages lie in the interval $[-1, 1]$. The network structure is encoded in an $NM \times NM$ matrix \mathbf{A} such that A_{ij} is the probability that, having selected a node i , the opinion at i takes on the value of node j . Thus

we have

$$A_{ij} = \begin{cases} q/(M-1) & \text{If } i \text{ and } j \text{ are in the same voter} \\ p/(N-1) & \text{If } i \text{ and } j \text{ are of the same issue} \\ 0 & \text{Otherwise} \end{cases} \quad (2.6)$$

Note that the sum of the rows and columns is 1.

We use a method adopted from studies of the voter model on a lattice [64]. If the state of the voters is \mathbf{s} , let \mathbf{s}'_i be the same state as \mathbf{s} , but with $\sigma_i \rightarrow -\sigma_i$. The probability of being in state \mathbf{s} is $P(\mathbf{s})$. The transition rate for $\sigma_i \rightarrow -\sigma_i$ is:

$$W_i(\mathbf{s}) = \frac{1}{2}(1 - \sigma_i \sum_j A_{ij} \sigma_j) \quad (2.7)$$

The master equation for $P(\mathbf{s})$ is:

$$\frac{dP(\mathbf{s})}{dt} = \sum_i [W_i(\mathbf{s}'_i)P(\mathbf{s}'_i) - W_i(\mathbf{s})P(\mathbf{s})] \quad (2.8)$$

Using $\langle \sigma_i \rangle = \sum_{\{S\}} \sigma_i P(S)$, we can write an equation for the evolution of the average of σ_i :

$$\frac{d\langle \mathbf{s} \rangle}{dt} = -\frac{1}{\mathcal{N}}(\mathbf{I} - \mathbf{A})\langle \mathbf{s} \rangle. \quad (2.9)$$

where $\mathcal{N} = NM$ is the effective system size and \mathbf{I} is the $\mathcal{N} \times \mathcal{N}$ identity matrix. The matrix $\mathbf{I} - \mathbf{A}$ is a weighted version of the graph Laplacian. For this matrix all the eigenvalues are nonnegative and when a path exists between any two nodes, there is a zero eigenvalue whose eigenvector has all components equal.

The averages do not give the exit time directly. For this purpose we need two-point correlations. To see this, note that the density of edges along which there is a disagreement is $(1 - \langle \sigma_i[\mathbf{As}]_j \rangle)/2$ [21]. As the correlation function approaches unity, the system approaches conformity and consistency. In a way similar to the derivation of equation (2.9), we can show:

$$\frac{d}{dt}\langle \sigma_i \sigma_j \rangle = -\frac{1}{\mathcal{N}}(2\langle \sigma_i \sigma_j \rangle - \langle [\mathbf{As}]_i \sigma_j \rangle - \langle \sigma_i [\mathbf{As}]_j \rangle), \quad i \neq j. \quad (2.10)$$

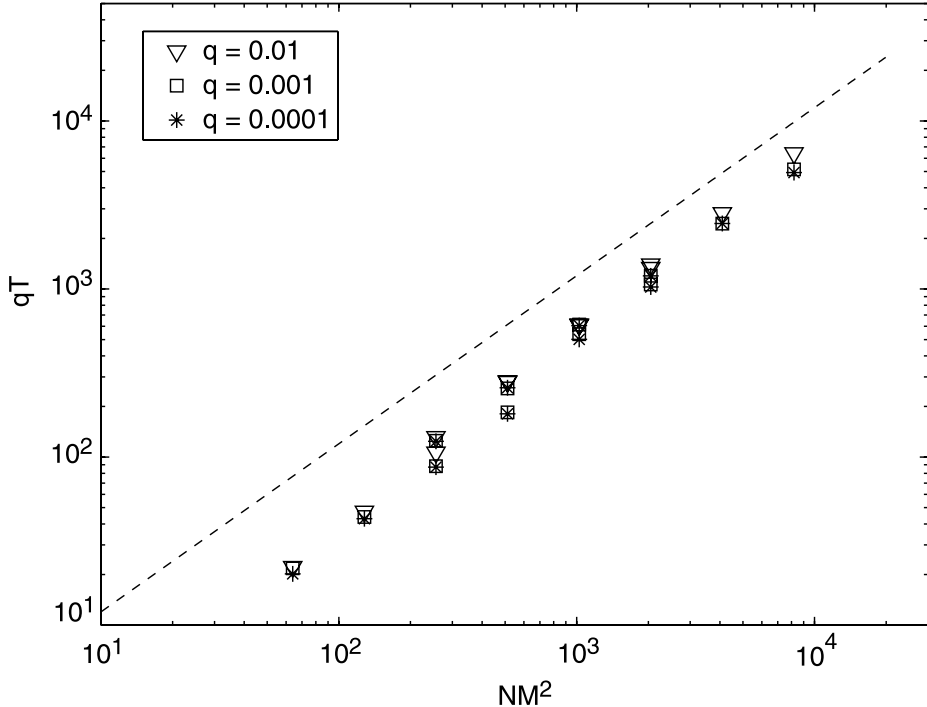


Figure 2.4: The scaled exit time, qT as a function of NM^2 for three values of $q \ll 1$, averaged over 2000 realizations. A dashed line with slope unity is shown for reference. Error bars are smaller than the marker size. Since the exit times themselves vary by a factor of 1000 for the various values of q , the scaling behavior seems satisfactory. Different points correspond to different values of N, M . For example, the pairs (8,8) and (32,4) both give $NM^2 = 512$.

For our network there are only four independent correlation functions since all nodes are equivalent. The autocorrelation is trivially 1 for all time. There are nodes within a voter that are connected by a function we will call r_v , and nodes in the same layer whose correlation we call r_h , and nodes that are not directed connected to one another which we call r_d . The \mathcal{N}^2 equations above thus reduce to three equations.

$$\frac{d}{dt}r_v = \frac{2}{\mathcal{N}} \left(\frac{q}{M-1} - \left(p + \frac{q}{M-1} \right) r_v + p r_d \right) \quad (2.11)$$

$$\frac{d}{dt}r_h = \frac{2}{\mathcal{N}} \left(\frac{p}{N-1} - \left(q + \frac{p}{N-1} \right) r_h + q r_d \right) \quad (2.12)$$

$$\frac{d}{dt}r_d = \frac{2}{\mathcal{N}} \left(\frac{p}{N-1} r_v + \frac{q}{M-1} r_h - \left(\frac{q}{M-1} + \frac{p}{N-1} \right) r_d \right) \quad (2.13)$$

Define:

$$\mathbf{r} = \begin{pmatrix} r_v \\ r_h \\ r_d \end{pmatrix} \quad (2.14)$$

$$\mathbf{v} = \begin{pmatrix} q/(M-1) \\ p/(N-1) \\ 0 \end{pmatrix} \quad (2.15)$$

$$\mathbf{B} = \begin{pmatrix} p + \frac{q}{M-1} & 0 & -p \\ 0 & q + \frac{p}{N-1} & -q \\ -\frac{p}{N-1} & -\frac{q}{M-1} & \frac{q}{M-1} + \frac{p}{N-1} \end{pmatrix}. \quad (2.16)$$

Then:

$$\frac{d}{dt}\mathbf{r} = \frac{2}{N}(\mathbf{v} - \mathbf{Br}). \quad (2.17)$$

Note that the asymptotic value of \mathbf{r} is $\mathbf{1}$, the vector with all components unity.

Thus we put $\mathbf{R} = \mathbf{1} - \mathbf{r}$. Note that $\mathbf{B}^{-1}\mathbf{v} = \mathbf{1}$, so that we can write:

$$\dot{\mathbf{R}} = -\frac{2}{N}\mathbf{BR}. \quad (2.18)$$

Denote by λ_i the eigenvalues and ν_i eigenvectors of B . Then the solution to Eq. (2.18) can be written:

$$\mathbf{r}(t) = \mathbf{1} - \sum_i (\mathbf{R}(0) \cdot \nu_i) e^{-2\lambda_i t / N} \nu_i \quad (2.19)$$

This can be used to make an estimate of the extinction time T for the system [100], namely as the rate of approach of \mathbf{r} to its asymptotic value. At long times the term which survives in Eq. (2.19) is the one with the smallest eigenvalue. Provided the eigenvalues are well separated, we have the approximation:

$$T \approx N/\lambda_{min}. \quad (2.20)$$

up to a factor of order unity.

Consider first the case $q \ll 1$. We can write $\mathbf{B} = \mathbf{B}_o + q\mathbf{B}_1$. We have:

$$\mathbf{B}_o = \begin{pmatrix} 1 & 0 & -1 \\ 0 & \frac{1}{N-1} & 0 \\ -\frac{1}{N-1} & 0 & \frac{1}{N-1} \end{pmatrix}. \quad (2.21)$$

$$\mathbf{B}_1 = \begin{pmatrix} -\frac{M-2}{M-1} & 0 & 1 \\ 0 & \frac{N-2}{N-1} & -1 \\ \frac{1}{N-1} & -\frac{1}{M-1} & \frac{1}{M-1} - \frac{1}{N-1} \end{pmatrix}. \quad (2.22)$$

The smallest eigenvalue of \mathbf{B}_o is 0 and the corresponding eigenvector is $\nu_o = (1, 0, 1)^\top$.

Rayleigh-Schroedinger perturbation theory tells us that, to first order in q , the smallest eigenvalue is:

$$q \frac{\nu_o \cdot \mathbf{B}_1 \nu_o}{\nu_o \cdot \nu_o} = q/(M-1). \quad (2.23)$$

Thus our estimate of T in this regime is $NM(M-1)/q$, in agreement with Eq. (2.4) and Figure 2.5.

A comparison between the scaling results and the smallest eigenvector are shown in Figure (2.5). From the Figure we see that the estimate gives the exit times correctly up to a factor ≈ 0.7 .

A solution for the exit times in the Wright island model was recently found using coalescent theory. It agrees with the scaling with system size and migration rate that we found here using simpler techniques [24].

2.1.4 Discussion

In this section, we have considered a generalization of the standard voter model that includes forces for dissonance avoidance as well as conformity. Such an assumption applies to a variety of social settings including cultural formation, political

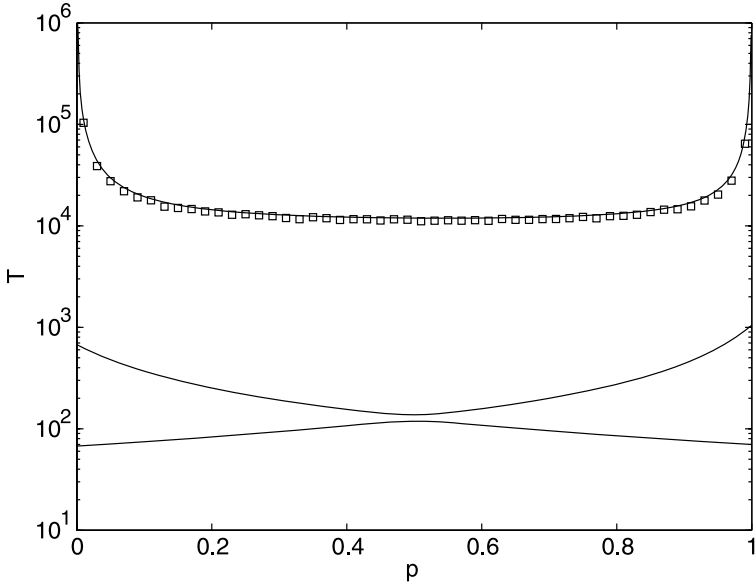


Figure 2.5: The estimate of 2.20 compared to the results of simulations from Figure 2.3, shifted by a constant factor of order unity for comparison. The reciprocals of the other two eigenvalues are also shown. The gap between the values is of order 10^2 – 10^3 , so that the smallest eigenvalue dominates

party platform creation, and organizational goal setting. Members of these collectives desire conformity, but they also desire consistency across issues or domains. For example, members of a political party want to cohere on common stands on issues but they also want a consistent underlying set of principles that relates positions across issues. The same forces also apply in some biological systems. Neutral genetic drift causes more prevalent alleles to preferentially spread, but separated populations may mix differently within-group and between-group.

At its core, this work considers the effects of adding these two forces. It is an exercise in showing the strengths and limitations of science as decomposition. We ask: does a model that includes both conformity and consistency perform like the product of the two individual models? We find that if the two forces apply at the same scale, if the probability of a voter conforming is of the same order as the probability of a voter ridding itself of an inconsistency, then the answer is a qualified

yes. The exit time is of order N^2M^2 , which is the product of the exit times of the individual models: a conformity model and an consistency model. However, when one force far outweighs the other, the answer is an unequivocal no. In this case, the exit time rises at a rate $1/r$, where r is the probability that the less likely force is applied. Thus, in a model in which the voters care much more about conforming than being consistent, the exit time can be substantial. And, even in models with small numbers of agents and few dimensions, as $r \rightarrow 0$, the exit time goes to infinity.

This last result is of mathematical interest because it shows how exit times can have a nonlinear relationship to the relative weights of forces. Empirically, the result tells us something about the persistence of heterogeneity. Models of cultural convergence and genetic drift show a quick dampening of diversity as do simple models of dissonance reduction. Adding the two forces, as we have shown, reveals much longer exit times, particularly when one force is stronger than the other. Thus, a society (resp. political party or species) may take a long time converge to a consistent culture (platform, or genetic sequence) even though the forces are in place for that to happen. If one force is very weak, the exit time may be so long that we would expect the system to not attain it in any practical time frame. As a result, heterogeneity would persist. Moreover, if we add even a tiny bit of noise to this generalized model, we find stable levels of heterogeneity that far outstrip those produced by the standard voter model [20].

2.2 A generalized voter model on complex networks

The voter model has also been extensively studied on lattices [108] and, in recent years, on complex networks [170, 162, 157, 161, 37]. It is closely related to a variety of models of language evolution [17], ecological dynamics [82], opinion dynamics [36],

and epidemic spread [137]. As described above, the voter model defines a dynamical process where nodes are each assigned one of two states, $+1$ or -1 . Connections are defined on a lattice by nearest neighbors or on an arbitrary network by edges. Each update step consists of selecting a pair of nodes and giving the state of one node to the other. In the most frequently studied version of the model, the first node chosen adopts the state of the second. For the traditional voter model on complex networks, a node is chosen second with frequency proportional to its degree, and so its influence is fixed by the selection process. Here, we introduce a generalized voter model with a single tunable parameter that allows control of the influence of topology in a manner independent of the selection process. In this generalized model, the probability of a node giving its state to its neighbor is proportional to k^α , where k is the node's degree and α is chosen.

We focus our attention on the mean exit time, i.e. the mean time to achieve consensus. It has been frequently seen that voter model dynamics follow a two step relaxation process [157, 18]. The state of the system first decays exponentially to an ensemble average state, then fluctuates diffusively around this value until consensus occurs. We find similar behavior in our model, but also observe a frustrated state that prevents the system from reaching the ensemble average value.

Voter model processes based entirely on selection frequency are denoted either *link update* or *node update* [161]. In link update dynamics, every time step an edge is selected uniformly at random. One of the two nodes at the ends of the link is then chosen randomly to give its state to the other. In node update dynamics, the traditional definition of the voter model on complex networks, a node is selected to adopt the state of a random neighbor. For random networks, the neighbor is more likely to be connected to a high degree node than low degree, so high degree nodes

have more influence.

2.2.1 A generalized voter model

The two processes described above specify both the selection of a pair of interacting nodes and which node adopts the state of the other. We separate this process into two distinct steps to better understand the contribution of each aspect of the process. Where edge update and node update dynamics differ in the following, we attach a superscript \mathcal{E} and \mathcal{N} , respectively, to the relevant quantity.

Given a network of size N , each node i has state $s_i = \pm 1$ and degree k_i . We define P_{ij} to be the probability of giving to node i the state of node j during a given time step. There are two independent components of this event: the probability S_{ij} of selecting an edge connecting nodes i and j and the probability $W(k_i, k_j)$ that a node with degree k_j gives its state to a node with degree k_i . Thus,

$$P_{ij} = S_{ij}W(k_i, k_j). \quad (2.24)$$

The form of $W(k_i, k_j)$ is motivated by comparison with node update dynamics in uncorrelated networks. Under the node update process, the probability of giving node i with degree k_i the state of node j with degree k_j is

$$P_{ij}^{\mathcal{N}} = \frac{A_{ij}}{Nk_i} \quad (2.25)$$

where A_{ij} is an element of the adjacency matrix, which has a value of 1 if the nodes share an edge and 0 otherwise. This can be interpreted as the probability $1/N$ of selecting i times the probability $1/k_i$ of following one particular edge out. If node pairs are selected in this manner, ignoring direction, a particular pair of nodes i and j can be chosen by either picking i and following an edge to j or by picking j and

following an edge to i . This gives

$$S_{ij}^{\mathcal{N}} = \frac{A_{ij}}{N} \left(\frac{k_i + k_j}{k_i k_j} \right). \quad (2.26)$$

We propose a generalization that includes the standard node update dynamics, which requires $S_{ij}^{\mathcal{N}} W(k_i, k_j) = P_{ij}^{\mathcal{N}}$. The only form of $W(k_i, k_j)$ to do this is

$$W(k_i, k_j) = \frac{k_j}{k_i + k_j}. \quad (2.27)$$

This form is consistent with our desire that $W(k_i, k_j)$ be a probability. It also suggests a one parameter generalization, which forms the basis for the rest of this section:

$$W(k_i, k_j, \alpha) = \frac{k_j^\alpha}{k_i^\alpha + k_j^\alpha}. \quad (2.28)$$

Qualitatively, the parameter α determines how much a node asserts its degree when transmitting its state. For $\alpha > 0$, the higher degree node of a pair is more likely to give its state to the lower degree node, a bias that increases with α . For $\alpha < 0$, the opposite is true. The special case $\alpha = 0$ ignores topology in determining the direction of interaction since $W(k_i, k_j, 0) = 1/2$ always. Node update dynamics occur when node selection determines pairs and $\alpha = 1$. A recently investigated “invasion” dynamic, where a node is picked to give its state to a random neighbor (opposite the traditional model), occurs for node selection and $\alpha = -1$ [35]. If all nodes of the network have the same degree, as in a mean field or lattice topology, then all values of α are equivalent to the traditional voter model. It can also be applied to other methods of pair selection. Traditional edge update dynamics are attained for $S_{ij}^{\mathcal{E}} = 1/M$, where M is the total number of edges, and $\alpha = 0$.

This process describes a situation where there is a particular connection between the behavior of the agents and the underlying network on which they live. For example, if this process were to be thought of in the context of opinion dynamics, a

value of $\alpha > 0$ would correspond to an individual preferring to think like those who are more connected than those who are less connected. The forces of influence and accessibility compete, such that a small value of α makes all nodes accessible enough to change state quickly, but limits the influence of any one node. A high value of α makes high degree nodes influential, thus able to order their neighborhoods quickly, but those influential nodes themselves will flip only on rare occasions.

To understand the outcome of this process, we will consider the master equation for an arbitrary network. The probability of a system being in state $\mathbf{s} = \{s_i\}$ at time t is defined to be $P(\mathbf{s}, t)$. Denote by \mathbf{s}^i the state \mathbf{s} where $s_i \mapsto -s_i$ and let S_{ij} be the probability of selecting the edge between nodes i and j , irrespective of update type. For brevity, we write $W(k_i, k_j, \alpha) = W_{ij}^\alpha$. The master equation is

$$\frac{d}{dt}P(\mathbf{s}, t) = \sum_{ij} S_{ij} W_{ij}^\alpha \left(\frac{1 + s_i s_j}{2} \right) P(\mathbf{s}^i, t) - S_{ij} W_{ij}^\alpha \left(\frac{1 - s_i s_j}{2} \right) P(\mathbf{s}, t). \quad (2.29)$$

Let $\langle s_i \rangle$ be the ensemble average probability of node i being in a $+1$ state. The evolution of arbitrary ensemble average functions can be found in a straightforward manner [100], giving

$$\frac{d\langle s_i \rangle}{dt} = \sum_j S_{ij} W_{ij}^\alpha (\langle s_i \rangle - \langle s_j \rangle). \quad (2.30)$$

We find a conserved magnetization, ρ^* , by choosing coefficients C_i such that

$$\frac{d\rho^*}{dt} = \sum_i C_i \frac{d}{dt} \langle s_i \rangle = 0. \quad (2.31)$$

Since S_{ij} is symmetric in i and j , this happens for arbitrary networks only if

$$C_i W_{ij}^\alpha = C_j W_{ji}^\alpha, \quad (2.32)$$

which implies that $C_i \propto k_i^\alpha$. Normalizing,

$$\rho^* = \frac{\sum_i k_i^\alpha \langle s_i \rangle}{\sum_i k_i^\alpha} = \frac{1}{N\mu_\alpha} \sum_i k_i^\alpha \langle s_i \rangle \quad (2.33)$$

where μ_α is the α^{th} moment of the degree distribution. Note that the ensemble conserved magnetization is independent of the process of selecting node pairs.

2.2.2 Bipartite Network

The simplest topology with heterogeneous degrees is the fully connected bipartite network. Such a network is given by two groups of nodes, group A with size a and group B with size b . A node in group A is connected to every node in group B , but none in group A , and vice versa. The degree of nodes in A , k_A , is the size of B , giving $k_A = b$ and similarly $k_B = a$. In this situation all edges are interchangeable, so there is no difference between the two selection processes and we need only to consider the effect of α . Let ρ_a be the concentration of +1 opinions in A and ρ_b be the concentration of +1 opinions in B . In our model, the special value $\alpha = 1$ is equivalent to the case studied in [157] on the same network and we follow a similar procedure, omitting details that can be found there. From Equation (2.33), the conserved magnetization is

$$\rho^* = \frac{1}{a^{\alpha-1} + b^{\alpha-1}} (b^{\alpha-1} \rho_a + a^{\alpha-1} \rho_b) \quad (2.34)$$

For any initial conditions, the ensemble average subgraph densities approaches ρ^* . If all nodes in A start as +1 and all nodes in B start as -1, then the probability of ending in the +1 state is

$$P_+ = \frac{b^{\alpha-1}}{b^{\alpha-1} + a^{\alpha-1}}. \quad (2.35)$$

The mean exit time T_α is given by the backward Komologorov equation [143]. T_α

solves

$$-\frac{a^\alpha + b^\alpha}{a+b} = (\rho_a - \rho_b)(b^{\alpha-1}\partial_b - a^{\alpha-1}\partial_a)T + \frac{1}{2}(\rho_a + \rho_b - 2\rho_a\rho_b)(a^{\alpha-2}\partial_a^2 + b^{\alpha-2}\partial_b^2)T. \quad (2.36)$$

where ∂_a and ∂_b are partial derivatives with respect to the initial subgraph densities. The first term describes convection, which brings the subgraph densities to some equal value, and the second term describes the diffusion of the network-wide state [157]. The convective dynamics can be shown to be fast for all α .

The fast step toward equal subgraph densities has a negligible impact on extinction time and we can consider only the subsequent one dimensional problem. We define $\rho = \rho_a = \rho_b$ and apply a change of variables using Equation (2.34). After integrating,

$$T = -(a^{1-\alpha} + b^{1-\alpha})(a^{\alpha-1} + b^{\alpha-1}) \times \frac{ab}{a+b}(\rho \log(\rho) + (1-\rho) \log(1-\rho)). \quad (2.37)$$

This has a similar form to the standard voter model, but with a factor that is symmetric about $\alpha = 1$. If we take $a = \lambda b$, then

$$T \propto (2 + \lambda^{1-\alpha} + \lambda^{\alpha-1}) \frac{\lambda}{1+\lambda} b. \quad (2.38)$$

If $\lambda \gg 1$, corresponding to a star-like graph,

$$T \sim \lambda^{|\alpha-1|} b. \quad (2.39)$$

This scaling is confirmed in simulations (see Figure 2.6). Notably, the standard voter model, $\alpha = 1$, is the fastest process for any complete bipartite network.

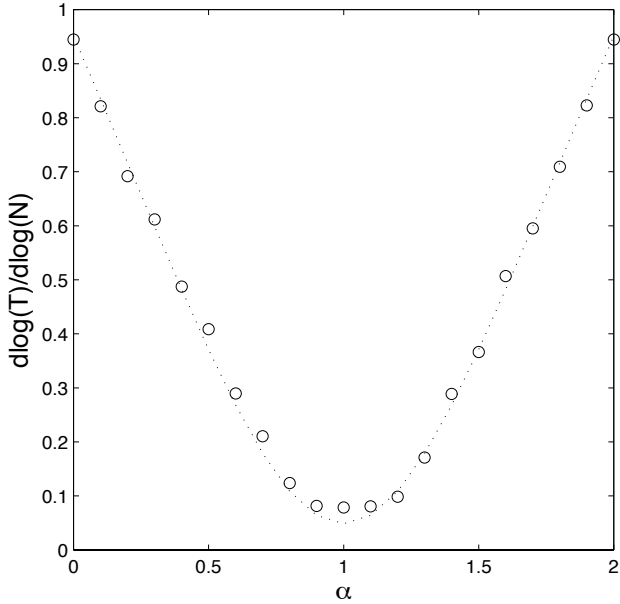


Figure 2.6: Circles are the simulated fit of $d \log T/d \log N$ for a complete bipartite network with groups of size $M = 40$ and N ranging from 100 to 5000. The dotted line is the scaling of Equation 2.39 for the same range of N .

2.2.3 Random scale-free networks

Similar analysis extends naturally to networks in which a node's degree determines the network structure. Many random network models fall into this category, including any random network generated by the configuration model, like those with scale-free distributions, and Erdos-Renyi networks [118]. Small world networks are not included, however, as certain nodes have exceptional topological characteristics that are independent of their degree [175].

As in Equation (2.36), we can write the equation satisfied by the mean exit time on an arbitrary network. For the remainder of this section, ρ_l refers to the density of +1 states on the subgraph of nodes with degree $k_l = l$. The backwards Komolgorov

equation now reads

$$\begin{aligned} -\delta_t = & \sum_{lm} S_{lm} W_{lm}^\alpha (\rho_l - \rho_m) \delta_i \partial_l T \\ & + \frac{1}{2} \sum_{lm} S_{lm} W_{lm}^\alpha (\rho_l + \rho_m - 2\rho_l \rho_m) \delta_l^2 \partial_l^2 T \end{aligned} \quad (2.40)$$

There is, in general, a prefactor to the term $\rho_l(1-\rho_l)$ when evaluating the probability that two nodes have differing states [170]. Numerical simulations show that this is of order one and not generally a constant over time when $\alpha \neq 1$, so it does not affect the final scaling results. The system is again split into a convective term and a diffusive term, however the assumption of fast approach to well-mixed state must be treated more carefully in our generalized model. However, since it was observed in [157] that node update dynamics on a scale free network has fast convection compared to its diffusive exit time, we know that a diffusion-dominated state exists.

We expect that this is not true for all α , though. In the case of $\alpha \gg 1$, a node with degree higher than all its neighbors will act to dictate its neighbors' states, but only rarely be changed itself. The network in this case may not be able to quickly approach the global equilibrium given by ρ^* , since these locally highest degree nodes will be pinned for a time dependent on α . If this duration is longer than the time for the rest of the system to become ordered via drift and diffusion, a quasi-frustrated state occurs. The specific local topology, rather than just degree distributions, dominates the dynamics.

Let us suppose that the exit time is diffusion dominated and then return to discuss the validity of this assumption later. The system can be approximated by a one dimensional equation in $\rho = \frac{1}{\mu_\alpha} \sum_l n_l l^\alpha \rho_l$, where n_l is the fraction of nodes with degree l .

$$-N = \frac{1}{\mu_\alpha^2} \left(\sum_{lm} S_{lm} W_{lm}^\alpha l^{2\alpha} \right) \rho(1-\rho) \partial_\rho^2 T. \quad (2.41)$$

And thus

$$T \propto \frac{N\mu_\alpha^2}{\sum_{lm} S_{lm} W_{lm}^\alpha l^{2\alpha}}. \quad (2.42)$$

The denominator can be simplified by noting that

$$\begin{aligned} \sum_{lm} S_{lm} W_{lm}^\alpha l^{2\alpha} &= \frac{1}{2} \left(\sum_{lm} S_{lm} W_{lm}^\alpha l^{2\alpha} + \sum_{lm} S_{lm} W_{ml}^\alpha m^{2\alpha} \right) \\ &= \frac{1}{2} \sum_{lm} S_{lm} l^\alpha m^\alpha. \end{aligned} \quad (2.43)$$

This gives:

$$T \propto N \frac{\mu_\alpha^2}{\sum_{lm} S_{lm} l^\alpha m^\alpha}. \quad (2.44)$$

Since S_{lm} is a probability, the sum can be thought of as a weighted average over selection probabilities. Interestingly, for $\alpha = 0$, neither the form of interaction selection nor the network topology matter. In that case, $\mu_0 = 1$ and $W_{ij} = 1/2$, so

$$T_{\alpha=0} \propto N. \quad (2.45)$$

This agrees with the observation in [162] that exit times scale with N in situations where the unweighted magnetization is conserved, which corresponds to $\alpha = 0$.

To go farther, we need to specify the selection scheme and the network. We focus our consideration on random uncorrelated scale-free networks with degree distribution $n_k \sim k^{-\nu}$. Networks with power law distributions appear in a variety of social and biological contexts and exhibit a range of interesting behaviors [118]. Let us first consider node update, for which $S_{lm}^N = n_l n_m \frac{l+m}{2\mu_1}$. Then Equation (2.44) becomes:

$$T^N \propto N \frac{\mu_1 \mu_\alpha}{\mu_{\alpha+1}}. \quad (2.46)$$

The α^{th} moment can be approximated by an integral:

$$\mu_\alpha \sim \int^{k_{max}} k^\alpha n(k) dk \quad (2.47)$$

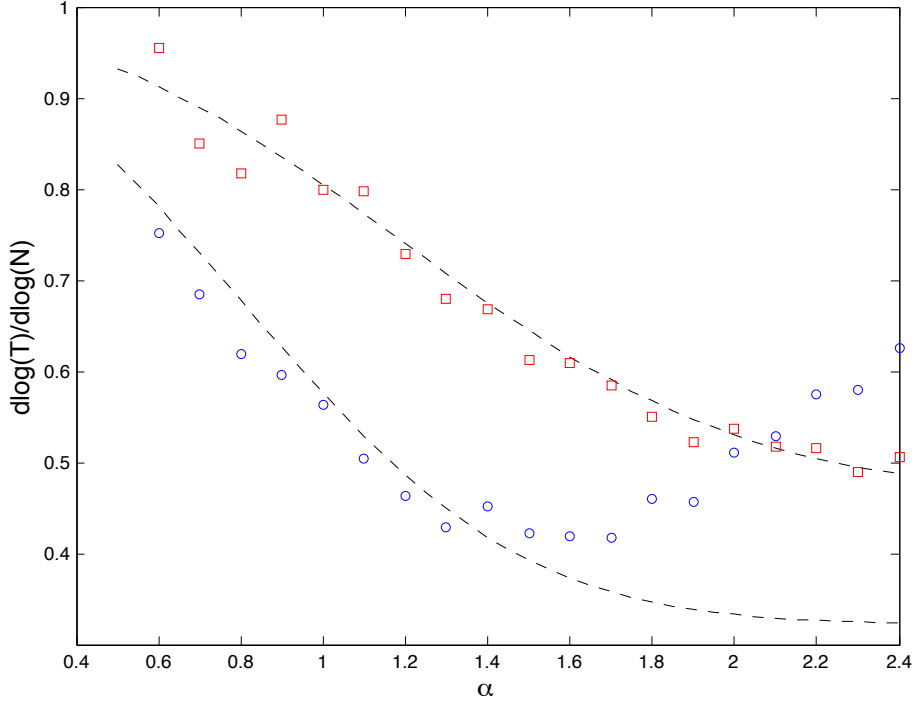


Figure 2.7: Simulated values of $d \log T / d \log N$ under node selection based on several hundred runs for N from 750–15000. Squares correspond to $\nu = 2.8$, circles to $\nu = 2.4$. The dashed line is the scaling based on the diffusive estimate, calculated by fitting the numerically calculated sum in Equation 2.44 for similar values of N . Note that frustration begins to dominate for $\nu = 2.4$ at $\alpha > 1.6$, causing the deviation from the diffusive estimate.

up to an effective maximum degree k_{max} , defined by $\int_{k_{max}}^{\infty} n(k) dk = 1/N$ [101]. It is easily seen that $k_{max} \sim N^{1/(\nu-1)}$.

$$T^N \propto \begin{cases} N^{\frac{\nu-2}{\nu-1}} & \alpha > \nu - 1 \\ N^{\frac{2\nu-\alpha-3}{\nu-1}} & \nu - 2 < \alpha < \nu - 1 \\ N & \alpha < \nu - 2 \end{cases} \quad (2.48)$$

For $\nu > 2$ and any α , the exit time increases without bound as system size increases. We simulated the process on random network generated by the configuration model [115] and found good agreement with our predictions (see Figure 2.7).

For edge update dynamics, $S_{lm}^E = n_l n_m \frac{l_m}{\mu_1^2}$. Low degree nodes are selected less

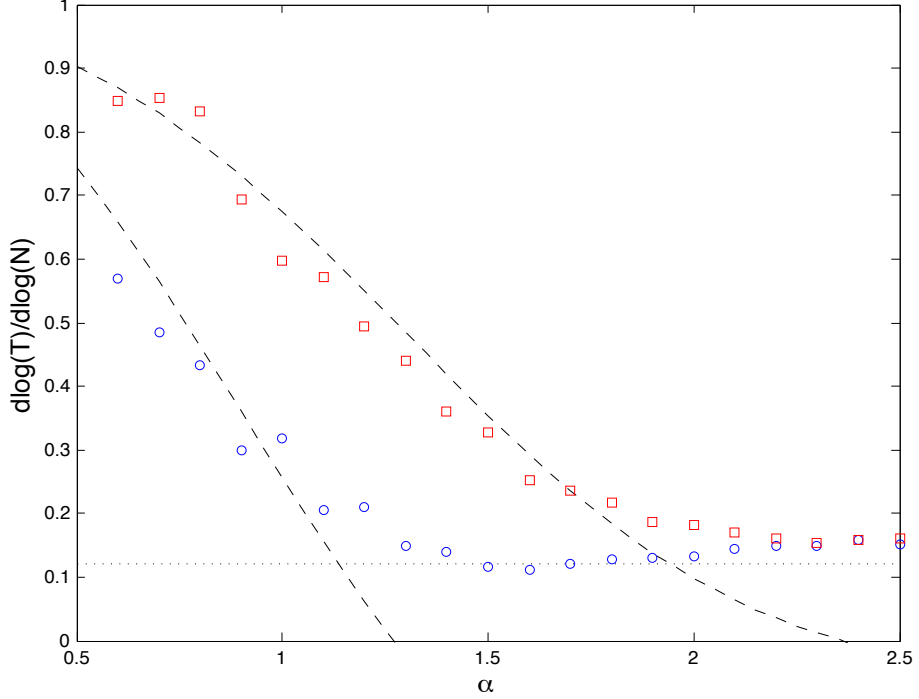


Figure 2.8: Simulated values of $d \log T / d \log N$ under edge selection from several hundred runs of values of N from 750–15000. Square are for $\nu = 2.8$, circles for $\nu = 2.4$. The dashed line comes from fitting the numerically calculated sum in Equation 2.44 for similar values of N . The horizontal line is the effective slope of $T \sim \log N$ for the system sizes used.

frequently under edge selection than node selection. The diffusive exit time can be calculated similarly, giving:

$$T^{\mathcal{E}} \propto N \left(\frac{\mu_1 \mu_{\alpha}}{\mu_{\alpha+1}} \right)^2. \quad (2.49)$$

The approximate scaling for edge update is

$$T^{\mathcal{E}} \propto \begin{cases} N^{\frac{\nu-3}{\nu-1}} & \alpha > \nu - 1 \\ N^{\frac{3\nu-2\alpha-5}{\nu-1}} & \nu - 2 < \alpha < \nu - 1 \\ N & \alpha < \nu - 2 \end{cases} \quad (2.50)$$

This leads to very different scaling behavior. For the parameter regions

$$\nu < 3 \quad \alpha > \nu - 1 \quad (2.51)$$

$$\nu < \frac{2\alpha + 5}{3} \quad \nu - 2 < \alpha < \nu - 1 \quad (2.52)$$

the diffusive exit time vanishes as N increases. Simulations show that there is a diffusive region which agrees with our predictions for smaller values of α (see Figure 2.8).

The convective process involves an exponential decay of each ρ_i to its ensemble equilibrium value, with rate determined by the network structure. For larger values of α , the state of the highest degree node comes to dominate the value of ρ^* . This causes ρ^* to be either extremely close to 0 or extremely close to 1, so the result of diffusive drift is close to a consensus state. Simulations for this region are consistent with either a very small power law scaling of $T^\varepsilon \propto N^{0.12}$ or $T^\varepsilon \propto \log(N)$ (Figure 2.8). The latter case would arise if the diffusive time is short compared to the drift time over the range of system sizes tested, consistent with observations (see inset, Figure 2.11) of dynamics for these values. Note that this case only is observed under edge selection.

A third regime is apparent when one considers the limit that $\alpha \rightarrow \infty$. In this limit, $\rho^* = s_{max}$, where s_{max} is the initial state of the highest degree node, either 0 or 1. However, since $W_{ij}^\infty = 0$, any node i whose degree is higher than all of its neighbors will take an arbitrarily long time to flip. Such nodes will be called “local leaders,” following [23]. The network enters a frustrated state where the convection does not exponentially drive the system to a global state ρ^* . As a result, the time to convergence is dominated by individual nodes and local topology, not global network properties (Figure 2.11). An illustration of this is shown for a small network in (Figure 2.9).

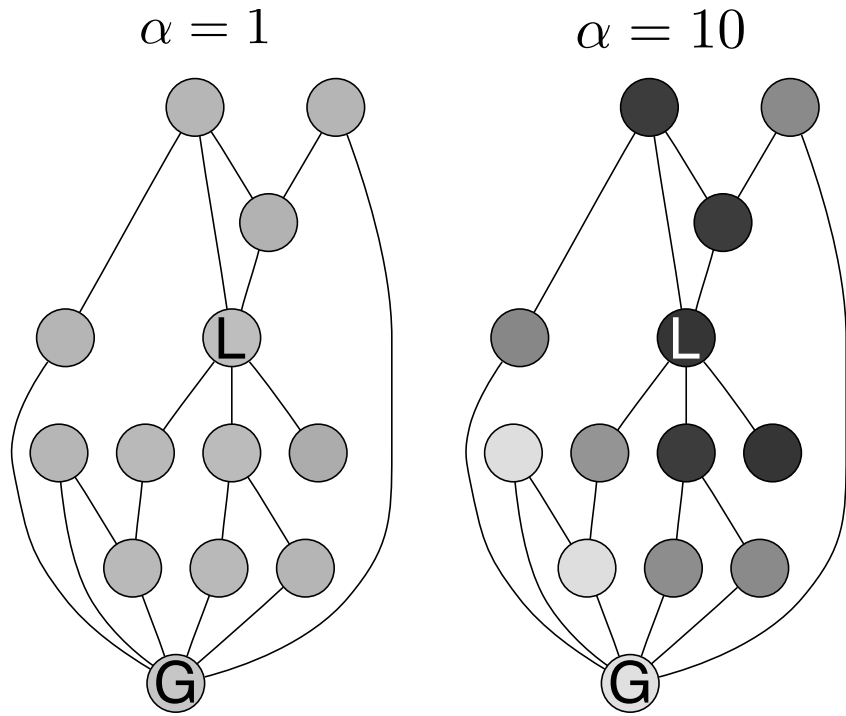


Figure 2.9: A example of node update dynamics on a small network containing a global highest degree node (G) and a separate local highest degree node (L) for $\alpha = 1$ and $\alpha = 10$. The darkness of a node corresponds to the average fraction of time spent in a state opposite the final state of the network over 1000 realizations with identical initial conditions. A darker node has spent more time in a contrary state than a light node. For $\alpha = 1$, states are well mixed and $T = 9.4$. For $\alpha = 10$, the decay to the metastable value ρ^* does not occur. The local leader and its neighborhood spend most of the time in a contrary state and $T = 4814$.

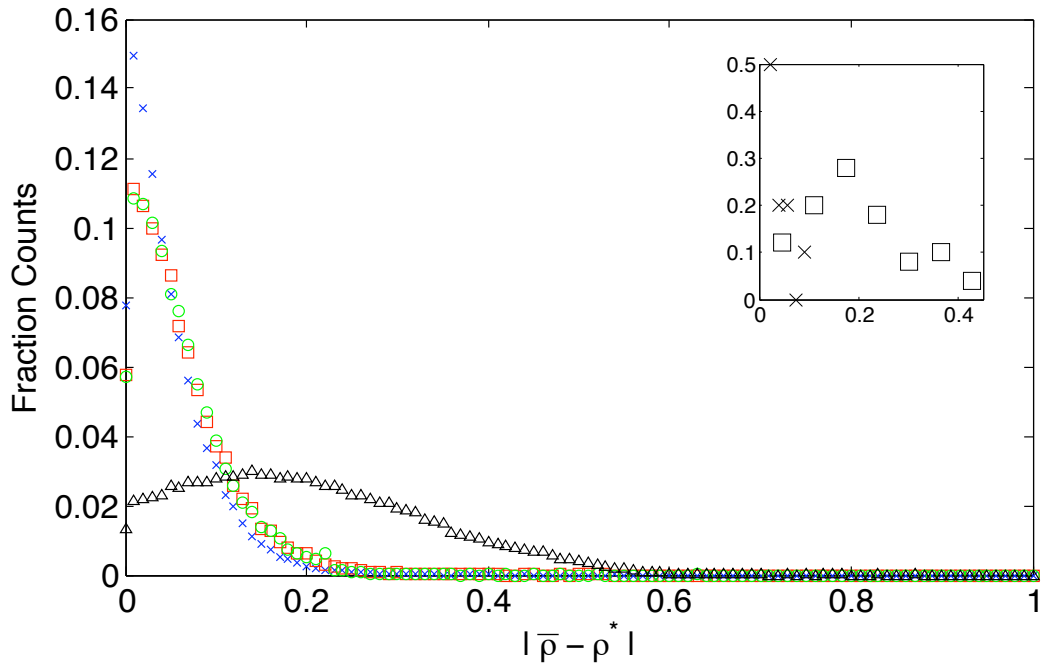


Figure 2.10: Normalized histogram of the absolute value of the time average deviation from ensemble equilibrium value ρ^* per node for $N = 3000$, $\nu = 2.4$, and $\alpha = 1$ (\times), 1.5 (\circ), 2 (\square), and 5 (\triangle) under node update dynamics, drawn over 50 (for $\alpha = 5$) or 10 (for all other α values) runs. For diffusive values of α , the deviations are gaussian and peaked around zero. For $\alpha = 5$, nodes do not center about ρ^* . The inset shows a normalized histogram of mean deviation values per network for $\alpha = 1$ (\times) and 5 (\square). The diffusive case is peaked around zero, whereas the frustrated case is broad and nonzero, showing large differences across networks.

The continuum treatment in Equation 2.40 averages over network ensembles before solving for the exit time. In the high α case, considering an averaged network ignores local leader effects and fails to give an accurate solution. The approach to an ensemble equilibrium state does not occur exponentially, so diffusion about this state is not a valid assumption (Figure 2.10). Moreover, the state at which the system becomes frustrated differs considerably between individual networks with the same degree distribution and size (inset, Figure 2.10).

The degree distribution of locally highest degree nodes can be approximated for the non-assortative case quite simply. The degree distribution of local leaders, $p_{ll}(k)$, is the independent product that a node has degree k and that all k neighbors have a degree less than k [23]:

$$p_{ll}(k) = p(k) \left(\sum_{k' < k} \frac{k' p(k')}{\mu_1} \right)^k. \quad (2.53)$$

No term is strongly related to system size, so the total number of local leaders N_{ll} scales linearly with N .

The dynamics of these nodes are based on extremely local behavior and thus very hard to approximate, but we can construct the slowest possible node and consider its behavior. For a sufficiently large system, one such node will likely exist and thus dominate the exit time. The probability on any given time step t to flip a local leader i with degree k_i is formally given by:

$$P_{flip}(k_i, t) = \sum_j S_{ij} \frac{k_j^\alpha}{k_i^\alpha + k_j^\alpha} P(\sigma_i \neq \sigma_j, t) \quad (2.54)$$

where $P(\sigma_i \neq \sigma_j, t)$ is the probability that the neighboring state differs from the local leader's state at time t .

Even neglecting the probability of differing states, the probability of a local leader adopting the state of a neighboring node has interesting properties. Assuming in-

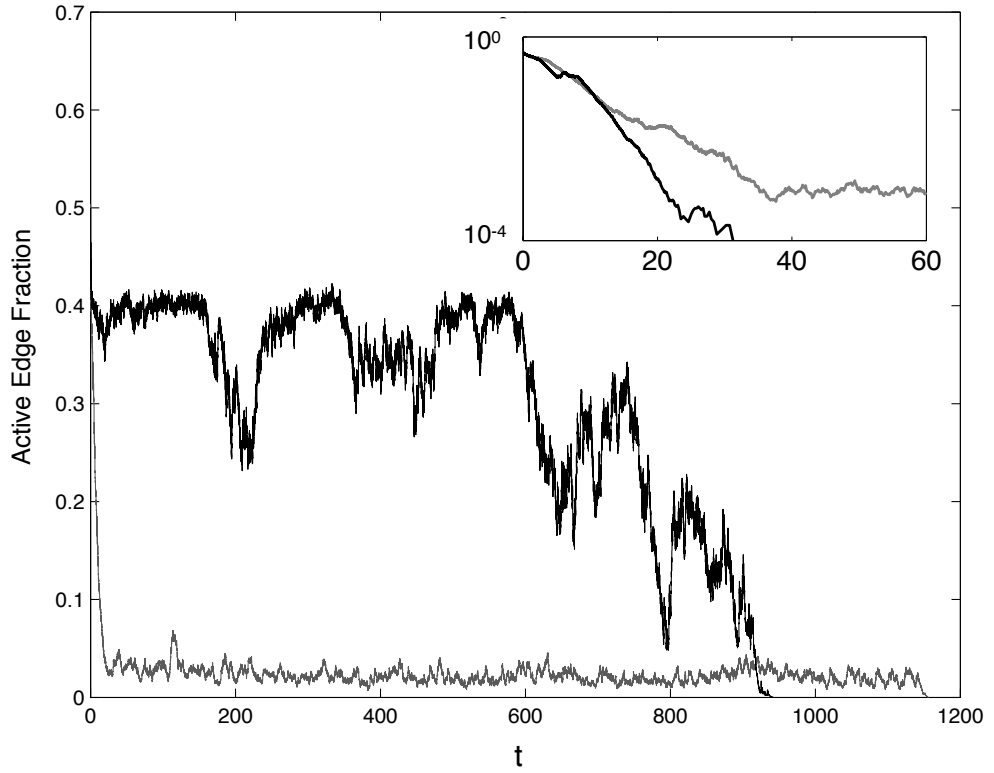


Figure 2.11: Typical dynamics of the fraction of active edges (edges connecting nodes with different states) for diffusion and frustration. Both have $N = 10000$, $\nu = 2.8$, and edge selection. The top line, in black, is for $\alpha = 1$ and the bottom line, in gray, is for $\alpha = 8$. The $\alpha = 1$ case is diffusive and fluctuates to convergence after reaching the ensemble average value. The $\alpha = 8$ case decays exponentially to a value greater than the ensemble average value, because a locally highest degree node or cluster is slow to flip. Just before $t = 1200$, these nodes flip and the system reaches the absorbing state. Inset shows early time dynamics on a similar network for $\alpha = 10$ in gray and $\alpha = 4$ in black. Both decay exponentially initially, but the high α case becomes frustrated and the other continues to convergence.

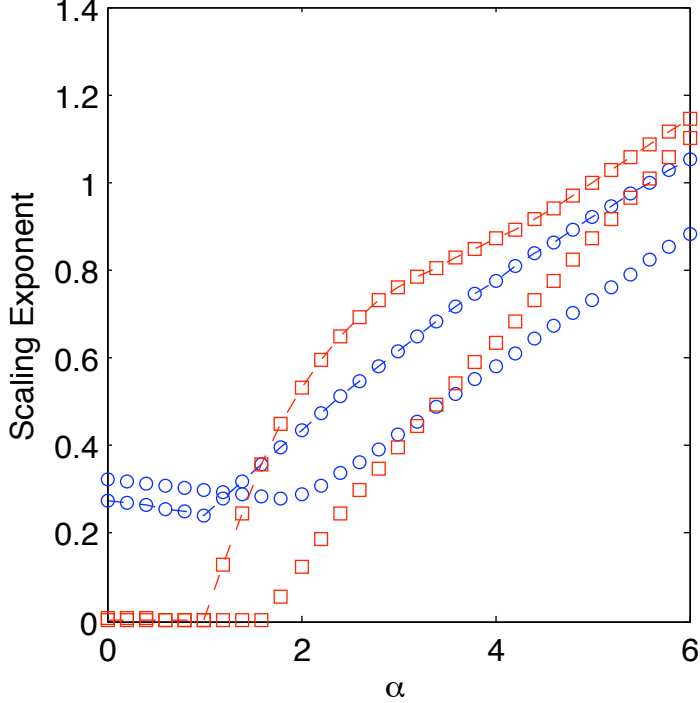


Figure 2.12: The scaling of mean time for the most isolated local leader to adopt the state of a neighbor, based on 1000 networks and $N=1000\text{--}32000$. Circles are for $\nu = 2.4$, squares for $\nu = 2.8$, connecting lines indicate node update, markers only indicates edge update. Note that this ignores the probability that a neighbor has an opposite state, therefore certainly underestimating the time to flip, but still gives qualitative agreement to the behavior observed in simulations.

dependence of the behavior of different local leaders in the same network, the mean time to take on a neighboring state is easy to calculate for a given node. From simulations, the mean time to flip of the most isolated local leader (who is not also the global leader) scales with system size as shown in Figure 2.12. While this does not have quantitative agreement with time to consensus, the qualitative behavior is consistent. Local leaders see outside states more rarely under node update than link update and the onset of slow flipping of local leaders starts earlier for $\nu = 2.4$ than $\nu = 2.8$.

2.2.4 Summary

Recent work [18] has found an approximate mean exit time for a duplication process on networks with arbitrary edge weights, assuming that diffusion is the dominant time scale. Our model can be considered a weighted directed network where the weight of an edge from i to j is given by W_{ij}^α , so it fits into the framework described. In this work, we demonstrate that there are at least two natural ways for this estimate of exit time to fail. As previously observed in Baxter *et al.*, the time for the system to reach a metastable equilibrium can be at least as large as the diffusive exit time scale. We see this in the edge selection process for values of α and ν where the diffusive exit time vanishes as system size gets large. The frustrated dynamics in the node selection mode, however, presents a new way in which the diffusive estimate can fail. System dynamics are driven by a small number of topologically special nodes, breaking the assumption that a continuum description applies.

More important than the specific model we have presented is the lesson about processes on scale-free networks. Because random scale-free networks are well known to exhibit large deviations, small differences in stochastic processes performed on them can create large differences in resulting behavior. In our model, the seemingly modest transition between node selection and edge selection radically changed the scaling of consensus time with system size, with edge selection being able to reach consensus much faster than node selection for the same ensemble average magnetization. Moreover, slight changes in the role of degree were able to induce a transition between a regime with an exit time dictated by global topology to one where it is dominated by particular local features of the network.

CHAPTER III

Glioblastoma Pattern Formation

The behavior of a glioblastoma multiforme (GBM) cell, or any other eukaryotic cell for that matter, can hardly be called a simple process. Certain aspects, however, can be beneficially analyzed with simple, phenomenological models. In this chapter, we consider how varying cell-cell adhesion strengths affects pattern formation. Unlike the adatoms and spins of traditional physics, one of the primary differences here is that cells can proliferate, which allows a wholly new mechanism for cluster growth.

The work presented here was part of a mid-sized collaboration on GBM invasion and motility with Chiocca group in the department of Neurosurgery at the Ohio State University Medical Center, the Berens lab at the Translational Genomics Research Institute, the Deisboeck group at Massachusetts General Hospital, and the Weitz lab in the physics department at Harvard University. My primary contribution was on the analysis of 3d cell paths using experimental data from the Berens and Chiocca labs. Spheroids made of several thousand fluorescently labeled GBM cells would be implanted into a collagen matrix and left to invade into it for 40 hours. Several times an hour, a set of image slices would be taken at sequential depths through the gel, giving a fully 3d description of the locations of cells in the assay. From this data set, I pieced together and analyzed the trajectories of cells that left the spheroid (e.g.

Figure 3.1).

Having full, independent trajectories allowed us to directly measure various aspects of shedding and invasion that in which we were interested. For example, unlike measurements of bulk populations where you can only rely on fitting, I could easily count the number of cells that left a spheroid comprised of a given cell line. This chapter is derived from work done in collaboration with Evgeniy Khain of the Oakland University Department of Physics, Len Sander, and Oskar Nowicki, Sean Lawler, and Antonio Chiocca of Ohio State University and published in [96]. We use the continuous time shedding data to determine parameters in the phenomenological description. It is based in large part on earlier work I did with Evgeniy Khain and Len Sander, with the same Ising-like model applied to a wound healing geometry where the initial condition assumes a confluent layer of cells instead of a diffuse cloud of cells [95].

3.1 Introduction

The process of tumor growth has attracted a good deal of attention in the physics community in recent years [166]. In addition to its medical importance, it presents an exciting example of pattern formation [52] and collective cell behavior [46] in intrinsically non-equilibrium systems. One of the rapidly developing areas of tumor growth studies is a theoretical and computational investigation of glioblastoma multiforme [46], the most malignant of primary brain tumors. Malignant gliomas are not treated effectively by current therapies, partly due to the fact that GBM is highly invasive [49]. Indeed, glioma cells not only proliferate, but detach from the primary tumor and migrate away into the extracellular matrix. To mimic the *in vivo* avascular tumor growth, the *in vitro* growth of multicellular tumor spheroids is

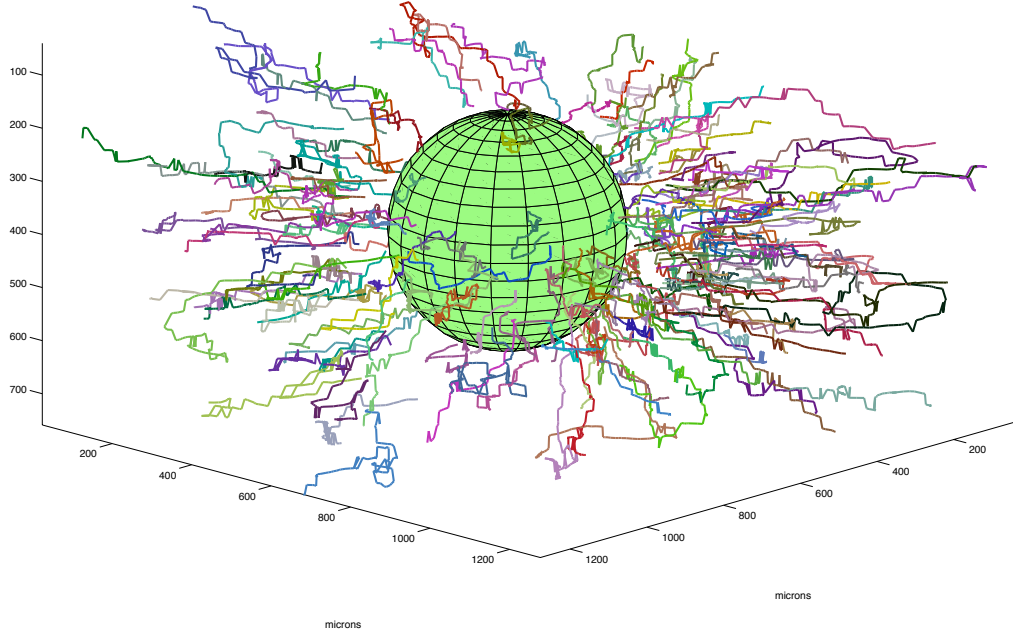


Figure 3.1: Paths from a hanging drop spheroid assay of the X12 glioblastoma cell line.

frequently considered [56]. In recent experiments, *in vitro* glioma growth (starting from a small tumor spheroid) was investigated in a transparent gel for two cell lines, U87WT (wild type) and U87 Δ EGFR [159]. In the second case, there is a mutation that is known to lead to enhanced malignancy [121]. In the experiment, the growing spheroid of glioma cells (the proliferative zone) is surrounded by zone of low-density motile cells known as the invasive zone. This morphology is similar to what happens in the brain where deadly recurrent tumors form via motile invasive cells. In the experiments Δ EGFR forms small clusters of cells in the invasive region, but WT does not [159]. It is probable that the mutation in the Δ EGFR line, which is known to make the EGF receptors constitutively active, also causes these cells to be more adhesive than the WT line, and this results in enhanced clustering. These clusters

may give a clue to the formation of recurrent brain tumors. The investigation of the mechanism of the clustering glioma cells is the subject of the present work.

In a growing tumor, the maximal proliferation activity occurs at the tumor border [28, 69]. Cells in the invasive and proliferative zones differ in phenotype: compared to cells in the inner proliferative zone, individual invasive cells have a much lower proliferation rate [69]. This dichotomy between invasive cells (which rapidly migrate but rarely proliferate) and proliferative cells located on the tumor surface has begun to be addressed theoretically [93, 159, 61].

3.2 Glioma clustering

To investigate clustering, we did an experiment to follow the clustering of glioma cells on a surface. On a substrate, glioma cells migrate, proliferate and experience cell-cell adhesion. One can define a characteristic time for migration, τ , as a time required for a cell to move its own diameter (of the order of $10\mu m$). The motion of cells is an active (and highly complicated) process. Many experiments have shown that the motion is not purely diffusive (even in the absence of chemotaxis) but shows persistence on small scales [50, 76]. However, on length scales larger than the persistence length, random motion is a reasonable approximation. The characteristic migration time τ can be found from the analysis (tracking) of the cell trajectories on a substrate [76]. Figure 1b in [76] shows the displacement of glioma cells migration versus time. On scales much larger than the cell diameter, this motion looks like diffusion with an effective diffusion time of 4 minutes. The effective migration time in our experiments is of the same order of magnitude. The typical time for proliferation is much larger, of the order of one day. However, the rate of proliferation depends on cell phenotype.

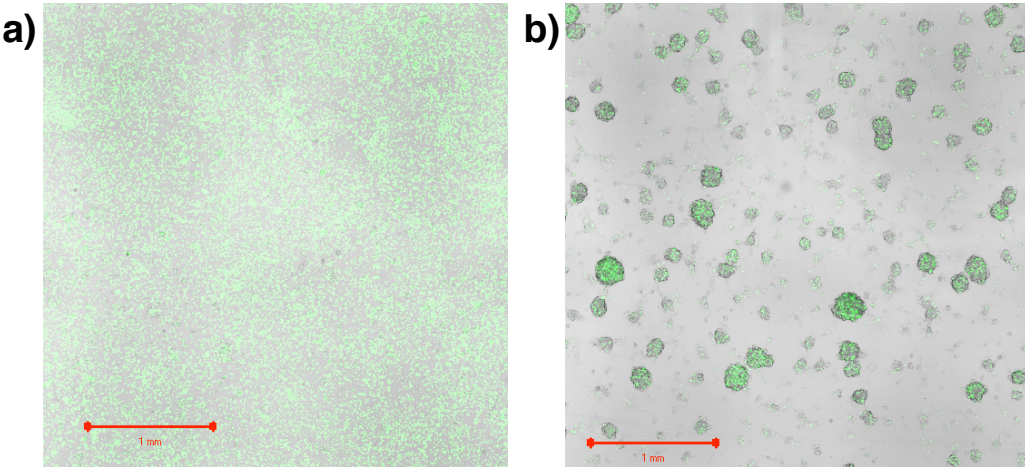


Figure 3.2: Snapshots of the system for the two cell lines five days after the beginning of the experiment. ΔEGFR (b) cells form clusters, while WT cells (a) are homogeneously distributed over the system.

In the experiment, we directly compared a low-density preparation of U87WT and U87 ΔEGFR cell lines. The cells were seeded on plastic Petri dishes at 50 percent initial confluence. Images were taken every 24 hours with a Zeiss LSM510 confocal microscope. Bright field images were captured on a transmitted light detector; cells were marked with GFP (green). Figure 3.2 shows the experimental results 5 days after the beginning of experiment. The ΔEGFR cells form large clusters (b), while WT cells remain homogeneous (a). A typical cluster size in Fig. 3.2b is of the order of one hundred microns, so each cluster contains hundreds of cells. Since cell-cell adhesion promotes clustering, the results suggest that ΔEGFR cells are more adhesive than the wild type cells. We have measured the cluster size distribution for the ΔEGFR ; the results will be shown below. We examined the initial stages of the experiment in details. We made a movie, consisting of 50 frames with 4 minutes interval between the frames. We observed that very small clusters (that include just several cells) were formed when cells migrated, randomly approaching each other and stuck together, see Fig. 3.3.

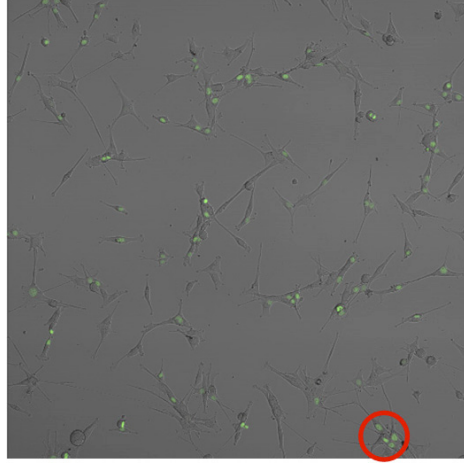


Figure 3.3: Δ EGFR cells a few hours after beginning of the experiment. Shown is a part of the system, $1400\mu m$ on $1400\mu m$. A circle shows a small cluster of cells, which randomly migrated and stuck together due to cell-cell adhesion.

In order to investigate these phenomena in detail we formulate a mathematical model for motile, proliferative and adhesive cells on a two-dimensional square lattice [95, 94]. Each lattice site can be empty or once occupied by a cell. We take the lattice distance to be equal to the cell diameter. The dynamics are as follows: a cell is picked at random. It can proliferate with probability α . If it does not proliferate, we allow the possibility of migration to a neighboring site if the site is empty. The probability for migration decreases as the number of nearest neighbors increases. In our model it is given by $(1 - \alpha)(1 - q)^n$, where $0 < q < 1$ is the adhesion parameter, and n is the number of nearest neighbors. This is a schematic representation of the underlying biology, but it is a convenient assumption. The case of no adhesion corresponds to $q = 0$. For large q , adhesion makes it quite hard to move a cell that has many neighbors. As we mentioned above, the migration time τ (the time for a cell to move one cell diameter) is much shorter than the proliferation time (the time for one cell division). Therefore, $\alpha \ll 1$. After each cell process, the time is advanced by the migration time divided by the current number of cells. Numerical solutions

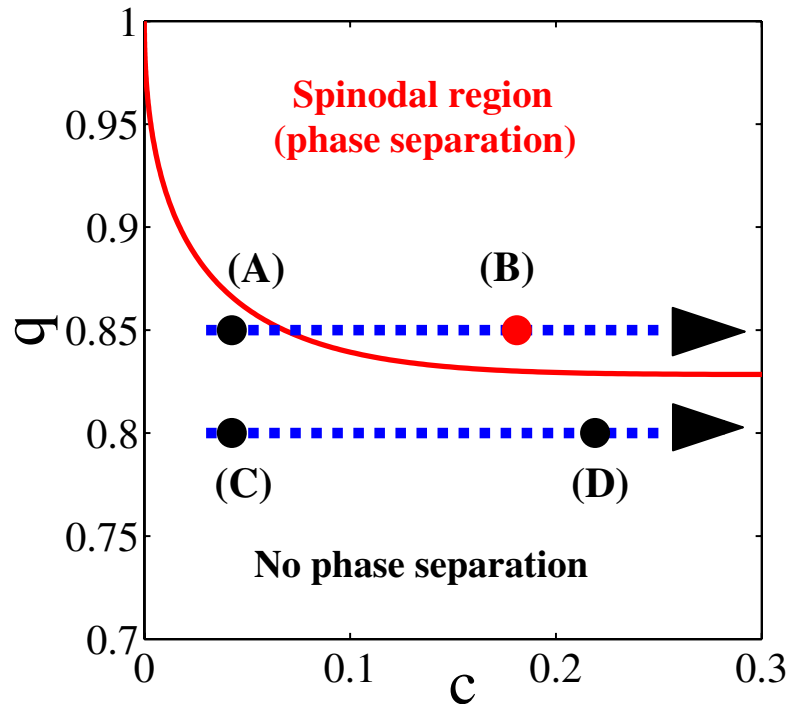


Figure 3.4: A part of the phase diagram, for small densities and large adhesion parameters. The probability of migration decreases as the number of nearest neighbors increases to account for cell-cell adhesion. A border of the phase separation region (the solid line) is given by Eq. (3.1). We start from small density and turn on proliferation. The average density of cells increases, and one can either enter the two-phase region [path (A)-(B)] or remain in the stable region [path (C)-(D)], depending on the adhesion parameter (two dotted lines).

of the model show that depending on the strength of cell-cell adhesion, we can get qualitatively different types of time evolution of the system. We also used similar model in the context of wound-healing [95].

In the case of non-proliferating cells ($\alpha = 0$), the existence of different regimes of clustering behavior is well known since our scheme can be mapped into the Ising model [81]: we identify the adhesion parameter q with $1 - \exp(-J/k_B T)$, where T is the temperature, k_B is Boltzmann's constant, and J is the coupling strength in the magnetic model. The average density of cells, c , is identified with $(m + 1)/2$

where m is the magnetization. By exploiting this mapping, we plot a phase diagram in terms of q and c for the case of no proliferation in Fig. 3.4. We present the part of the phase diagram corresponding to small c and large q . In Fig. 3.4, the solid curve separates the phase diagram into two qualitatively different regions. Below the curve, an initially homogeneous ensemble of cells remains homogeneous. Due to non-zero adhesion some small-size clusters form, but these clusters do not grow. If the cell-cell adhesion parameter exceeds a critical value $q_c(c)$ determined by [81]:

$$c = \frac{1}{2} \pm \frac{1}{2} \left[1 - \frac{16(1 - q_c)^2}{q_c^4} \right]^{1/8}, \quad (3.1)$$

we enter the region in the phase diagram where the homogeneous state becomes unstable, and there is phase separation and clustering.

For non-zero proliferation, the diagram shown in Fig. 3.4, gives only qualitative predictions, which we test numerically (see below). Nevertheless, it allows us to propose two qualitatively different scenarios of time evolution and growth of cell population depending on the strength of cell-cell adhesion. Consider an initially homogeneous system of cells with a very small density (points A and C in Fig. 3.4) and turn the proliferation on. The average density of cells increases (dotted lines), and the system either enters the two-phase region (B) or remains in the stable region (D), depending on q . For supercritical adhesion, a phase separation occurs between high density clusters and a “gas” of single cells. Then these clusters start growing mostly by proliferation (since coarsening [173] is a very slow process). If q is smaller than the threshold adhesion strength q_c , the system remains homogeneous, and the growth of cell population is entirely determined by proliferation.

It turns out that the proliferation rate α is not constant: as we mentioned above, cells on the surface of tumor spheroids (these cells are called *proliferative*) divide

much more often than single individual cells (which are called *invasive*). We incorporate this experimental observation in the model, assuming that cells located on the surfaces of clusters have an increased proliferation rate, which is denoted by α_{high} . Notice that inside the cluster cells (which have no empty neighboring sites) can not proliferate. Proliferation of invasive cells is assumed to depend on cell density: when the density is high, cells proliferate less due to contact inhibition effect. An experiment was done to quantify the proliferation rate of invasive cells. We found that it can be fitted by $\alpha(n) = \alpha_{low}(1 + n)^\beta(1 - n)$ with $\beta = 1.73$, where $0 < n < 1$ is the local area fraction and α_{low} is the basic proliferation rate for invasive cells. Invasive cells may switch their phenotype to proliferative, as they form sufficiently large cluster. Then their rate of division increases significantly from α_{low} to $\alpha_{high} \gg \alpha_{low}$.

Figure 3.5 shows the results of simulations of the discrete model, which mimic the clustering behavior of $\Delta EGFR$ cells, see Fig. 3.2b. a) An instance of $\alpha_{high} = \alpha_{low}$. b) An instance of a simulation incorporating the assumption that invasive cells switch their phenotype to proliferative (and increase their proliferation rate), when they form clusters; here $\alpha_{high} \gg \alpha_{low}$. In the latter case, number of clusters is smaller, and the clusters are sufficiently large, which better agrees with experimental observations.

In order to make a quantitative comparison between the theoretical model and experiments, we consider the cluster size distribution, $F(N)$, for $\Delta EGFR$ cells. It is hard to identify very small clusters in the experiment; thus we limit ourselves to the large N tails of the distributions, see Fig. 3.6. We measured the size of sufficiently large clusters and averaged the results over three sets of experiments. We estimated the number of particles in a cluster, assuming that the density within the cluster is about one-half the density of close packing. We performed a detailed comparison of the cluster size distribution obtained from numerical simulations with

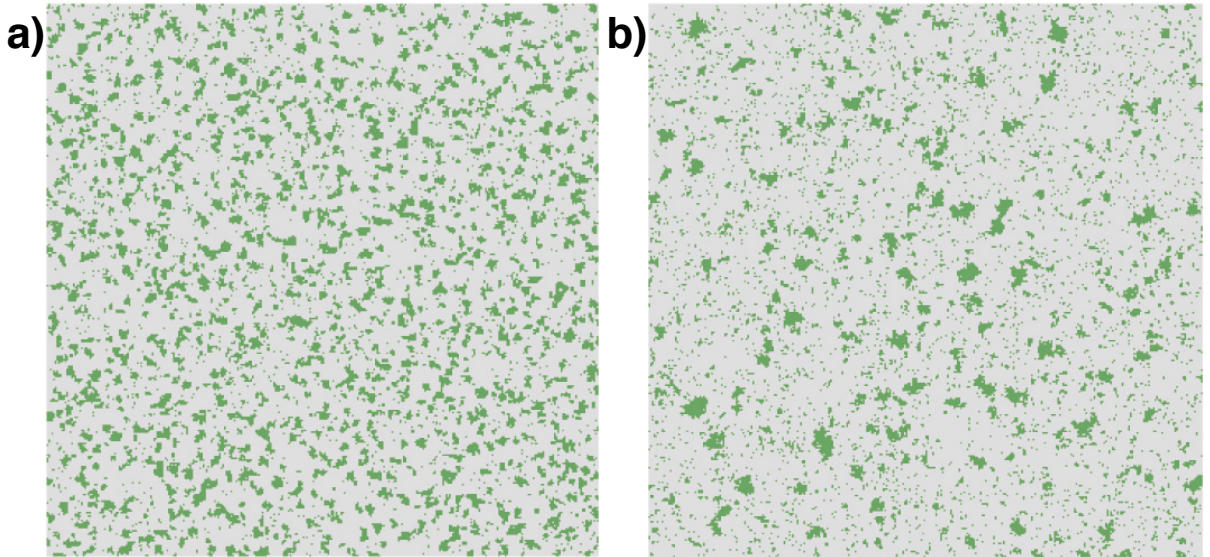


Figure 3.5: Clustering of $\Delta EGFR$ cells, as computed from the discrete model. Snapshots of the system are taken at time $T = 1800$, which corresponds to the fifth day of experiments (see Fig. 3.2b). An upper panel corresponds to the case $\alpha_{high} = \alpha_{low}$, a lower panel incorporates an assumption that invasive cells switch their phenotype to proliferative (and increase their proliferation rate), when they form clusters, here $\alpha_{high} \gg \alpha_{low}$. Parameters: $q = 0.9, \alpha_{low} = \alpha_{high} = 0.00127$ for the upper panel and $q = 0.84, \alpha_{low} = 0.0004, \alpha_{high} = 0.0056$ for the lower panel, the diffusion time is $\tau = 4$ minutes.

the experimental results both in case of "constant" proliferation ($\alpha_{high} = \alpha_{low}$) and in case where we distinguish between proliferative and invasive cells ($\alpha_{high} \gg \alpha_{low}$).

For "constant" proliferation the agreement is rather poor (for any set of the unknown parameters (q, α)). The number of small clusters in the simulations (Fig. 3.6, pluses) is larger than in the experiment (Fig. 3.6, circles, dotted line), while the number of large clusters is much smaller than in experiments. The same conclusion follows from the analysis of the corresponding snapshot of the system, Fig. 3.5. The disagreement can be resolved by recalling that the proliferation rate is higher in the proliferative zone than in the invasive zone [69], $\alpha_{high} \gg \alpha_{low}$. Figure 3.6 shows that the resulting cluster size distribution (Fig. 3.6, squares) is in a good agreement with the experiment on day 5. This is also true on day 4; it is quite difficult to make a comparison for earlier times, since the clusters are small. Therefore, our modeling suggests two successive mechanisms, leading to formation and growth of cell clusters. First, cells form small clusters due to the effects of cell-cell adhesion. Second, cells in these clusters switch their phenotype to proliferative and start dividing more rapidly.

As Fig. 3.2a shows, wild-type cells do not form clusters. Nevertheless, it is possible to get some information about them by analyzing the total intensity of the green fluorescence in the image. This allows us to estimate the total cell density at early times, when the density growth is almost exponential. Therefore, we can derive the low-density proliferation rate, which turns out to be $\alpha_{low} = 0.0017$. There are still two unknown parameters left for the wild type cells: the effective strength of cell-cell adhesion, q and the division rate of proliferative cells, α_{high} . The inset in Fig. 3.6 shows the phase diagram of parameters as computed from simulations of the discrete model. Each point in this phase diagram corresponds to the set of parameters (q, α_{high}) for the fixed α_{low} . Above the dotted curve, the system

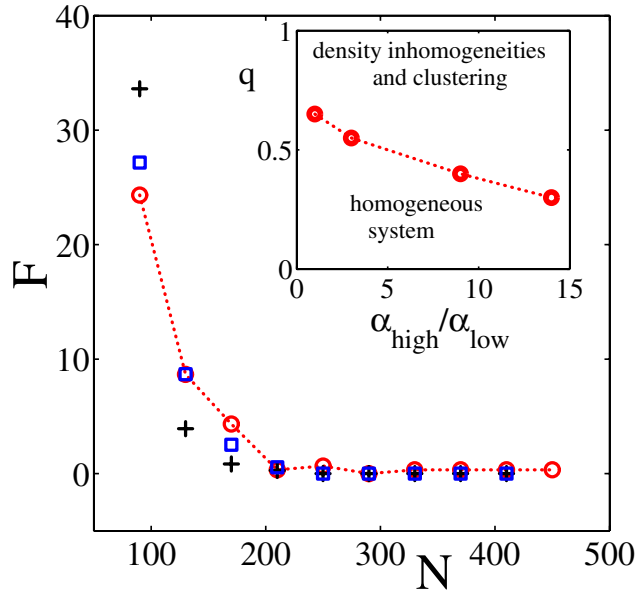


Figure 3.6: Cluster size distribution for Δ EGFR from experiment (circles, dotted line) and simulations (symbols). Pluses correspond to the case $\alpha_{high} = \alpha_{low}$, see also the upper panel in Fig. 3.5; squares correspond for the case we take into account the dynamic phenotypic switch between “invasive” phenotype and “proliferative” phenotype (see text) when cells form clusters, see also the lower panel in Fig. 3.5. Parameters are the same as in Fig. 3.5. An inset shows the phase diagram of parameters (q, α_{high}) as computed from simulations of the discrete model for $\alpha_{low} = 0.0017$ (see text). Above the dotted curve, the system shows density inhomogeneities, while below it the system remains homogeneous. Therefore, the possible parameters values for the wild type correspond to the lower part of the diagram.

shows density inhomogeneities, while below the threshold cells remain distributed uniformly. Therefore, the possible parameters values for the wild type correspond to the lower part of the diagram.

In our modeling, the adhesion parameter q determines the probability of detachment of a cell from a neighboring cell (or a cluster). How can this effective strength of cell-cell adhesion be experimentally measured? The value of q for different cell types can be estimated by measuring the shed rate of invasive cells from the tumor surface. Since shedding is related to the process of breaking the cell-cell bond, by using the known shed rate and the tumor surface area, we arrive at values of the adhesion parameter q . We performed another experiment, in which $U87\Delta EGFR$ tumor spheroid was placed in a collagen gel. Using confocal microscopy, we *counted directly* the number of cells detached from the spheroid surface per unit time per unit area. For the tumor with radius of $170\mu m$, we measured the shed rate of 0.0357×10^6 cells day $^{-1}$ cm $^{-2}$. The discrete model gives one-to-one correspondence between the shed rate J and the adhesion parameter q , see Fig. 3.7. This gives $q \approx 0.85$ for $\Delta EGFR$ cells, which is in an excellent agreement with the values of q used in our modeling. For the wild-type cells, we use estimates for the shed rate from [159], which give much smaller q .

3.3 Discussion

In this work, we have studied the formation of clusters in a system of motile cells both experimentally and by simulations of a discrete stochastic model. We showed that there are two radically different regimes of behavior: cells either form clusters or remain homogeneously distributed over the system. We propose the following mechanism for cluster formation and growth. Initially small clusters are formed due

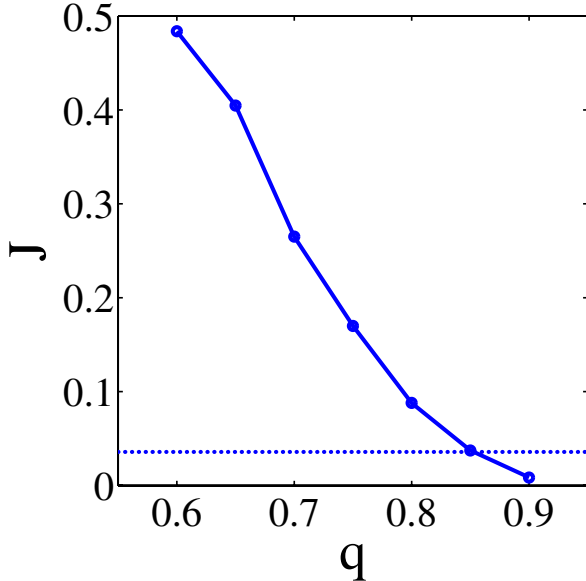


Figure 3.7: Shed rate J from tumor spheroid (measured in $10^6 \text{ cells cm}^{-2} \text{ day}^{-1}$) as a function of the adhesion parameter q as computed in numerical simulations of a three-dimensional version of the discrete stochastic model. The dotted line corresponds to the experimentally observed shed rate for $U87\Delta EGFR$ cells, which gives $q \simeq 0.85$.

to phase separation if cell-cell adhesion is larger than some threshold value. Then cells in these clusters switch their phenotype from “invasive” to “proliferative”, which causes a rapid growth of clusters. Our experimental results are completely consistent with our theoretical predictions. The experiment shows that the process of phase separation, familiar in materials science, occurs in cell cultures.

The application of these ideas to *in vivo* tumors is, necessarily, quite speculative, but not unrealistic. In fact, GBM and anaplastic astrocytomas are known to commonly form secondary foci of tumor formation within 2 cm of the initially resected tumor. This would suggest that they behave as $U87\Delta EGFR$ cells with $q > q_c$. However, another behavior seen in malignant gliomas is exemplified by the disease gliomatosis cerebri (GC). In GC, single malignant glioma cells infiltrate diffusely into the brain in a relatively homogeneous fashion. In this case, GC cells behave more

like U87WT; their behavior is consistent with $q < q_c$. We should point out that secondary tumor formation is the obstacle to successful treatment of GBM patients after resection of the primary tumor. Cell-cell adhesion is known to be important in tumor growth and morphogenesis [164]. We can guess that adhesion among the cloud of invasive cells (that are known to exist around GBM tumors) plays an important role in initial formation of clusters. We speculate that this may cause the dynamical switch of phenotype from “invasive” to “proliferative”, which leads to development of recurrent tumors. Our model suggests that Δ EGFR cells form clusters (if we return to the patterns in [159, 93] we can suggest that the small clusters of Δ EGFR cells are almost certainly due to enhanced adhesion in this cell type), which is consistent with the experimental observation that Δ EGFR mutation is associated with higher malignancy [121].

Altered cell-cell adhesion is likely to be an important factor in glioma cell migration. One of the major mechanisms of cell-cell adhesion is the interaction of members of the cadherin family expressed on adjacent cells. Cleavage of N-Cadherin has been shown to promote glioblastoma cell migration [99], and reorganization of the cadherins has been reported in glioma invasion [139]. Additional studies of biological cell-cell adhesion mechanisms in glioma will be necessary to understand the specific mechanisms pertinent to glioma cells.

Finally, we did not consider the effects of cell-matrix adhesion, however, it is no less important than cell-cell adhesion. Cell-substrate adhesion is known to affect cell migration [181]. Therefore, choosing a specific migration time corresponds to the specific cell-substrate adhesion. In experiments, increase in cell-substrate adhesion may either increase or decrease the motility of cells, depending on functional ligand and receptor density. It is widely believed that there is a competition between cell-cell

and and cell-substrate adhesions, and that larger cell-substrate adhesion suppresses clustering [146]. Suppose that the density of ligands and receptors is such that increase in cell-substrate adhesion causes a decrease in cell motility. For supercritical adhesion, our model suggests that the larger the cell-substrate adhesion, the more time it would take to form clusters. This does not contradict the experimental findings of [146], but suggests a long time may be needed to observe clustering.

CHAPTER IV

Network Reorganization in Adult Neurogenesis

In adult hippocampal neurogenesis, a continuous population of new cells integrates into the existing active neuronal network of the dentate gyrus. The process is thought to assist memory formation and storage by reinforcing precise activity patterns while leaving intact the large-scale structural and functional properties of the network [3, 153, 182]. This suggests that adult neurogenesis is optimized for the maintenance of functional activity during structural turnover. However, it is also known that epileptogenic injury causes structural changes to the network environment around new cells, dramatically altering existing connectivity patterns, and is associated with aberrant integration of new cells and possibly encourages the development of epilepsy [130]. In this Chapter, we use a computational model to consider the role of the established network topology on the outcomes of neurogenesis-driven reorganization. In particular, we ask if different networks have similar or different robustness of structure and functional activity to the addition of new cells.

Though many details are as yet unknown, considerable evidence suggests that new cells are promoted by firing activity throughout their development in many ways. Hippocampal neuroblasts arise from progenitor cells in the subgranular zone of the dentate gyrus (DG) and migrate a short distance into the granule layer [7, 90, 33, 102].

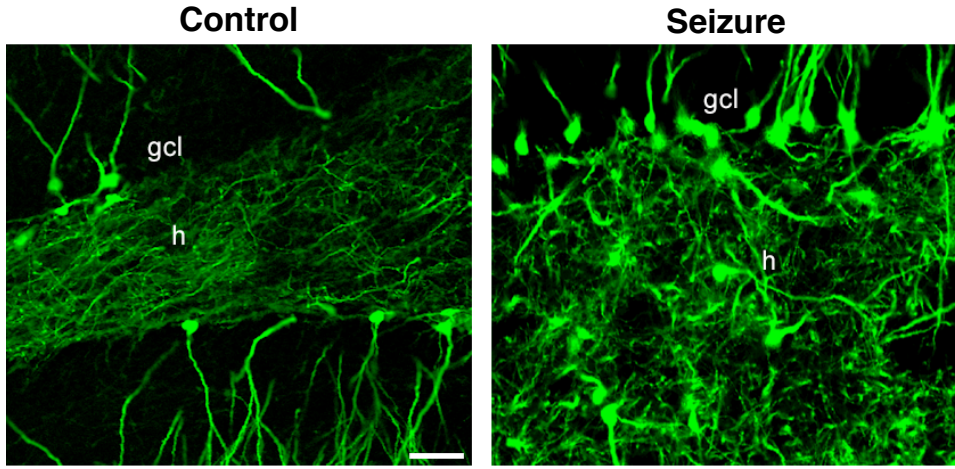


Figure 4.1: Incorporation patterns of adult-born neurons in the rat hippocampus in normal conditions (Top) and four weeks post-status epilepticus (Bottom). The granule cell layer is denoted “gcl” and the hilus is denoted “h.” Note both abnormal locations of survival and disrupted innervation patterns. See A.1 for methods. Images provided courtesy of Jack Parent.

Excitatory stimulus in the environment increases the rate of production of new cells [48]. Activity from synaptic inputs from GABAergic interneurons promotes the development of neural processes [127, 67]. Studies have found new granule cells to be preferentially activated by stimulation [142] and to have sensitive synaptic plasticity [148]. Survival of new cells is also increased by integrated activity [109]. Taken together, new cells appear to require activity to mature, but also arrange their connections to seek activity. Despite this activity-seeking, however, the activity remains globally unchanged.

Epileptogenic injury can significantly alter the neurogenic niche and induce changes in integration (e.g. Figure 4.1). The number of inhibitory cells is reduced by hilar cell death, the size and spread of granule cell synaptic outputs increases due to mossy fiber sprouting, and the spatial distribution of granule cells is widened because of granule cell dispersion [30]. Additionally, seizures form a different activity environ-

ment in which to mature. The rate of neurogenesis after status epilepticus has been observed to increase [136]. Some neuroblasts migrate ectopically into the hilus and, unlike in the healthy brain [136, 147, 135], appear to receive synapses from other granule cells [140].

We hypothesize that the divergent integration patterns arise from the possibility that neurogenic network maintenance has different outcomes in different network environments, independent of possible pharmacological effects of injury. To address this, we build a simple computational model of neurogenesis with the only fundamental assumption that new neurons wire and survive within the network based on their established activity. By varying properties of the original network, we look at the effect of the established network structure on its own reorganization. We find that there is an optimal network topology which is dynamically and structurally robust to the addition of new neurons. For other network structures or decreased inhibition levels, neurogenesis leads to significant structural and dynamical changes in the underlying network. We thus postulate that there is a range of normal conditions in which neurogenesis could enhance network performance, while in pathological conditions it can further *worsen* the pathology instead of being a stable maintenance process.

Considerable experimental [60, 34, 169] and computational work [4, 19, 39, 48, 177] has previously focused on the role of neurogenesis in learning. The role of network itself in neurogenesis has been virtually ignored, however. Computational modeling of the DG and some of the structural changes associated with epilepsy has done at the network level [58, 116], but not with feedback into the neurogenesis-based network reorganization. Existing theoretical work has focused on either the role of neurogenesis or the behavior of static injured networks, but has not considered both

aspects within a similar framework like we do here.

4.1 Neurogenesis model

4.1.1 Initial network formation

We build the connection structure of the initial network in our model in a manner inspired by Watts-Strogatz random networks [175]. A cartoon summarizing the result of this process is provided in Figure 4.2a.

For each cell we determine its downstream (axonal) connections by looking within a radius containing twice the desired average number of out-connections and connecting to each with probability $1/2$. For each connection, we rewire it to a randomly chosen excitatory cell anywhere in the network with a probability, p , which we vary. For $p = 0$, no connections are rewired, and for $p = 1$ all connections are sent to a random target. The network structure thus depends strongly on the parameter p , which effectively controls the ratio of short-range connections to long-range connections. Each excitatory neuron is also connected to, on average, four inhibitory neurons through the same procedure as described above, without random rewiring. All excitatory-to-inhibitory connections are therefore local. Inhibitory cells send out-connections to, on average, four other inhibitory cells and 100 excitatory cells. These targets are selected purely at random. We adopted this connectivity structure to roughly represent that of the CA3 layer of the hippocampus [84].

The rewiring parameter p allows the connectivity of excitatory-excitatory networks to range from purely local ($p = 0$) to purely random ($p = 1$), while preserving many other aspects of the network such as the degree (i.e. cell connectivity) distribution. Between the local and global extremes is a small-world topology. Small-world networks are characterized by having short average path lengths between any two

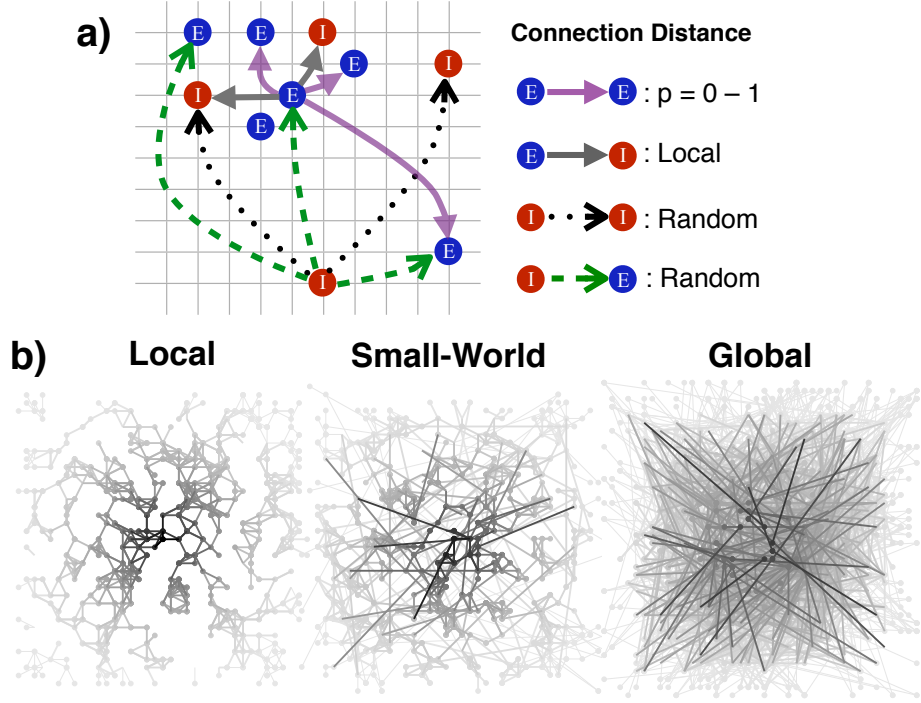


Figure 4.2: a) Cartoon schematic of the established network formation. Local excitatory-to-excitatory connections are rewired to a random excitatory cell with probability p . b) Examples of this process on reduced networks for each of the three regimes we consider in this work: Local ($p = 0$), small-world ($p = 0.1$), and global ($p = 1$). Each image is a subset of an excitatory network of 500 cells with an average out-degree of 3. Edges are colored darker according to how close their parent cell is to the center.

nodes, but a high probability that the neighbors of a given node are connected to one another [118]. We observe small-world structure in our excitatory networks around $p = 0.05\text{--}0.2$ (See A.2). Examples of the above scheme for local, global, and small-world networks are shown in Figure 4.2b.

For the simulations presented here, the established networks prior to neurogenesis have 1000 excitatory neurons and either 200 (normal inhibition) or 100 (low inhibition) inhibitory neurons at random on a two-dimensional square lattice with 40 lattice sites per side and periodic boundaries. A lattice site can hold at most one excitatory cell. Inhibitory cells are placed on a site independent of its occupancy

status to reflect distinct cell layers. We specify that each excitatory cell will be connected to, on average, 3.5% of the other excitatory cells.

4.1.2 Neuronal dynamics

We represent network activity with integrate-and-fire dynamics with stochastic spontaneous firing. While integrate-and-fire is only a very rough approximation of the dynamics of real neurons, it is sufficient for the purposes of our model, for which firing rate, not detailed dynamics, is paramount.

In the integrate-and-fire scheme, the k th cell has a voltage V_k which follows:

$$\frac{dV_k}{dt} = (I_{e/i} + E_k - \alpha_k V_k) + \sum_j w_{jk} A_{jk} I_{syn}^j(t + \tau_{delay}),$$

where $I_{e/i}$ is the global excitability of excitatory/inhibitory neurons, depending on what class of neuron k belongs to. The initial potentials are distributed uniformly at random between 0 and 1. The cellular and network parameters are adopted from [84]. We use $I_i = 0.6$ and $I_e = 0.73$. The external stimulus is denoted by E_k , which is 0 for unstimulated cells and 0.4 for those which receive external stimulus. Stimulus occurs at the five centermost excitatory cells. The membrane leak constant is α_k , drawn for each cell from a uniform distribution between 1 and 1.3. The network adjacency matrix elements are denoted by A_{jk} , which is 1 if neuron k sends an output to neuron j and 0 otherwise. Synaptic weight is denoted by w_{jk} . Synaptic weight is based only on the class of the neurons involved, with $w_{ee} = 0.2$, $w_{ei} = 0.4$, $w_{ie} = -0.4$, and $w_{ii} = -0.7$. When a neuron's membrane potential becomes higher than one, it fires. The synaptic current follows a double exponential form taken from [117]. For more details, see A.3.

4.1.3 Neurogenesis and network reorganization

In order to represent neurogenesis, we slowly introduce new neurons after the network has settled into steady state dynamics. A new cell is placed on a randomly chosen unoccupied lattice site. To determine its input connections, a new cell looks at the input connections to nearby cells. The most highly active inputs to nearby cells are chosen, with some noise to wash out small differences in firing activity, until the cell has the desired number of inputs. Our results are not sensitive to modest changes the amount of noise. Similarly, the output connections are drawn from downstream targets of nearby cells. Connections are made to a random subset of possible outputs until the new cell has the same average number of connections as the original network.

During the initial stages of its dynamics, an introduced cell can undergo rapid rewiring. At several points while the new neuron is immature, all output connections which do not result in a sufficient number of coincident downstream firing events are broken and new connections are again chosen at random. When a cell has reaches its maturation age, it survives and ceases rewiring only if it has fired at a much higher rate than background, otherwise it is removed. When a new cell survives, the total population is kept constant by killing a randomly chosen mature cell. Birth and maturation rates are chosen so that there is little interaction between two immature cells and the network activity is well sampled by each new cell. The precise implementation of these rules and parameter robustness is in A.5.

Except where noted, simulations are performed by first running dynamics on the stimulated initial network for establish baseline activity. We then add 500 new cells as described above, and stop the simulation after the last new cell has had an opportunity to mature. Each data point represents 50 realizations. All simulations

and data analysis were performed in Matlab 7.7.0 (Mathworks). See A.4 for exact descriptions of the analysis techniques used.

4.2 Results

We investigate neuronal integration and activity patterns as a function of structural properties of the existing initial network for two levels of inhibition. We find that these integration patterns critically depend on the existing network topology, and under normal inhibition fall into one of three categories: Local networks for very low p , small-world networks for $p \approx 0.1\text{--}0.3$, and global networks for, roughly, $p > 0.3$. A typical example of each is shown in Figure 4.3, which provide a template for understanding the details of the results that follow.

For local networks, the spatial distribution of new cells that survive is constrained, but often large. This follows a similar distribution as activity, where cells in the center participate in bursts that propagate radially outward. Because a cell's location and its firing time are tightly related, cells exhibit some synchrony with much of the active region, but this does not necessarily span the further extents. Since axonal connections are selected by their ability to induce downstream firing events, the output structure tends to point into the active region, but not necessarily with a particular focus.

Networks with a high rewiring probability show no localization of survivorship at all, even though a significant fraction ($1-p$) of the edges are still local in nature. New cells spread evenly throughout space, resulting in bursts that spread without spatiotemporal order, but with very high synchrony everywhere in space. High synchrony and uniform activity create a distribution of downstream connections that are spread throughout space and highly unfocused.

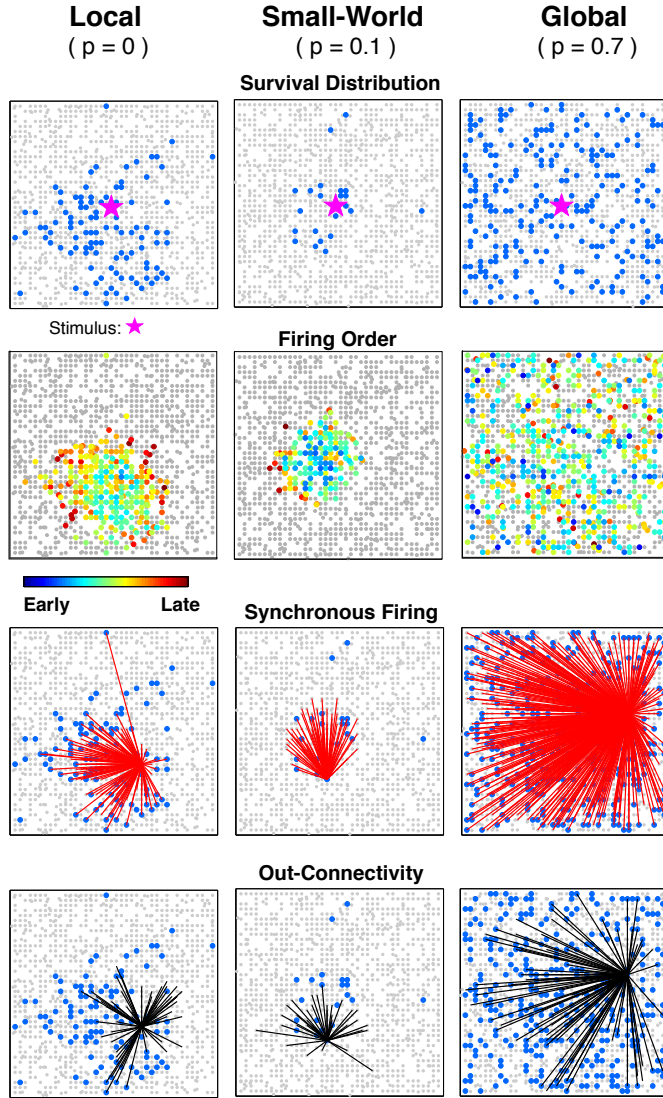


Figure 4.3: Examples of typical survival patterns of new cells for each of the normal inhibition three regimes: local ($p = 0$), small-world ($p = 0.1$), and global ($p = 0.7$). The top row depicts new cells (blue) amidst established cells (gray) and the stimulation point (magenta star). Incorporation is much more concentrated in the small-world case than either local or global. The second row highlights the out-connections (black lines) from one new cell. Local topologies, while localized, have less radial orientation of out-connections than small-world topologies. Global networks are highly random. The third row shows connections from the same cell to cells, new or established, with which its mean phase coherence was greater than 0.5 (red lines). Local and small-world networks are spatially constrained, but the small-world does not expand as far as local networks. Global networks, by contrast, show widespread synchronization. The fourth row depicts the mean firing delay from burst onset (early to late represented by blue to red). Global networks lack spatial firing order.

Small-world networks seem intuitively that they should appear like slightly more global versions of local networks, but this does not occur. Previous investigations have shown that the small fraction of long-range connections present in small-world networks can limit the scope of activity by interfering with the ability for activity to propagate in waves [145, 117]. Survivorship for small-world networks is localized, and tends to be more focused about the stimulus region. This bursts still tend to propagate in a basically radial fashion, but do not extend as far. This causes the region with highly synchronous firing to include the extent of the active region, since it does not take much time for signals to traverse it. As a result, the axonal connections that can induce firing events are highly oriented toward the active region. Altogether, these integration patterns make the small-world networks respond to stimulus in a more orderly and focused fashion than either the purely local or more global cases.

4.2.1 Activity and augmentation patterns of the network in response to external stimulus

We first consider in detail how the network activity patterns respond to external stimulus for different network topologies. We stimulated five excitatory neurons positioned in the center of the network by applying an additional constant current. As expected from the example cases, for established networks with $p < 0.2$ and normal inhibition, we see highly localized activation patterns (Figure 4.4a. Note log color scale), while global connectivity patterns and/or diminished inhibition produce widespread firing. Considering only the changes in firing rate (Figure 4.4b), new cells create an increase in the firing rate that remains near the stimulated region for normal inhibition and low p . This confirms that our neurogenesis process can sharpen the response of our network to a stimulus. Increasing the rewiring and

decreasing inhibition each result in a global increase of firing rate, with amounts varying depending on the details of the network.

The difference in activity distribution between local and small-world integration is subtle, but very important. In those local networks which admit an above-median number of new cells, the activity profile propagates radially outward (Figure 4.4c). While local networks with below-median numbers tend to show stable activity, cases of expanding activity are sufficiently common overall in local networks to reduce the ability of reorganization to generally remain focused. This is in sharp contrast to the small-world case, where even those instances which admit the most cells show much more stable and focused profiles over time. Global networks have extremely different dynamics, increasing with time uniformly throughout space.

The focused activity for small-world networks are reflected in the spatial distribution of survivorship. Small-world networks show surviving new cells to be closest to the stimulus in the small-world case (Figure 4.5a). To maintain specific activity after incorporation of new cells, as we expect in normal hippocampal conditions, the established network must have relatively local connectivity of the original network and sufficiently high levels of inhibition. Small-world networks exhibit the highest correlation between initial activity and the spatial distribution of surviving cells, slightly better than purely local networks and much better than more global networks (Figure 4.5b). As might be expected since new cells enhance network activity, such small-world networks also show the highest spatial correlation between initial frequency and the chance in frequency (Figure 4.5c).

While we observe that under normal inhibition, the smallest number of added cells survives when the network is in the small-world regime, under low inhibition the situation changes dramatically. The spread of new cells is not hindered in any

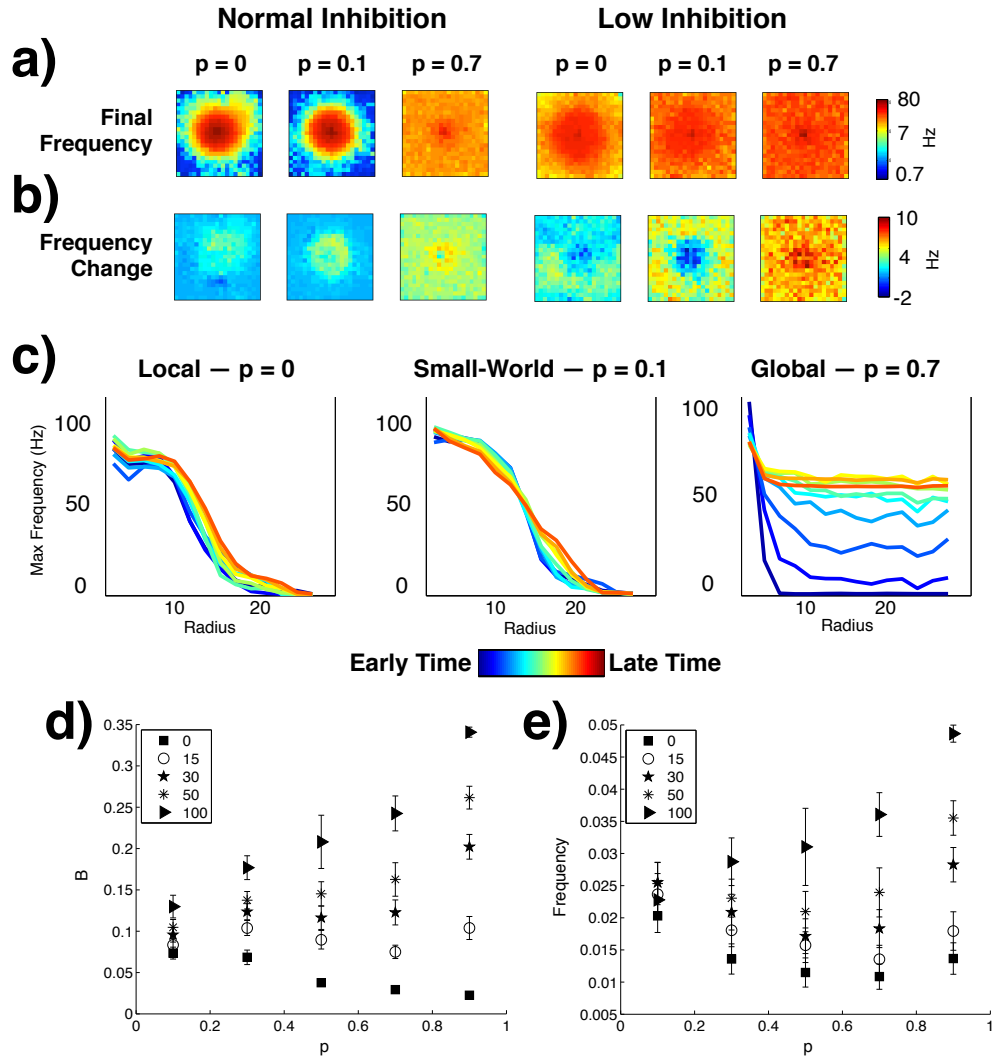


Figure 4.4: Descriptions of the distribution of activity. a) Average spatial distribution of final firing rate (top, log scale) and b) change of firing rate (bottom, linear scale) for several values of rewiring probability and inhibition. Only normal inhibition and local and small-world networks have spatially constrained final activity and activity change, with small-world having more focused increase of firing rate around the stimulated region. c) Activity profile as a function of distance from the stimulus at ten points during the simulation, averaged over the “worst-case” half of simulations with the highest rate of survival. Dark blue is the earliest, dark red the latest. Note the expanding profile in the local case. d) Mean network frequency as a function of the number of cells survived (different markers) and incorporated into the network for normal inhibition. d) Burst synchrony B , ranging from 0 for Poisson random firing to 1 for exactly simultaneous, as a function of number of cells survived. Notably, global networks are not functionally robust to the addition of activity-seeking cells. Where present, error bars denote standard error.

case, allowing the network activity to be uniformly very high after cells integrate (Figure 4.4a). Interestingly, with low inhibition, the once-optimal small-world regime is associated with the *widest* distribution of new cells and the worst correlation of network response with initial activity (Figure 4.5a–c).

4.2.2 Innervation patterns of incorporated neurons

Another important feature of neurogenesis is the innervation pattern of the new cells. We consider each synaptic connection to be spanned by a long axon and short dendrites, such that the direction of a connection is roughly that of the innervating axon. For low values of p , a clear pattern of radially oriented outputs toward the stimulation site is observed for introduced cells, as in the examples in Figure 4.3. This disappears for large p . (See A.7 for more details of the orientation and innervation patterns.)

To quantify this, we measured the average radial component for the output directions of all surviving new cells (Figure 4.5d). Networks in the small-world regime show higher radial ordering than those with either more purely local or global connection structure. This illustrates yet another way in which activity in the established network is best able to specifically dictate the behavior of new cells in small-world networks. Additionally, low inhibition networks are not able to develop the same degree of directionality as normal networks.

4.2.3 Firing dynamics

Inspired by the spatio-temporal ordering (or lack thereof) of firing events in Figure 4.3, we consider differences in the firing patterns of new and established cells in reorganized networks. If we look at time traces of the instantaneous firing rate, we see that for small-world networks the activation of new neurons overlaps with

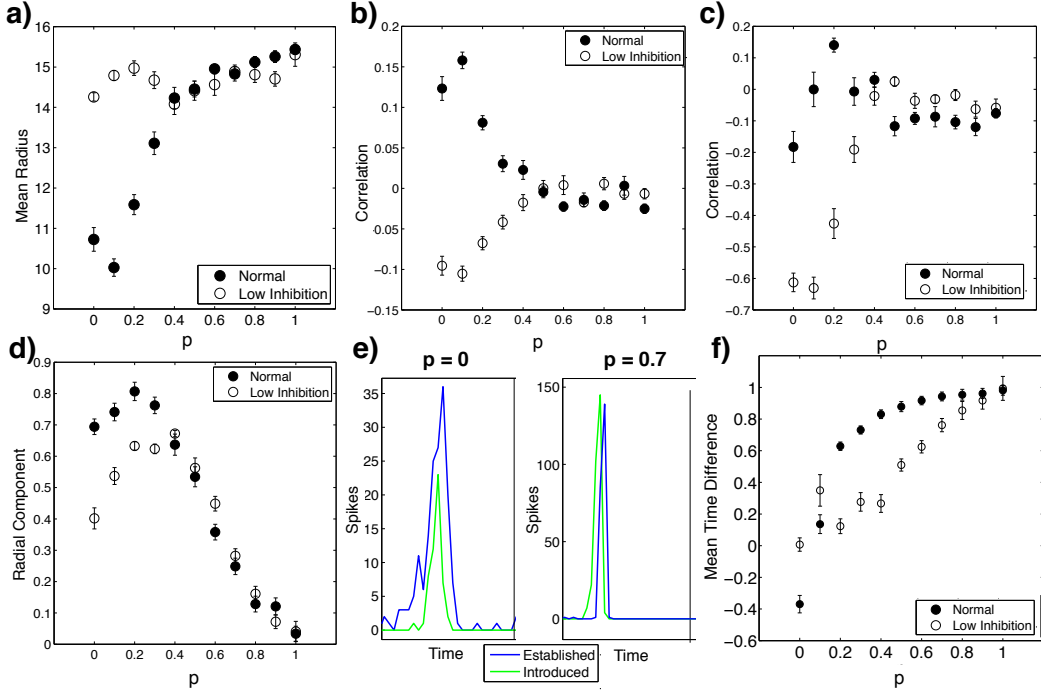


Figure 4.5: a) Mean distance of surviving cells from stimulus point. b) Spatial correlation of initial network activity and survival probability. Note that the optimum occurs for $p = 0.1$, with neither local nor global networks performing as well. c) Correlation of initial activity with change in activity. Again, small-world networks are the only ones to show consistent enhancement of initially active regions. d) Mean radial (relative to stimulus location) orientation of new cell out-connections. Small-world networks show the most radial order. e) Examples of the intraburst structure of instantaneous firing rate for local and global networks. In the local case, new cells fire as part of the burst, whereas in the global case new cells form a population that fires before the established network cells burst. f) The mean delay in intraburst firing onset of old cells compared to new cells. Local and small-world networks at normal inhibition do not see a large separation of new and old populations. Error bars in all cases denote standard error.

that of the already existing cells (Figure 4.5e) without a significant lead-lag pattern emerging between the two populations. For random networks, bursts from new cells tend to lead those of the original ones.

To quantify this observation, we measure the time difference between the onset of bursts of the old and new subpopulations (Figure 4.5f). This time difference is negative when old cells lead and positive when new cells lead. We restrict ourselves to data taken from the end of the simulation. We see that, in most cases, new cells will lead bursts in the established network. The only case where the established network consistently leads bursts is for low rewiring and normal inhibition. The transition between which cell population leads occurs when the network is in the small-world regime.

Notably, for low inhibition there is never a regime with a negative time difference. However, the new cell lead time is generally smaller for low inhibition because the established network requires less activity to be driven.

4.2.4 Robustness of network activity

Finally, we wanted to investigate if the observed changes in network dynamics was merely due to different numbers of new cells surviving in the different networks. To address this, we ran simulations that terminated when 100 new cells matured and were successfully incorporated into the network, instead of 500 being introduced to the network, but with many dying. Because of this, some simulations were run for longer time period than others. We quantified the activity patterns with the mean frequency of the network and a measure of synchronous bursting, denoted B , taken from [165].

Local networks are much more robust in terms of mean firing rate and mean

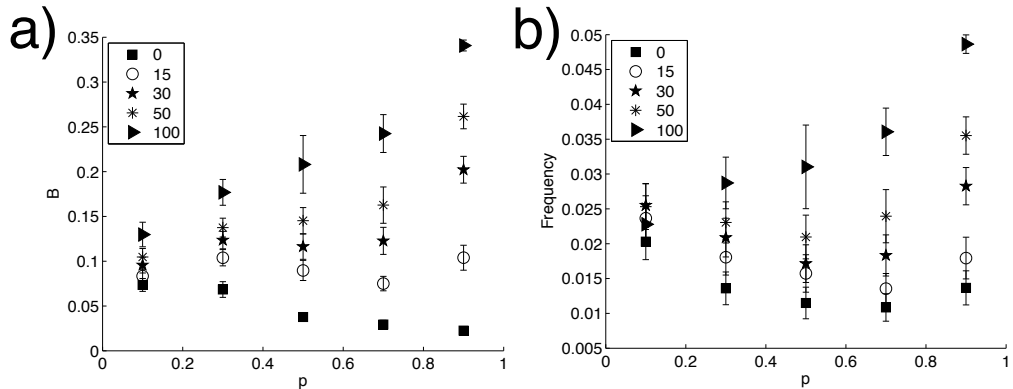


Figure 4.6: Mean network frequency (a) and burst synchrony B (b) as a function of the number of cells survived and incorporated into the network for normal inhibition. Notably, global networks are not functionally robust to the addition of activity-seeking cells.

burst synchrony to activity-dependent reorganization than those with more random connections (Figure 4.4d and e). In all cases, established networks with low p tolerate the incorporation of activity-seeking neurons with only modest increases in activity and synchronous firing. Networks with more global connections start with slightly less activity, but are not able to accommodate the same number of neurons without having increasing firing rate and spontaneous bursting. Decreasing inhibition does not qualitatively change this behavior, although the mean firing rate is generally higher (not shown).

4.3 Discussion

In this work, we considered how a network's topology affects its ability to be structurally and functionally maintained by continual addition of new network nodes during neurogenesis. To that end, we constructed a model with very general rules of activity-promoted incorporation of new neurons, and investigated outcomes as a function of the established network environment.

We found that with normal inhibition levels, our networks to have stable and focused reorganization by neurogenesis for a relatively narrow range of rewiring probabilities near $p = 0.1$, corresponding to the small-world regime of the excitatory network. For networks with that topology, the network activity most precisely dictates the survival location and structural integration of the new cells and the resulting change in firing rate, yet the network is still able to retain overall dynamical properties. This coincides very well with results of others that indicate that many parts of the brain are wired as small-world networks, as well as quantitative estimates of the DG connectivity that imply that it may be a small-world network [58]. However, when the network starts in a non-optimal topology or is provided with insufficient inhibition, the integration patterns are significantly different. Networks that are too local can allow new cells to propagate activity (and thus future new cells) away from the stimulus. Networks that are too global or have low inhibition see a uniform rise in activity throughout space and widespread, nonspecific integration of new cells.

Experimentally observed neurogenic outcomes differ greatly. A variety of experiments show that cells born in an epileptic environment integrate into the network in a more disorganized and less specific fashion than in healthy conditions. Widening of the granule cell layer and ectopic integration of neuroblasts into the dentate hilus are examples of wide dispersal in epilepsy [131]. While cells migrate abnormally due to changes in motility cues [72], how they alter the network dynamics is still an open question. The orientation of these new cells is highly random, in considerable contrast to the ordered picture seen in healthy granule cells. Additionally, neurogenesis accelerates after seizures in terms of both increased proliferation [22, 136] and faster functional integration [125]. Experimental observations have also found that experimental epilepsy reduces learning ability [158, 79, 85].

We have modeled a portion of the structural network changes observed in human and experimental temporal lobe epilepsy by implementing reduced numbers of inhibitory cells and changes in the network topology. In our model, networks which deviate from the small-world and normal inhibition regime, undergo significant structural and dynamical modifications during augmentation and tend to develop towards higher activity levels, global synchrony and a disordered response to the stimulus. Increasing rewiring induces much greater shifts away from stimulus specificity, with the additional characteristics of activity spreading widely through the network and activity-survival correlation becoming zero. The result is similar to the randomly oriented post-seizure neurons shown in Figure 4.1. Decreasing inhibition also causes even low values of rewiring to result in widespread activity and survival probability, as well as the increased survival rates observed experimentally.

Experiments on rats found that suppressing neurogenesis after status epilepticus reduced the duration and frequency of occurrence of recurrent seizures [87, 88], consistent with the picture that neurogenesis can reinforce and spread epileptic dynamics. In both cases the probability of developing seizures after SE was also reduced. Taken together, it suggests that some injuries that did not induce seizures created an environment that was pushed toward pathological dynamics by neurogenesis. In our model, pushing the network out of the small-world regime, either by making it more local or more global, results in a network less stable to reorganization by neurogenesis, while decreasing inhibition can immediately change dynamics.

Our results suggest that under pathological (epileptic) conditions the newly incorporated cells can exhibit shifts in their activity patterns compared to neurons in the established network. We did not observe these differences under normal conditions. This is possibly related to the observation that hubs (nodes with many more connec-

tions than average) can induce epileptic dynamics [116]. The activity-seeking nature of new cells is a mechanism that can create these hub cells. The relative dynamics of newly added neurons into pathological and normal networks would be an interesting avenue for experimental study to gain insight into the possible epileptogenic nature of neurogenesis.

We choose generic cellular incorporation rules that achieve biologically observed outcomes so that results will not depend strongly on the detailed biology. This is especially important for neurogenesis, as many details of environmental-development interactions are not well understood. Even our simple framework recapitulates many of the important general features of models with considerable biological detail. In healthy conditions, new cells incorporate in functional units that fire given specific stimulus, as in the detailed learning model of [4]. By looking at the frequency of our networks with no new cells in Figure 4.4d, we see a trend toward somewhat higher base activity for more local networks, made much higher by also decreasing inhibition. Similar behavior was reported in the extremely detailed and biologically driven hippocampal model of [58].

Our primary result is a general one, describing neurogenesis as a network maintenance process in which functional activity feeds back into structural modification. A neurogenic process that is sufficiently activity-dependent to enhance stable functional clusters can have a complementary topology under which its effect is optimal. When the same process operates on networks deviating from this optimum, the network is driven towards even more pathological behavior. This happens by activity becoming non-localized in the high rewiring case or in the local case by new cells forming an activity profile that continually moves farther from the stimulus. Critically, the differences in outcome can be entirely due to differences in the initial neurogenic

environment, without any changes in the underlying biochemistry of the neurogenic process.

CHAPTER V

Summary and Conclusions

The last two decades, roughly speaking, have seen a large shift towards viewing processes in physics, biology, and the social sciences within the context of their environment. Disease ecology and epidemiology have looked towards networks of people to help understand spread of important diseases like flu and SARS. Molecular biology has taken to considering large maps of how genes and proteins regulate one another within cells. Social science has begun to think about how social heterogeneity affects how opinions, behaviors, and even happiness can spread through populations. Physics has developed a wide number of important techniques for understanding the universal properties of networks, irrespective of origin, and the behavior of various types of processes on them. Complex networks are a large part of this zeitgeist, but certainly not the only part. Cancer biology, for example, has begun to look deeply into how tumors adjust their local cellular niche to recruit assistance from healthy cells. Even the extremely conservative field of economics has begun considering behavioral effects, realizing that individuals do not act with pure internal logic.

This approach has struck such a chord because differences in environments can cause even simple processes to have qualitatively different outcomes. The work presented in this thesis contributes in several small ways to understanding how this

occurs. As a physicist, I hope that even if the individual topics are disparate, this general approach is coherent.

In Chapter II, we analyze a family of voter-like models in a variety of complex network environments. As a simple non-equilibrium stochastic process, this is a useful testbed for ideas about how network structure affects the dynamics of coarsening systems where population consensus is an inevitable final state. In one case, we introduce a simple model based on the notion of contrasting urges toward conformity with others and internal consistency. If either consistency or conformity is reached faster than the wait for the complementary interaction to occur, the time to consensus is much slower than if conformity and consistency have similar weighting.

In the second part of Chapter II, we define a non-linear generalization of the voter model that allows us to carefully control the effect of the influence of degree. On power law networks, the system has a striking property: For relatively modest bias towards high-degree nodes, a frustrated state can persist around nodes with high degree relative to their local neighborhood, even if not high relative to the network as a whole. This is similar to the first part in that a long-lasting regime is induced by a separation of time scales, but here the long time scale arises naturally out of the synergy between large fluctuations in degree and bias in the voter-like process. Especially notable is that this frustrated regime arises when the dynamics shift from being largely independent of specific topology to being dominated by local features. Understanding this transition is an interesting direction for future work.

Chapter III contributes to the extensive literature on glioblastoma motility and pattern formation. We make a phenomenological connection between the variable magnitude of cell-cell adhesion and qualitative observations about the clustering of diffuse cells. We connect that to novel measurements of experimental systems in

order to show qualitative correspondence. This type of work is especially important in glioma assays, where it is known that cells interact with their environment in numerous ways, from differing cell-matrix and cell-cell adhesion to mechanical remodeling of the local matrix. The details of such interactions are extremely complex. Comparing effective models such as the one presented here to experimental results can be useful in helping elucidate the relative importance of each interaction and its connections to pathology.

We return to the impact of networks on processes in Chapter IV, where we consider adult neurogenesis in the dentate gyrus. New neurons continually join an established neuronal network in the brain and wire into it in a manner dependent on the local firing activity. Specifically, we investigated how the established network topology determines the structural and functional outcome after considerable turnover of cells. While the model has a number of implementation details, the fundamental organization is based on only two core principles: new cells can sense the network structure, and firing activity drives the integration and survival of new neurons. Our established network structure is based on Watts-Strogatz random networks to allow ease of control from local to small-world to global topologies,

We find three different trajectories for the network evolution. In extremely local cases, the new cells propagate activity as a front away from stimulus, spreading the activated region beyond its initial scope. Global networks are considerably more unstable with respect to new neurons, with globally synchronized activity quickly emerging after only a few cells join the network. In contrast to both of those, small-world networks retain stable functional activity and structure. Intriguingly, some experiments have suggested that the dentate gyrus is, in fact, in a small-world regime. Moreover, epilepsy is associated with significant changes to connectivity

of the dentate gyrus consistent with moving the network away from a small-world regime. It is associated with aberrant, less organized patterns of neurogenesis, much like we observe. This approach suggests that disturbances at the level of network structure can be sufficient to move neurogenesis from being useful for learning to driving the network toward epileptic dynamics.

From a general perspective, adult neurogenesis is an interesting case to study stochastic processes on dynamic networks. It has the dual properties of having well-studied microscopic dynamics and in being apparently optimized for the enhancement and preservation of network dynamics during node turnover. Our work forms a part of the study of network properties that are conducive to dynamic maintenance. One can imagine other situations with a similar goal that could branch off from our results, such as dynamically self-healing functional networks or optimizing institutional organization to retain skill sets. Optimizing environments for maintenance processes in general would be an interesting avenue for future research.

APPENDIX

Supplemental Material for Chapter IV

A.1 Experimental Seizure Model and Imaging Methods

A.1.1 Pilocarpine-induced status epilepticus

Adult male Sprague-Dawley rats were pretreated with atropine methylbromide (5 mg/kg intraperitoneally [IP]; Sigma), and 15-minutes later were given pilocarpine hydrochloride (340 mg/kg IP; Sigma) to induce status epilepticus (SE). Seizures were terminated with diazepam (10 mg/kg) after 90 minutes of SE as previously described [131]. Controls received the same treatments as experimental animals except that they were given saline in place of pilocarpine.

A.1.2 Retrovirus production and injection

Replication-incompetent recombinant RV vectors were pseudotyped by co-transfection of GP2-293 packaging cell line (Clontech,) with plasmids containing the RV vector (RV-CAG-GFP-WPRE, gift of S. Jessberger and F. Gage) and vesicular stomatitis virus (VSV)-G envelope protein (Clontech). The supernatant containing RV was harvested and filtered through a 0.45- μ m pore size filter (Gelman Sciences) and centrifuged in a Sorvall model RC 5C PLUS at 50,000xg at 4°C for 90 minutes. The RV-containing pellet was resuspended in 1X PBS, aliquoted, and subsequently stored

at -80°C until use. The concentrated RV titer was determined using NIH 3T3 cells and found to be approximately $1\text{-}5 \times 10^8$ CFU/mL. For intrahippocampal RV injections, animals were anesthetized with a ketamine/xylazine mixture and placed on a water-circulating heating blanket. After positioning in a Kopf stereotaxic frame, a midline scalp incision was made, the scalp reflected by hemostats to expose the skull, and bilateral burr holes drilled. RV vector ($2.5 \mu\text{L}$ of viral stock solution) was injected into the left and right dentate gyri over 20 minutes each using a $5 \mu\text{L}$ Hamilton Syringe, and the micropipette left in place for an additional 2 minutes. Coordinates for injections (in mm from Bregma and mm depth below the skull) were caudal 3.9; lateral 2.3, depth 4.2.

A.1.3 Tissue processing, immunohistochemistry, and microscopy

Four weeks after SE, animals were deeply anesthetized and perfused with 4% paraformaldehyde (PFA). The brains were removed, postfixed for 4-6 hours in 4% PFA, cryoprotected in 30% sucrose and frozen. Coronal sections ($40 \mu\text{m}$ thick) were cut with a freezing mictrotome and fluorescence immunohistochemistry was performed on free-floating sections [136, 134] using rabbit anti-GFP primary antibody (1:1000, Invitrogen) and Alexa 488-conjugated anti-rabbit IgG secondary antibody (1:400, Invitrogen). Images were captured using a Zeiss LSM 510 confocal microscope.

A.2 Established network structure

The established excitatory-excitatory network exhibits small-world structure around for values of $p \approx 0.05\text{--}0.2$. We plot the mean path length and the clustering coefficient in Figure A.1.

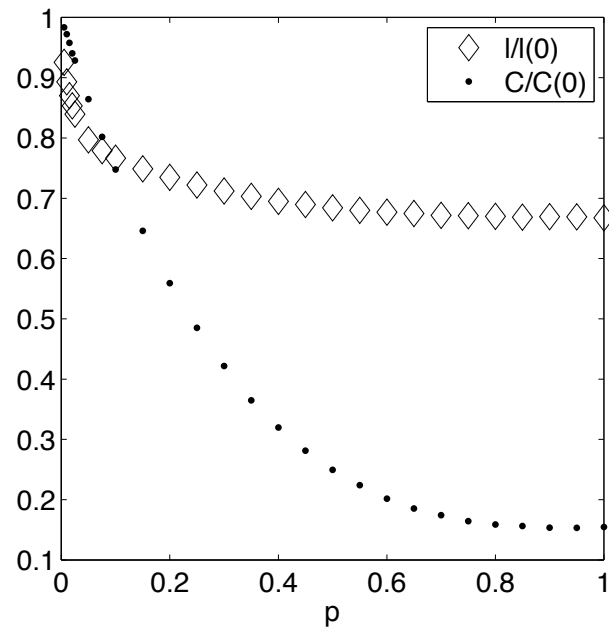


Figure A.1: Average mean path length (diamonds) and clustering coefficient (dots) as a function of rewiring probability p , normalized by the value for $p = 0$. All data points are averages over 20 simulated networks. The path length drops sharply as p increases, but the clustering coefficient has much slower decrease. The small-world regime is defined by having large clustering but small path length, which is found for rewiring probabilities near $p = 0.1$.

A.3 Model rules

A.3.1 Neuronal dynamics

We represent network activity with integrate-and-fire dynamics with stochastic spontaneous firing. While integrate-and-fire is only a very rough approximation of the dynamics of real neurons, it is sufficient for the purposes of our model, for which connectivity, not detailed dynamics, is paramount.

In the integrate-and-fire scheme, the i th cell has a voltage V_i which follows:

$$\frac{dV_k}{dt} = (I_{e/i} + E_k - \alpha_k V_k) + \sum_j w_{jk} A_{jk} I_{syn}^j(t + \tau_{delay}),$$

where $I_{e/i}$ is the global excitability of excitatory/inhibitory neurons, depending on what class of neuron k belongs to. The initial potentials are distributed uniformly at random between 0 and 1. The cellular and network parameters are adopted from [84]. We use $I_i = 0.6$ and $I_e = 0.73$. The external stimulus is denoted by E_k , which is 0 for unstimulated cells and 0.4 for those which receive external stimulus. Stimulus occurs at the five centermost excitatory cells. The membrane leak constant is α_k , drawn for each cell from a uniform distribution between 1 and 1.3. The network adjacency matrix elements are denoted by A_{jk} , which is 1 if neuron k sends an output to neuron j and 0 otherwise. The synaptic weight is denoted by w_{jk} . Synaptic weight is based only on the class of the neurons involved, with $w_{ee} = 0.2$, $w_{ei} = 0.4$, $w_{ie} = -0.4$, and $w_{ii} = -0.7$. The negative sign represents inhibition. Synaptic weight and excitability parameters are inspired by [84], where they were tuned to give controlled dynamics. Finally, the synaptic current from the j th neuron is $I_{syn}^j(t)$, where $I_{syn}(t)$ comes from a double exponential based on the time t since neuron j fired plus a signaling delay $\tau_{delay} = 0.08$:

$$I_{syn}(t) = e^{-t/\tau_s} - e^{-t/\tau_F}$$

where $\tau_S = 3\text{ms}$ and $\tau_F = 0.3\text{ms}$. This current form is taken from [117].

The voltage dynamics is numerically solved using the Euler method. Membrane potentials are capped below by 0 and if $V_j > 1$, the neuron j fires. All cells also have a probability of 0.0003 per ms of spontaneously firing, providing a mean background firing rate per cell of 0.3Hz. When a neuron fires, its potential is reset and held at 0 for a refractory time of 8 ms.

A.3.2 Neurogenesis and network reorganization

In order to represent neurogenesis, we introduce a new neuron every 350 ms after an initial 1,000 ms of simulation time. A new cell is placed on a randomly chosen unoccupied lattice site. We then proceed to form inward (dendritic) and outward (axonic) connections. We form inward connections by compiling a list of all inward connections of neighboring cells (within radius $R/2$) to the newly added one. This list denotes the possible in-connections. Inputs are drawn from this list by assigning a score g_i to each neuron on the list based on firing rate f_i and a small amount of random jitter ω drawn uniformly between 0 and 1:

$$g_i = a \frac{f_i}{\max_{\{i\}} f_i} + (1 - a)\omega.$$

The parameter a determines the amount of randomness in the selection process. We use $a = 0.8$ to wash out small differences in firing activity and preserve large ones. The neurons with the highest values of g are selected to be inputs to the new cell, until the appropriate number of inputs is reached. Our results are not sensitive to modest changes in a .

Similarly, the output connections are drawn from downstream targets of nearby cells. Connections are made to a random subset of possible outputs until the new cell has the same average number of connections as the original network.

During the initial stages of its dynamics the network can undergo rapid rewiring. At intervals of 200 ms of simulation time, all output connections which do not result in a sufficient number of coincident firing events (defined as a post-synaptic cell firing within 10 ms after the pre-synaptic cell fires) are broken and new connections are again chosen at random. After 2000 ms of simulation time, the new cell either dies if its firing rate is less than 100 times the spontaneous background firing rate (0.3Hz) or matures and ceases to undergo changes in its connections. When a new cell survives, the total population is kept constant by killing a randomly chosen mature cell.

Birth and maturation rates are chosen so that there is little interaction between two immature cells and the network activity is well sampled. Spatial activity distributions were not observed to change considerably for the parameters used here, except in response to new cells. Network activity can thus be well measured by 2000 ms of activity, even though it is not a physiologically relevant time period.

A.4 Metrics of network activity

A.4.1 Spatial measurements

To measure and visualize the firing activity, survivorship, and number of reconnection events as a function of location, we break the space into a 20×20 grid of squares covering the network space, so that each square represents four lattice sites. Activity and reconnection events are both measured as the average value among all cells that fall within a given square. For survivorship, we report the average number of cells that survive within a given square.

A.4.2 Radial component

To measure the mean radial component of output connections, we first create a vector for each new cell that represents the average direction of all outputs. This is defined as

$$\vec{v}_i = \frac{1}{k_i} \sum_j A_{ji} \frac{\vec{x}_j - \vec{x}_i}{|\vec{x}_j - \vec{x}_i|}$$

where $k_i = \sum_j A_{ji}$ is the number of out-connections from neuron i . We then measure the inward radial component by taking the dot product of this mean direction with the inward-pointing unit radial vector \hat{r} at the location of the i th neuron and normalizing by the magnitude of \vec{v}_i : $\hat{r} \cdot \vec{v}_i / |\vec{v}_i|$. This is averaged for all surviving new neurons in each simulation. Values close to one indicate highly radial directionality among new neurons' outputs. Values near zero are consistent with random directions.

A.4.3 Synchronous bursting

We use an existing measure of synchronicity of bursting based on interspike time differences [165]. We first make an ordered list of all spike times t_ν for all excitatory

Table A.1: Model parameters

Variable	Description	Value taken
N_{ex}	Number of excitatory neurons	1000
N_{in}	Number of inhibitory neurons	200, 100
N_{add}	Number of introduced neurons	500
L	Number of lattice sites per side	40
p	Rewiring probability	0–1
k_{ee}	Average number of excitatory-to-excitatory connections per cell	35
k_{ei}	Average number of excitatory-to-inhibitory connections per cell	4
k_{ie}	Average number of inhibitory to excitatory connections per cell	110
k_{ii}	Average number of inhibitory to inhibitory connections per cell	4
m	Radial multiplier	2
I_{ex}	Excitatory cell excitability	0.73
I_{in}	Inhibitory cell excitability	0.7
w_{ee}	Excitatory-excitatory connection weight	0.2
w_{ei}	Excitatory-inhibitory connection weight	0.4
w_{ie}	Excitatory-excitatory connection weight	-0.4
w_{ii}	Inhibitory-inhibitory connection weight	-0.7
α	Membrane leak constant	1-1.3
E	External stimulus	0.4
τ_s	Slow time for spike	3 ms
τ_f	Fast time scale for spike	0.3ms
τ_d	Spike delay	0.08 ms
	Random firing probability per ms	0.0003
	Refractory time	8 ms
	Integration time step	0.3 ms
	Number of stimulated cells	5
	Excitatory-excitatory connection radius	6.54 sites
	New cell “nearby” radius in units of the excitatory-excitatory connection radius	0.5
	Number of reconnection chances per cell per connection	10
	Time to mature	2000 ms
	Threshold firing rate for synapse survival	30 Hz
	Threshold firing rate for cell survival	30 Hz
a	New cell input jitter control parameter	0.8
	Time between introduced cells	350 ms
	Maximum time window between denoting firing events as causal	10 ms

cells. The measure B is defined as

$$B = \frac{1}{\sqrt{N}} \left(\frac{\sqrt{\langle \tau_\nu^2 \rangle - \langle \tau_\nu \rangle^2}}{\langle \tau_\nu \rangle} - 1 \right)$$

where $\tau_\nu = t_\nu - t_{\nu+1}$ is the time difference between subsequent firing events for on the excitatory network and angle brackets indicate averages over all such time differences. For large N and all neurons firing as independent Poisson processes, $B = 0$, and for synchronous bursting $B = 1$.

A.4.4 Spike order

The relative intraburst order of new and old cells is measured as the time difference between the onset of new cells bursting and old cells bursting. We define the onset of a burst as the time at which the number of new or old cells firing simultaneously increases past four. We make a list of the onset of all new and old bursts. For each burst of new cells, we record the time difference to the closest old burst onset. The convention is chosen such that an old burst that leads a new burst has a negative time difference.

A.5 Robustness

The simulations reported here have a gap time between introduced neurons of 350 ms, as opposed to 300 ms for the simulations in the main text. However, note that this change also does not cause significant differences.

A.5.1 Randomness parameter

The model presented has many parameters which are not constrained by data. Some of them, for instance the parameters for the integrate and fire dynamics, were chosen to give behaviors that give well-understood dynamics. Two parameters, how-

ever, control model rules that attempt to consolidate the result of complicated biological processes in an approximate fashion: the random jitter in connecting new cells to existing ones and the radius within which we look to find targets for new cell connections. We consider here the robustness of our results to changes in these parameters to perturbation.

Recall that when a new cell is placed on the existing network, it draws its connections from the inputs of nearby cells. Each connection i is given a rank g_i based on mean firing rate f_i , with random jitter ω drawn uniformly between 0 and 1:

$$g_i = a \frac{f_i}{\max_{\{i\}} f_i} + (1 - a)\omega$$

where the maximum is taken over all possible input cells. The parameter a thus controls the effect on of randomness on inputs.

The results in the text are for $a = 0.8$. We ran simulations for $a = 0.7$ and $a = 0.9$ and show the main results in Figure A.2 for normal inhibition and Figure A.3 for low inhibition. The behavior that we found previously is maintained for both values, showing that as long as firing activity dominates the ordering of innervating cells, the specific value of this randomness parameter results in almost no change in outcome.

A.5.2 “Nearby” radius parameter

When adding a new cell to the network, we make a list of inputs of nearby cells and connect to some of them as mentioned above. The maximum distance which we consider to be “nearby” is therefore a parameter in our model. If too many cells are within this radius, a new cell will be able to see inputs from a large part of the network and location becomes effectively meaningless. If there are too few cells considered, the selection process does a poor job of optimizing the network connections because there are only a small number of sources to consider.

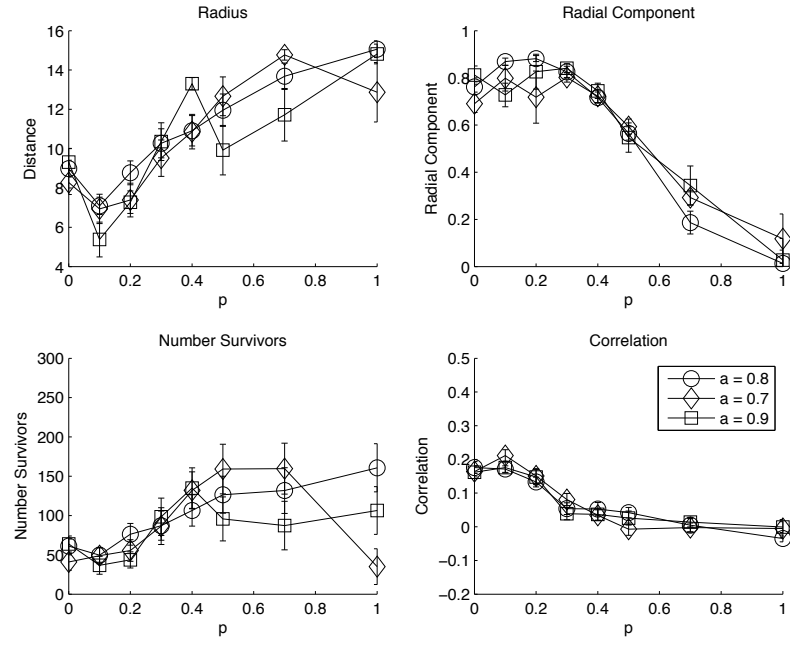


Figure A.2: Integration patterns of new neurons in normal inhibition networks, after perturbing the random jitter magnitude.

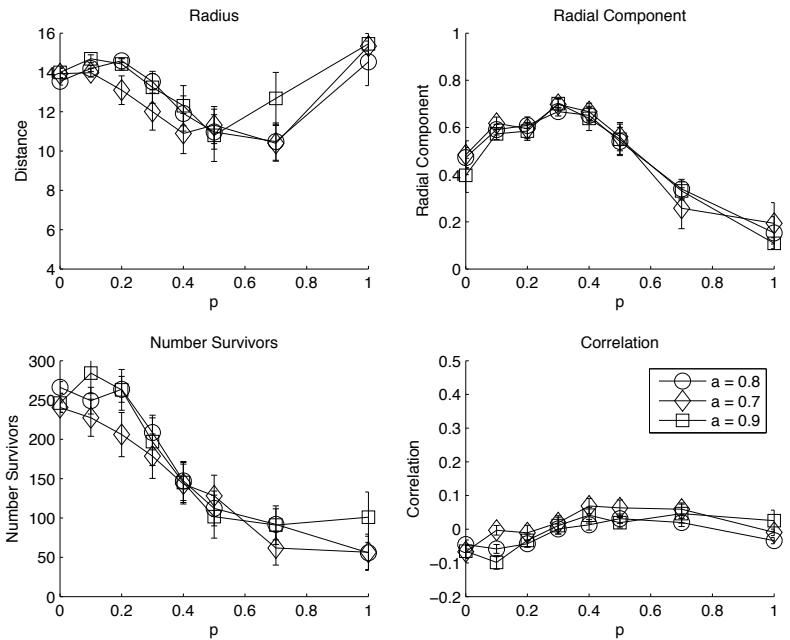


Figure A.3: Integration patterns of new neurons in low inhibition networks, after perturbing the random jitter magnitude.

These considerations led us to use a value in the text given by one half of the excitatory-excitatory connection radius. We consider small perturbations in this distance, testing 0.4 and 0.6 times the excitatory-excitatory radius. Results are shown in Figures A.4 and A.5, respectively. Area, and thus average number of nearby cells, goes as the square of distance so these values correspond to 0.64 and 1.44 times the number of cells than simulations shown in the main text.

The qualitative behaviors we described in the text are still seen here, although some plots have shifted somewhat. While a slight increase in radius causes no significant differences, when the target-selection radius is small, the rewiring probability at which new cells start to incorporate globally increases. The changes that result as a function of radius can be easily attributed to the fraction of the network that is seen by a new cell. With the radius smaller, the cell has access to fewer possible targets from which to receive innervation. This results in a less optimal number of inputs and therefore fewer survivors and a slightly higher correlation. Even so, the trends of increasing radius with higher rewiring, lower correlation, more random directionality with increased rewiring are still similar, though extrema occur for different values of p than with higher radius. Importantly for our results, the outcome of local networks with decreased inhibition differs only slightly in magnitude.

A.6 High connectivity

We briefly explored the effect of increasing the connectivity from 3.5% to 4.5%, since increased connectivity is another result of epileptogenic injury. For these simulations, we kept the number of inhibitory cells at 200, the same as the normal condition. We summarize the results in Figure A.6. For extremely local networks, the high connectivity situation is similar to the low inhibition regime. This makes sense,

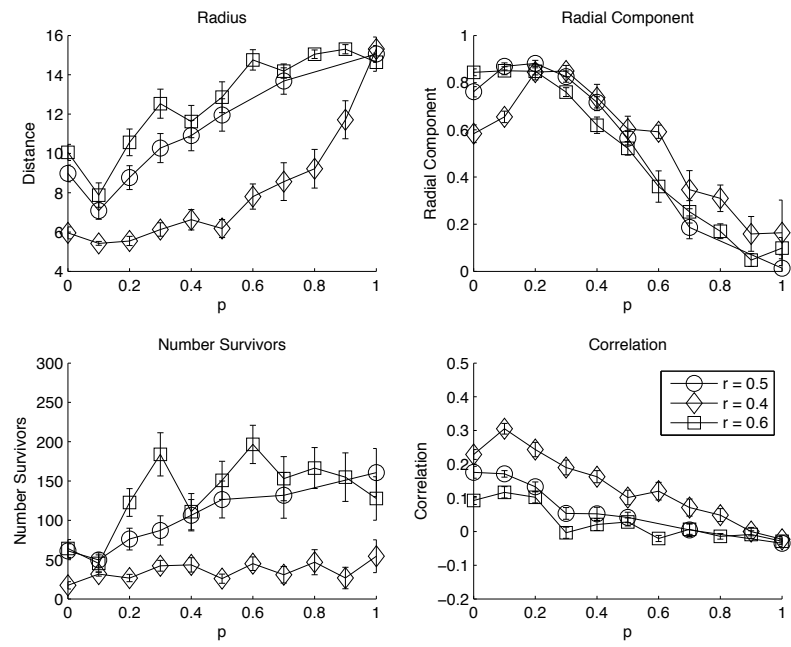


Figure A.4: Integration patterns of new neurons in normal inhibition networks, after perturbing the size of the local radius for new cells. Increasing the radius causes almost no difference, although decreasing it too much results in cells that have a hard time finding strong innervation and thus surviving.

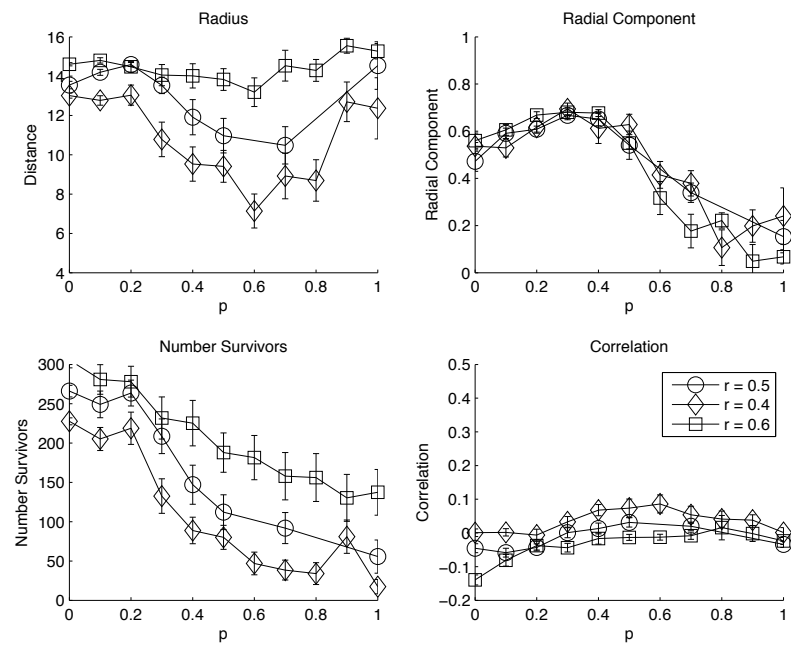


Figure A.5: Integration patterns of new neurons in low inhibition networks, after perturbing the size of the local radius for new cells. Unlike the normal inhibition case, for low inhibition the radius matters, but only changes the absolute magnitudes of number of surviving new cells and mean distance and does not alter the shape of the dependence on p .

as increasing excitatory connectivity increases the influence of excitation compared to inhibition. As p increases, the outcomes become similar to the normal inhibition case with lower connectivity. This is because the extra connections are not making any particular region more densely interconnected at higher random wiring, so their effect lessens. Due of the similarities to the two primary cases we look at, we restrict our discussion in the main text to inhibition and rewiring.

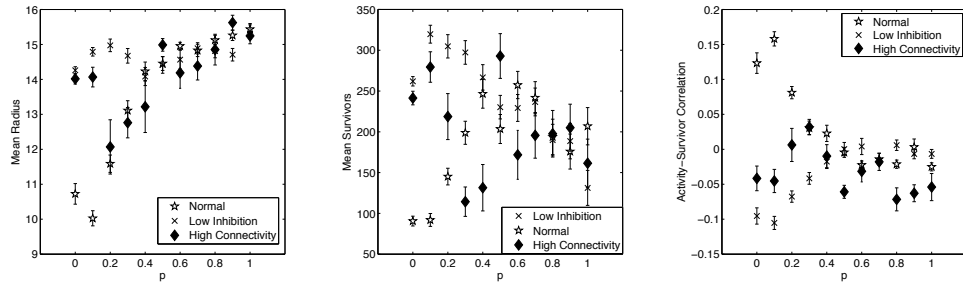


Figure A.6: A comparison of integration patterns in a high connectivity network (4.5% instead of 3.5%) with 200 inhibitory cells. Note that around $p = 0.2$, the networks switch from behaving like they are in a low inhibition regime to one with normal inhibition.

A.7 Rewiring and orientation results

The newly born neurons are thought to have higher structural plasticity, enabling them to rapidly form and abolish synaptic connections to other cells. This potentially allows the cells to optimally integrate themselves into the existing networks. In our simulation this reconnection occurs when an immature neuron is unable to generate a sufficient number of downstream coincident firing events. We observed that the number of activity dependent reconnection events per surviving cell is highest for global network topologies (Figure A.7c). Furthermore, networks with lowered inhibition exhibit lower rates of reconnection events for $p < 0.5$ due to the overall activity being higher in the network with lowered inhibition. New cells therefore do

not seek specific targets, indicating a lower potential controllability of the process, as well as a possible reason for significant modifications of the hippocampal network structure during epileptogenesis as shown in Figure A.7a. Examples of the mean directionality that results from this reconnection process can be seen in Figure A.7b.

We also looked at the spatial distribution of reconnection events as a function of p and inhibition (Figure A.7). Under normal inhibition and for relatively local networks, cells that lie outside the immediate stimulated area undergo significantly more reconnection events. Established cells within the stimulated region are more likely than remote cells to respond to firing events from new cells, making it an easier region to wire into. This effect becomes less dramatic and eventually goes away for more random network topologies as well as for networks with diminished inhibition.

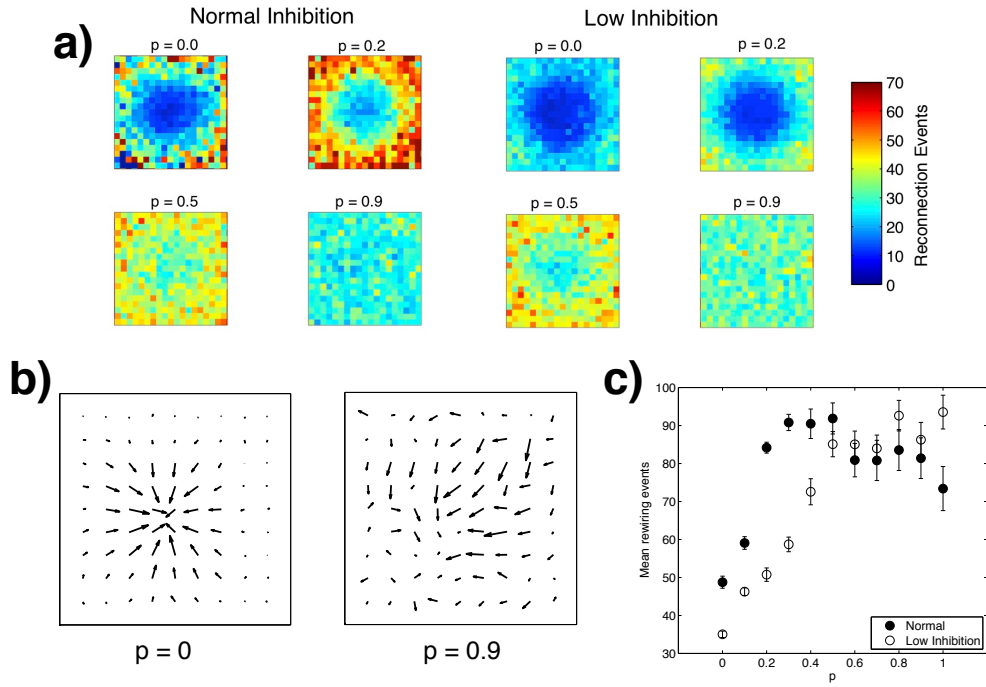


Figure A.7: a) Examples of the mean number of reconnection events as a function of space for several values of rewiring and inhibition. Note that in cases where the network acts like a good filter, which is to say and low p , the network splits into regions where it is easy to wire into and regions where it is hard to wire into, with the separation being greater for normal inhibition. b) Mean direction of output connections as a function of location for two different values of rewiring. Both have normal inhibition. For low rewiring, the connections are aligned radially, whereas for higher rewiring the orientation becomes more random. c) Average number of rewiring events. Networks with low inhibition require less searching to effectively integrate into the network.

BIBLIOGRAPHY

- [1] L. F. Abbott and S. B. Nelson. Synaptic plasticity: taming the beast. *Nat Neurosci*, 3 Suppl:1178–83, 2000.
- [2] D. N. Abrous, M. Koehl, and M. L. Moal. Adult neurogenesis: from precursors to network and physiology. *Physiol Rev*, 85(2):523–69, 2005.
- [3] J. B. Aimone, J. Wiles, and F. H. Gage. Potential role for adult neurogenesis in the encoding of time in new memories. *Nat Neurosci*, 9(6):723–7, 2006.
- [4] J. B. Aimone, J. Wiles, and F. H. Gage. Computational influence of adult neurogenesis on memory encoding. *Neuron*, 61(2):187–202, 2009.
- [5] R. Albert and A.-L. Barabasi. Statistical mechanics of complex networks. *Reviews of Modern Physics*, 74, 2002.
- [6] K. T. Alligood, T. Sauer, and J. A. Yorke. *Chaos: An Introduction to Dynamical Systems*. Springer-Verlag, New York, NY, 1997.
- [7] J. Altman and G. D. Das. Autoradiographic and histological evidence of postnatal hippocampal neurogenesis in rats. *J Comp Neurol*, 124(3):319–35, 1965.
- [8] D. G. Amaral, H. E. Scharfman, and P. Lavenex. The dentate gyrus: fundamental neuroanatomical organization (dentate gyrus for dummies). *Prog Brain Res*, 163:3–22, 2007.
- [9] R. Ananthakrishnan and A. Ehrlicher. The forces behind cell movement. *International Journal of Biological Sciences*, 3, 2007.
- [10] P. Andersen. *The Hippocampus Book*. Oxford University Press, New York, 2007.
- [11] T. Antal, S. Redner, and V. Sood. Evolutionary dynamics on degree-heterogeneous graphs. *Phys Rev Lett*, 96(18):188104, 2006.
- [12] K. Asano, C. D. Duntsch, Q. Zhou, J. D. Weimar, D. Bordelon, J. H. Robertson, and T. Pourmotabbed. Correlation of N-cadherin expression in high grade gliomas with tissue invasion. *J Neurooncol*, 70(1):3–15, 2004.

- [13] R. Axelrod. The dissemination of culture: A model with local convergence and global polarization. *Journal of conflict resolution*, 41(2):203–226, 1997.
- [14] R. Ayala, T. Shu, and L.-H. Tsai. Trekking across the brain: the journey of neuronal migration. *Cell*, 128(1):29–43, 2007.
- [15] D. T. Balu and I. Lucki. Adult hippocampal neurogenesis: regulation, functional implications, and contribution to disease pathology. *Neuroscience and biobehavioral reviews*, 33(3):232–52, 2009.
- [16] K. Barami, L. Lewis-Tuffin, and P. Z. Anastasiadis. The role of cadherins and catenins in gliomagenesis. *Neurosurg Focus*, 21(4):E13, 2006.
- [17] G. J. Baxter, R. A. Blythe, W. Croft, and A. J. McKane. Utterance selection model of language change. *Phys Rev E*, 73:046118, 2006.
- [18] G. J. Baxter, R. A. Blythe, and A. J. McKane. Fixation and consensus times on a network: a unified approach. *Phys Rev Lett*, 101(25):258701, 2008.
- [19] S. Becker. A computational principle for hippocampal learning and neurogenesis. *Hippocampus*, 15(6):722–38, 2005.
- [20] J. Bednar, A. Bramson, A. Jones-Rooy, and S. Page. Emergent cultural signatures and persistent diversity: A model of conformity and consistency. *Preprint*, 2008.
- [21] E. Ben-Naim, L. Frachebourg, and P. L. Krapivsky. Coarsening and persistence in the voter model. *Phys Rev E*, 53(4), 1996.
- [22] J. Bengzon, Z. Kokaia, E. Elmér, A. Nanobashvili, M. Kokaia, and O. Lindvall. Apoptosis and proliferation of dentate gyrus neurons after single and intermittent limbic seizures. *Proc Natl Acad Sci USA*, 94(19):10432–7, 1997.
- [23] V. Blondel, J. Guillaume, J. Hendrickx, C. de Kerchove, and R. Lambiotte. Local leaders in random networks. *Phys Rev E*, 2008.
- [24] R. A. Blythe. The propagation of a cultural or biological trait by neutral genetic drift in a subdivided population. *Theoretical Population Biology*, 71:454–472, 2007.
- [25] R. A. Blythe and A. J. McKane. Stochastic models of evolution in genetics, ecology and linguistics. *J Stat Mech*, 7:P07018, 2007.
- [26] S. D. Bouard, C. Christov, J. Guillamo, L. Kassar-Duchossoy, S. Palfi, C. Leguerinel, M. Masset, O. Cohen-Hagenauer, M. Peschanski, and T. Lefrançois. Invasion of human glioma biopsy specimens in cultures of rodent brain slices: a quantitative analysis. *J Neurosurg*, 97(1):169–176, 2002.
- [27] D. Boyer and O. Miramontes. Interface motion and pinning in small-world networks. *Phys Rev E*, 67, 2003.

- [28] A. Brú, S. Albertos, J. L. Subiza, J. L. García-Asenjo, and I. Brú. The universal dynamics of tumor growth. *Biophys J*, 85(5):2948–61, 2003.
- [29] E. Bruel-Jungerman, C. Rampon, and S. Laroche. Adult hippocampal neurogenesis, synaptic plasticity and memory: facts and hypotheses. *Reviews in the neurosciences*, 18(2):93–114, 2007.
- [30] P. S. Buckmaster and F. E. Dudek. Network properties of the dentate gyrus in epileptic rats with hilar neuron loss and granule cell axon reorganization. *J Neurophysiol*, 77(5):2685–96, 1997.
- [31] P. S. Buckmaster, G. F. Zhang, and R. Yamawaki. Axon sprouting in a model of temporal lobe epilepsy creates a predominantly excitatory feedback circuit. *J Neurosci*, 22(15):6650–8, 2002.
- [32] E. Bullmore and O. Sporns. Complex brain networks: graph theoretical analysis of structural and functional systems. *Nat Rev Neurosci*, 10(3):186–98, 2009.
- [33] H. A. Cameron, C. S. Woolley, B. S. McEwen, and E. Gould. Differentiation of newly born neurons and glia in the dentate gyrus of the adult rat. *Neuroscience*, 56(2):337–44, 1993.
- [34] L. Cao, X. Jiao, D. S. Zuzga, Y. Liu, D. M. Fong, D. Young, and M. J. During. VEGF links hippocampal activity with neurogenesis, learning and memory. *Nat Genet*, 36(8):827–35, 2004.
- [35] C. Castellano. Effect of network topology on the ordering dynamics of voter models. *arXiv:cond-mat/0504522*, 2005.
- [36] C. Castellano, S. Fortunato, and V. Loreto. Statistical physics of social dynamics. *Reviews of Modern Physics*, 81, 2009.
- [37] C. Castellano, V. Loreto, A. Barrat, and F. Cecconi. Comparison of voter and glauber ordering dynamics on networks. *Phys Rev E*, 2005.
- [38] C. Castellano, D. Vilone, and A. Vespignani. Incomplete ordering of the voter model on small-world networks. *Europhys Lett*, 63(1), 2003.
- [39] R. A. Chambers, M. N. Potenza, R. E. Hoffman, and W. Miranker. Simulated apoptosis/neurogenesis regulates learning and memory capabilities of adaptive neural networks. *Neuropsychopharmacology*, 29(4):747–58, 2004.
- [40] Y.-S. Chu, W. A. Thomas, O. Eder, F. Pincet, E. Perez, J. P. Thiery, and S. Dufour. Force measurements in e-cadherin-mediated cell doublets reveal rapid adhesion strengthened by actin cytoskeleton remodeling through rac and cdc42. *J Cell Biol*, 167(6):1183–94, 2004.

- [41] A. Clauset, C. R. Shalizi, and M. E. J. Newman. Power-law distributions in empirical data. *SIAM Review*, 51(4):661–703, 2009.
- [42] E. Clément, P. Leroux-Hugon, and L. Sander. Exact results for a chemical reaction model. *Phys Rev Lett*, 67(12), 1991.
- [43] P. Clifford and A. Sudbury. Model for spatial conflict. *Biometrika*, 60(3):581–588, 1973.
- [44] R. Cooper. *Coordination Games*. Cambridge University Press, Cambridge, UK, 1998.
- [45] E. Cukierman, R. Pankov, D. R. Stevens, and K. M. Yamada. Taking cell-matrix adhesions to the third dimension. *Science*, 294(5547):1708–12, 2001.
- [46] T. S. Deisboeck and I. D. Couzin. Collective behavior in cancer cell populations. *Bioessays*, 31(2):190–7, 2009.
- [47] T. S. Deisboeck, T. Demuth, and Y. Mansury. Correlating velocity patterns with spatial dynamics in glioma cell migration. *Acta Biotheoretica*, 53:181–190, 2005.
- [48] K. Deisseroth, S. Singla, H. Toda, M. Monje, T. D. Palmer, and R. C. Malenka. Excitation-neurogenesis coupling in adult neural stem/progenitor cells. *Neuron*, 42(4):535–52, 2004.
- [49] T. Demuth and M. E. Berens. Molecular mechanisms of glioma cell migration and invasion. *J Neurooncol*, 70(2):217–28, 2004.
- [50] T. Demuth, N. J. Hopf, O. Kempski, D. Sauner, M. Herr, A. Giese, and A. Perneczky. Migratory activity of human glioma cell lines in vitro assessed by continuous single cell observation. *Clin Exp Metastasis*, 18(7):589–97, 2001.
- [51] J. Desgrange and D. A. Cheresh. Integrins in cancer: biological implications and therapeutic opportunities. *Nat Rev Cancer*, 10, 2010.
- [52] A. Deutsch and S. Dormann. *Cellular Automaton Modeling of Biological Pattern Formation*. Birkhauser Boston, 2005.
- [53] I. Dornic, H. Chaté, J. Chave, and H. Hinrichsen. Critical coarsening without surface tension: The universality class of the voter model. *Phys Rev Lett*, 87(4), 2001.
- [54] S. Dorogovtsev and J. F. F. Mendes. *Evolution of Networks: From Biological Nets to the Internet and WWW*. Oxford University Press, USA, 2003.
- [55] A. D. Doyle, F. W. Wang, K. Matsumoto, and K. M. Yamada. One-dimensional topography underlies three-dimensional fibrillar cell migration. *J Cell Biol*, 184(4):481–90, 2009.

- [56] D. D. Duca, T. Werbowetski, and R. D. Maestro. Spheroid preparation from hanging drops: characterization of a model of brain tumor invasion. *J Neurooncol*, 67(3):295–303, 2004.
- [57] F. E. Dudek and L.-R. Shao. Mossy fiber sprouting and recurrent excitation: direct electrophysiologic evidence and potential implications. *Epilepsy Currents*, 4(5):184–7, 2004.
- [58] J. Dyhrfjeld-Johnsen, V. Santhakumar, R. J. Morgan, R. Huerta, L. S. Tsimring, and I. Soltesz. Topological determinants of epileptogenesis in large-scale structural and functional models of the dentate gyrus derived from experimental data. *J Neurophysiol*, 97(2):1566–87, 2007.
- [59] P. Erdős and A. Rényi. On the evolution of random graphs. *Publ. Math. Inst. Hung. Acad. Sci*, 5, 1960.
- [60] S. Farioli-Vecchioli, D. Saraulli, M. Costanzi, S. Pacioni, I. Cinà, M. Aceti, L. Micheli, A. Bacci, V. Cestari, and F. Tirone. The timing of differentiation of adult hippocampal neurons is crucial for spatial memory. *PLoS Biol*, 6(10):e246, 2008.
- [61] S. Fedotov and A. Iomin. Probabilistic approach to a proliferation and migration dichotomy in tumor cell invasion. *Phys Rev E*, 77(3 Pt 1):031911, 2008.
- [62] L. Festinger. *A Theory of Cognitive Dissonance*. Stanford University Press, California, 1957.
- [63] D. A. Fletcher and J. Theriot. An introduction to cell motility for the physical scientist. *Phys. Biol.*, 1:T1–T10, 2004.
- [64] L. Frachebourg and P. L. Krapivsky. Exact results for kinetics of catalytic reactions. *Phys Rev E*, 53(4), 1996.
- [65] F. Furnari, T. Fenton, and R. Bachoo. Malignant astrocytic glioma: genetics, biology, and paths to treatment. *Genes & Development*, 21:2683–2710, 2007.
- [66] C. W. Gardiner. *Handbook of Stochastic Methods*. Springer-Verlag, New York, NY, 2004.
- [67] S. Ge, D. A. Pradhan, G.-L. Ming, and H. Song. GABA sets the tempo for activity-dependent adult neurogenesis. *Trends Neurosci*, 30(1):1–8, 2007.
- [68] W. Gerstner and W. M. Kistler. *Spiking Neuron Models*. Cambridge University Press, Cambridge, UK, 2002.
- [69] A. Giese, M. A. Loo, N. Tran, D. Haskett, S. W. Coons, and M. E. Berens. Dichotomy of astrocytoma migration and proliferation. *Int J Cancer*, 67(2):275–82, 1996.

- [70] E. Glaeser, B. Sacerdote, and J. Scheinkman. Crime and social interactions. *The Quarterly Journal of Economics*, 111(2):507–548, 1996.
- [71] R. Goldbrunner, J. Bernstein, and J. Tonn. Cell-extracellular matrix interaction in glioma invasion. *Acta Neurochirurgica*, 141:295–305, 1999.
- [72] C. Gong, T. Wang, H. Huang, and J. M. Parent. Reelin regulates neuronal progenitor migration in intact and epileptic hippocampus. *J Neurosci*, 27(8):1803–1811, 2007.
- [73] V. D. Gordon, M. Valentine, M. Gardel, D. Andor-Ardo, S. Dennison, A. Bogdanov, D. A. Weitz, and T. S. Deisboeck. Measuring the mechanical stress induced by an expanding multicellular tumor system: a case study. *Exp Cell Res*, 289:58–66, 2003.
- [74] S. Gupta, R. Anderson, and R. May. Networks of sexual contacts: Implications for the pattern of spread of HIV. *AIDS*, 1989.
- [75] Y. He, Z. J. Chen, and A. C. Evans. Small-world anatomical networks in the human brain revealed by cortical thickness from MRI. *Cereb Cortex*, 17(10):2407–19, 2007.
- [76] B. Hegedus, A. Czirok, I. Fazekas, T. B'abel, E. Madar'asz, and T. Vicsek. Locomotion and proliferation of glioblastoma cells in vitro: statistical evaluation of videomicroscopic observations. *J Neurosurg*, 92(3):428–34, 2000.
- [77] B. Hegedus, F. Marga, K. Jakab, and K. Sharpe-Timms. The interplay of cell-cell and cell-matrix interactions in the invasive properties of brain tumors. *Biophys J*, 2006.
- [78] C. Heinrich, N. Nitta, A. Flubacher, and M. Muller. Reelin deficiency and displacement of mature neurons, but not neurogenesis, underlie the formation of granule cell dispersion in the epileptic hippocampus. *J Neurosci*, 2006.
- [79] G. L. Holmes. Epilepsy in the developing brain: lessons from the laboratory and clinic. *Epilepsia*, 38(1):12–30, 1997.
- [80] J. D. Hood and D. A. Cheresh. Role of integrins in cell invasion and migration. *Nat Rev Cancer*, 2, 2002.
- [81] K. Huang. *Introduction to Statistical Physics*. Taylor & Francis, USA, 2001.
- [82] S. Hubbell. *The Unified Neutral Theory of Biodiversity and Biogeography*. Princeton University Press, NJ, 2001.
- [83] A. Huttenlocher, R. R. Sandborg, and A. F. Horwitz. Adhesion in cell migration. *Current Opinion in Cell Biology*, 7(5):697–706, 1995.

- [84] P. Jablonski, G. R. Poe, and M. Zochowski. Structural network heterogeneities and network dynamics: a possible dynamical mechanism for hippocampal memory reactivation. *Phys Rev E*, 75(1 Pt 1):011912, 2007.
- [85] S. Jessberger, K. Nakashima, and G. C. Jr. Epigenetic modulation of seizure-induced neurogenesis and cognitive decline. *J Neurosci*, 27(22):5967–5975, 2007.
- [86] S. Jessberger, C. Zhao, N. Toni, and G. C. Jr. Seizure-associated, aberrant neurogenesis in adult rats characterized with retrovirus-mediated cell labeling. *J Neurosci*, 27(35):9400–9407, 2007.
- [87] K.-H. Jung, K. Chu, M. Kim, S.-W. Jeong, Y.-M. Song, S.-T. Lee, J.-Y. Kim, S. K. Lee, and J.-K. Roh. Continuous cytosine-b-d-arabinofuranoside infusion reduces ectopic granule cells in adult rat hippocampus with attenuation of spontaneous recurrent seizures following pilocarpine-induced status epilepticus. *Eur J Neurosci*, 19(12):3219–26, 2004.
- [88] K.-H. Jung, K. Chu, S.-T. Lee, J. Kim, D.-I. Sinn, J.-M. Kim, D.-K. Park, J.-J. Lee, S. U. Kim, M. Kim, S. K. Lee, and J.-K. Roh. Cyclooxygenase-2 inhibitor, celecoxib, inhibits the altered hippocampal neurogenesis with attenuation of spontaneous recurrent seizures following pilocarpine-induced status epilepticus. *Neurobiol Dis*, 23(2):237–46, 2006.
- [89] L. Kadanoff. *Statistical Physics: Statics, Dynamics and Renormalization*. World Scientific Publishing Co., Singapore, 2000.
- [90] M. S. Kaplan and J. W. Hinds. Neurogenesis in the adult rat: electron microscopic analysis of light radioautographs. *Science*, 197(4308):1092–4, 1977.
- [91] N. Kee, C. M. Teixeira, A. H. Wang, and P. W. Frankland. Preferential incorporation of adult-generated granule cells into spatial memory networks in the dentate gyrus. *Nat Neurosci*, 10(3):355–62, 2007.
- [92] G. Kempermann. The neurogenic reserve hypothesis: what is adult hippocampal neurogenesis good for? *Trends Neurosci*, 31(4), 2008.
- [93] E. Khain and L. M. Sander. Dynamics and pattern formation in invasive tumor growth. *Phys Rev Lett*, 96(18):188103, 2006.
- [94] E. Khain and L. M. Sander. Generalized Cahn-Hilliard equation for biological applications. *Phys Rev E*, 77(5 Pt 1):051129, 2008.
- [95] E. Khain, L. M. Sander, and C. M. Schneider-Mizell. The role of cell-cell adhesion in wound healing. *J Stat Phys*, 128(1-2):209–218, 2007.
- [96] E. Khain, C. M. Schneider-Mizell, M. O. Nowicki, E. A. Chiocca, S. Lawler, and L. M. Sander. Pattern formation of glioma cells: Effects of adhesion. *Europhys Lett*, 88(2):28006, 2009.

- [97] M. Kimura and T. Ohta. The average number of generations until fixation of a mutant gene in a finite population. *Genetics*, 61:763–771, 1969.
- [98] H. Kleinman and G. Martin. Matrigel: Basement membrane matrix with biological activity. *Semin Cancer Biol*, 15(5):378–386, 2005.
- [99] Z. A. Kohutek, C. G. diPierro, G. T. Redpath, and I. M. Hussaini. Adam-10-mediated n-cadherin cleavage is protein kinase c-alpha dependent and promotes glioblastoma cell migration. *J Neurosci*, 29(14):4605–4615, 2009.
- [100] P. L. Krapivsky. Kinetics of monomer-monomer surface catalytic reactions. *Physical Review A*, 45(2), 1992.
- [101] P. L. Krapivsky and S. Redner. Finiteness and fluctuations in growing networks. *Journal of Physics A*, 35:9517–9534, 2002.
- [102] H. G. Kuhn, H. Dickinson-Anson, and F. H. Gage. Neurogenesis in the dentate gyrus of the adult rat: age-related decrease of neuronal progenitor proliferation. *J Neurosci*, 16(6):2027–33, 1996.
- [103] R. Kuruba, B. Hattiangady, and A. K. Shetty. Hippocampal neurogenesis and neural stem cells in temporal lobe epilepsy. *Epilepsy & Behavior*, 14 Suppl 1:65–73, 2009.
- [104] C.-A. Lamontagne, C. M. Cuerrier, and M. Grandbois. AFM as a tool to probe and manipulate cellular processes. *Pflugers Arch*, 456(1):61–70, 2008.
- [105] C.-A. Lamontagne and M. Grandbois. PKC-induced stiffening of hyaluronan/CD44 linkage; local force measurements on glioma cells. *Exp Cell Res*, 314(2):227–36, 2008.
- [106] F. Lefranc, J. Brotchi, and R. Kiss. Possible future issues in the treatment of glioblastomas: Special emphasis on cell migration and the resistance of migrating glioblastoma cells to apoptosis. *Journal of Clinical Oncology*, 23(10), 2005.
- [107] K. Lehmann, M. Butz, and G. Teuchert-Noodt. Offer and demand: proliferation and survival of neurons in the dentate gyrus. *Eur J Neurosci*, 21(12):3205–16, 2005.
- [108] T. M. Liggett. *Interacting Particle Systems*. Springer, New York, 2005.
- [109] C.-W. Lin, S. Sim, A. Ainsworth, M. Okada, W. Kelsch, and C. Lois. Genetically increased cell-intrinsic excitability enhances neuronal integration into adult brain circuits. *Neuron*, 65(1):32–9, 2010.
- [110] R. Littler. Loss of variability at one locus in a finite population. *Mathematical Biosciences*, 25:151–163, 1975.

- [111] P.-M. Lledo, M. Alonso, and M. S. Grubb. Adult neurogenesis and functional plasticity in neuronal circuits. *Nat Rev Neurosci*, 7(3):179–93, 2006.
- [112] C. Martinez-Rico, F. Pincet, E. Perez, J. P. Thiery, K. Shimizu, Y. Takai, and S. Dufour. Separation force measurements reveal different types of modulation of e-cadherin-based adhesion by nectin-1 and -3. *J Biol Chem*, 280(6):4753–60, 2005.
- [113] G. Mathern, T. Babb, J. Leite, and J. Pretorius. The pathogenic and progressive features of chronic human hippocampal epilepsy. *Epilepsy Res*, 1996.
- [114] A. Mogilner. Mathematics of cell motility: have we got its number? *J. Math. Biol.*, 2008.
- [115] M. Molloy and B. Reed. A critical point for random graphs with a given degree sequence. *Random Structures and Algorithms*, 6:161–180, 1995.
- [116] R. J. Morgan and I. Soltesz. Nonrandom connectivity of the epileptic dentate gyrus predicts a major role for neuronal hubs in seizures. *Proc Natl Acad Sci USA*, 105(16):6179–84, 2008.
- [117] T. Netoff, R. Clewley, S. Arno, T. Keck, and J. White. Epilepsy in small-world networks. *J Neurosci*, 2004.
- [118] M. Newman. The structure and function of complex networks. *SIAM Review*, 45:167–256, 2003.
- [119] M. Newman. Power laws, Pareto distributions and Zipfs law. *Contemporary Physics*, 2005.
- [120] M. E. J. Newman, A.-L. Barabási, and D. J. Watts. *The Structure and Dynamics of Networks*. Princeton University Press, NJ, 2006.
- [121] R. Nishikawa, X. D. Ji, R. C. Harmon, C. S. Lazar, G. N. Gill, W. K. Cavenee, and H. J. Huang. A mutant epidermal growth factor receptor common in human glioma confers enhanced tumorigenicity. *Proc Natl Acad Sci USA*, 91(16):7727–31, 1994.
- [122] F. Nottebohm. Neuronal replacement in adult brain. *Brain Res Bull*, 57(6):737–49, 2002.
- [123] G. Ódor. Universality classes in nonequilibrium lattice systems. *Reviews of Modern Physics*, 76, 2004.
- [124] I. Ortega-Perez, K. Murray, and P.-M. Lledo. The how and why of adult neurogenesis. *J Mol Histol*, 38(6):555–62, 2007.
- [125] L. S. Overstreet-Wadiche, D. A. Bromberg, and A. L. Bensen. Seizures accelerate functional integration of adult-generated granule cells. *J Neurosci*, 2006.

- [126] L. S. Overstreet-Wadiche, D. A. Bromberg, A. L. Bensen, and G. L. Westbrook. Seizures accelerate functional integration of adult-generated granule cells. *J Neurosci*, 26(15):4095–103, 2006.
- [127] L. S. Overstreet-Wadiche and G. L. Westbrook. Functional maturation of adult-generated granule cells. *Hippocampus*, 16(3):208–15, 2006.
- [128] S. Page, L. Sander, and C. M. Schneider-Mizell. Conformity and dissonance in generalized voter models. *J Stat Phys*, 128:1279–1287, 2007.
- [129] F. Pampaloni, E. Reynaud, and E. Stelzer. The third dimension bridges the gap between cell culture and live tissue. *Nat Rev Mol Cell Bio*, 8, 2007.
- [130] J. M. Parent. The role of seizure-induced neurogenesis in epileptogenesis and brain repair. *Epilepsy Res*, 50(1-2):179–89, 2002.
- [131] J. M. Parent, R. C. Elliott, S. J. Pleasure, N. M. Barbaro, and D. H. Lowenstein. Aberrant seizure-induced neurogenesis in experimental temporal lobe epilepsy. *Ann Neurol*, 59(1):81–91, 2006.
- [132] J. M. Parent and D. H. Lowenstein. Mossy fiber reorganization in the epileptic hippocampus. *Curr Opin Neurol*, 10(2):103–9, 1997.
- [133] J. M. Parent and G. G. Murphy. Mechanisms and functional significance of aberrant seizure-induced hippocampal neurogenesis. *Epilepsia*, 49 Suppl 5:19–25, 2008.
- [134] J. M. Parent, E. Tada, J. R. Fike, and D. H. Lowenstein. Inhibition of dentate granule cell neurogenesis with brain irradiation does not prevent seizure-induced mossy fiber synaptic reorganization in the rat. *J Neurosci*, 19(11):4508–19, 1999.
- [135] J. M. Parent, N. von dem Bussche, and D. H. Lowenstein. Prolonged seizures recruit caudal subventricular zone glial progenitors into the injured hippocampus. *Hippocampus*, 16(3):321–8, 2006.
- [136] J. M. Parent, T. W. Yu, R. T. Leibowitz, D. H. Geschwind, R. S. Sloviter, and D. H. Lowenstein. Dentate granule cell neurogenesis is increased by seizures and contributes to aberrant network reorganization in the adult rat hippocampus. *J Neurosci*, 17(10):3727–38, 1997.
- [137] R. Pastor-Satorras and A. Vespignani. Epidemic spreading in scale-free networks. *Phys Rev Lett*, 86(14), 2001.
- [138] J. A. Pedersen and M. A. Swartz. Mechanobiology in the third dimension. *Annals of Biomedical Engineering*, 33(11):1469–90, 2005.

- [139] C. Perego, C. Vanoni, S. Massari, A. Raimondi, S. Pola, M. G. Cattaneo, M. Francolini, L. M. Vicentini, and G. Pietrini. Invasive behaviour of glioblastoma cell lines is associated with altered organisation of the cadherin-catenin adhesion system. *Journal of Cell Science*, 115(Pt 16):3331–40, 2002.
- [140] J. P. Pierce, J. Melton, M. Punsoni, D. P. McCloskey, and H. E. Scharfman. Mossy fibers are the primary source of afferent input to ectopic granule cells that are born after pilocarpine-induced seizures. *Exp Neurol*, 196(2):316–31, 2005.
- [141] E. Pugliese and C. Castellano. Heterogeneous pair approximation for voter models on networks. *Europhys Lett*, 88:54004, 2009.
- [142] V. Ramirez-Amaya, D. F. Marrone, F. H. Gage, P. F. Worley, and C. A. Barnes. Integration of new neurons into functional neural networks. *J Neurosci*, 26(47):12237–41, 2006.
- [143] S. Redner. *A Guide to First-Passage Processes*. Cambridge University Press, Cambridge, UK, 2007.
- [144] F. Rohlf and G. Schnell. An investigation of the isolation-by-distance model. *American Naturalist*, 105:295–324, 1971.
- [145] A. Roxin, H. Riecke, and S. A. Solla. Self-sustained activity in a small-world network of excitable neurons. *Phys Rev Lett*, 92(19):198101, 2004.
- [146] P. L. Ryan, R. A. Fots, J. Kohn, and M. S. Steinberg. Tissue spreading on implantable substrates is a competitive outcome of cell-cell vs. cell-substratum adhesivity. *Proc Natl Acad Sci USA*, 98(8):4323–7, 2001.
- [147] H. E. Scharfman, J. H. Goodman, and A. L. Sollas. Granule-like neurons at the hilar/CA3 border after status epilepticus and their synchrony with area CA3 pyramidal cells: functional implications of seizure-induced neurogenesis. *J Neurosci*, 20(16):6144–58, 2000.
- [148] C. Schmidt-Hieber, P. Jonas, and J. Bischofberger. Enhanced synaptic plasticity in newly generated granule cells of the adult hippocampus. *Nature*, 429(6988):184–7, 2004.
- [149] C. M. Schneider-Mizell, J. M. Parent, and E. Ben-Jacob. Network structure determines patterns of network reorganization during adult neurogenesis. *arXiv:0912.2108v1*, 2009.
- [150] C. M. Schneider-Mizell and L. Sander. A generalized voter model on complex networks. *J Stat Phys*, 136:59–71, 2009.
- [151] M. A. Serrano, K. Klemm, F. Vazquez, V. M. Eguiluz, and M. S. Miguel. Conservation laws for voter-like models on random directed networks. *J Stat Mech*, page P10024, 2009.

- [152] F. A. Siebzehnrubl and I. Blumcke. Neurogenesis in the human hippocampus and its relevance to temporal lobe epilepsies. *Epilepsia*, 49 Suppl 5:55–65, 2008.
- [153] A. J. Silva, Y. Zhou, T. Rogerson, J. Shobe, and J. Balaji. Molecular and cellular approaches to memory allocation in neural circuits. *Science*, 326(5951):391–5, 2009.
- [154] F. Slanina and H. Lavicka. Analytical results for the sznajd model of opinion formation. *European Physical Journal B*, 35:279–288, 2003.
- [155] I. Soltész. *Diversity in the Neuronal Machine*. Oxford University Press, USA, 2006.
- [156] V. Sood, T. Antal, and S. Redner. Voter models on heterogeneous networks. *Phys Rev E*, 77, 2008.
- [157] V. Sood and S. Redner. Voter model on heterogeneous graphs. *Phys Rev Lett*, 94, 2005.
- [158] C. E. Stafstrom, A. Chronopoulos, S. Thurber, J. L. Thompson, and G. L. Holmes. Age-dependent cognitive and behavioral deficits after kainic acid seizures. *Epilepsia*, 34(3):420–32, 1993.
- [159] A. M. Stein, T. Demuth, D. Mobley, M. E. Berens, and L. M. Sander. A mathematical model of glioblastoma tumor spheroid invasion in a three-dimensional in vitro experiment. *Biophys J*, 92, 2007.
- [160] A. M. Stein, D. A. Vader, T. S. Deisboeck, E. A. Chiocca, L. M. Sander, and D. A. Weitz. Directionality of glioblastoma invasion in a 3d in vitro experiment. *arXiv:q-bio.CB/0610031*, 2006.
- [161] K. Suchecki, V. M. Eguiluz, and M. S. Miguel. Conservation laws for the voter model in complex networks. *Europhys Lett*, 69(2):228–234, 2005.
- [162] K. Suchecki, V. M. Eguiluz, and M. S. Miguel. Voter model dynamics in complex networks: Role of dimensionality, disorder, and degree distribution. *Phys Rev E*, 72, 2005.
- [163] K. Swanson, E. A. Jr, and J. Murray. Virtual brain tumours (gliomas) enhance the reality of medical imaging and highlight inadequacies of current therapy. *British Journal of Cancer*, 2002.
- [164] M. Takeichi. Cadherin cell adhesion receptors as a morphogenetic regulator. *Science*, 251:1451–5, 1991.
- [165] P. H. E. Tiesinga and T. J. Sejnowski. Rapid temporal modulation of synchrony by competition in cortical interneuron networks. *Neural computation*, 16(2):251–75, 2004.

- [166] P. Tracqui. Biophysical models of tumour growth. *Reports on Progress in Physics*, 72, 2009.
- [167] D. A. Vader, A. Kabla, D. A. Weitz, and L. Mahadevan. Strain-induced alignment in collagen gels. *PLoS ONE*, 4(6):e5902, 2009.
- [168] N. G. Van Kampen. *Stochastic Processes in Physics and Chemistry*. Elsevier, Amsterdam, 2007.
- [169] H. van Praag, B. R. Christie, T. J. Sejnowski, and F. H. Gage. Running enhances neurogenesis, learning, and long-term potentiation in mice. *Proc Natl Acad Sci USA*, 96(23):13427–31, 1999.
- [170] F. Vazquez and V. M. Eguiluz. Analytical solution of the voter model on uncorrelated networks. *New Journal of Physics*, 10, 2008.
- [171] M. Vicente-Manzanares, D. Webb, and A. F. Horwitz. Cell migration at a glance. *Journal of Cell Science*, 118:4917–4919, 2005.
- [172] D. Vilone and C. Castellano. Solution of voter model dynamics on annealed small-world networks. *Phys Rev E*, 69, 2004.
- [173] P. Voorhees. The theory of Ostwald ripening. *J Stat Phys*, 38, 1985.
- [174] D. Watts. Networks, dynamics, and the small-world phenomenon. *American Journal of Sociology*, 105(2), 1999.
- [175] D. Watts and S. Strogatz. Collective dynamics of ‘small-world’networks. *Nature*, 393, 1998.
- [176] B. Winters, S. Shepard, and R. A. Foty. Biophysical measurement of brain tumor cohesion. *International Journal of Cancer*, 114, 2005.
- [177] L. Wiskott, M. J. Rasch, and G. Kempermann. A functional hypothesis for adult hippocampal neurogenesis: avoidance of catastrophic interference in the dentate gyrus. *Hippocampus*, 16(3):329–43, 2006.
- [178] S. Wright. Evolution in mendelian populations. *Genetics*, 16:97–159, 1931.
- [179] H. P. Young. *Individual strategy and social structure: an evolutionary theory of institutions*. Princeton University Press, Princeton, NJ, 2001.
- [180] S. Yu, D. Huang, W. Singer, and D. Nikolic. A small world of neuronal synchrony. *Cereb Cortex*, 18(12):2891–901, 2008.
- [181] M. H. Zaman, L. Trapani, A. Siemeski, and D. MacKellar. Migration of tumor cells in 3d matrices is governed by matrix stiffness along with cell-matrix adhesion and proteolysis. *Proc Natl Acad Sci USA*, 103(29), 2006.

- [182] C. Zhao, W. Deng, and F. H. Gage. Mechanisms and functional implications of adult neurogenesis. *Cell*, 132:645–660, 2008.
- [183] C.-S. Zhao and L. S. Overstreet-Wadiche. Integration of adult generated neurons during epileptogenesis. *Epilepsia*, 49 Suppl 5:3–12, 2008.
- [184] R. Ziff, E. Gulari, and Y. Barshad. Kinetic phase transitions in an irreversible surface-reaction model. *Phys Rev Lett*, 56(24), 1986.